

# Modelling the Electric Field from Implantable Defibrillators

by

**Timothy John Gale**

B.E., M.Eng.Sc. (University of Melbourne)

School of Health Sciences

(*Dept of Clinical Sciences*)

Submitted in fulfilment of the  
requirements for the degree of

**Doctor of Philosophy**

University of Tasmania

August, 1995


## Declarations

This Thesis is my own work and contains no material that has been accepted for a degree or diploma by the University or any other institution, except by way of background material and duly acknowledged in the Thesis, and to the best of my knowledge and belief no material previously published or written by another person except where due acknowledgement is made in the text of the Thesis.

Signed: .....

Date: August 1995

This thesis is not to be made available for loan or copying for one year following the date this statement was signed. Following that time the thesis may be made available for loan and limited copying in accordance with the *Copyright Act 1968*.

Signed: .....

Date: August 1995

## Abstract

This thesis presents a mathematical model of the electric field from implantable defibrillators, together with the numerical implementation, validation and examples of application of the model.

The model was based on Laplace's equation for potential and was implemented using the boundary element method with constant quadrilateral elements and realistic torso structures. An efficient out-of-core solver was developed, allowing any size problem to be solved, subject only to computer speed and time available. A method was also developed that allowed matrices calculated in one problem to be used in other, similar problems, often reducing calculation times by an order of magnitude.

Model validation included comparison of myocardial potentials from the model to those from a finite element model (r.e.=2.8%) and from measurements in a sheep (c.c.=0.464, r.e.=23.6%). Validation was also done against resistance and voltage at defibrillation threshold from 29 patients implanted with a transvenous system and 8 patients with the transvenous system and an additional subcutaneous patch. Without the patch, the relative error between the average of the clinical results and the model result was 9.4% (voltage) and 0.8% (resistance). The average of the relative errors between each clinical result and the model result was 23.4% (voltage) and 11.6% (resistance). With the patch, the equivalent relative errors were 33.9%, 19.4%, 44.0% and 22.5%.

Transvenous, epicardial and subcutaneous electrode configurations were modelled in a series of investigations. The best transvenous configuration was with a right ventricular cathode and an anode in the inferior vena cava, where defibrillation voltage and energy were reduced by 35% and 55%, respectively, compared to a standard configuration with the anode in the superior vena cava. Configurations with a right ventricular cathode and large epicardial patch performed best, though, and reduced voltage and energy by up to 59% and 79%, respectively. The optimal length of the right ventricular transvenous electrode was approximately 60mm. An infarcted heart was also modelled.

For future work, anisotropy may be added to the heart and skeletal muscle of the model. Anisotropic regions may be represented by many small boundary element regions or by finite elements. Automated construction of the torso mesh and an algorithm for automatically optimising electrode position may be developed. Individual patients may be modelled and predicted values of defibrillation voltage, energy and resistance compared to values measured at the time of implantation.

In conclusion, the boundary element model was successful in modelling the electric field in the torso and in predicting implantable defibrillator performance. The model has potential to be used in research and development and in clinical settings.

## **Acknowledgements**

I wish to acknowledge help given by my supervisor, Professor D. Kilpatrick, and co-supervisors, Dr. P.R. Johnston and Dr. P.M. Nickolls, and also by Teletronics Pty. Ltd. I wish to acknowledge the work done by Dr. Johnston in providing computer code for some numerical integration routines, and providing geometry data for some torso surfaces used in the Thesis. I am very grateful to the support and assistance given by my supervisors.

I also wish to thank my wife Carol for her support and encouragement during the past four years, without which this task would have been much more difficult. I would also like to acknowledge the support of my parents and my parents in-law, which was much appreciated.

*To Carol and the boys—David, Richard and Philip*

# Contents

<b>1</b>	<b>Introduction</b>	<b>1</b>
<b>2</b>	<b>Biomedical Background</b>	<b>4</b>
2.1	Introduction . . . . .	4
2.2	Heart Structure and Function . . . . .	4
2.3	Early History of Defibrillation . . . . .	13
2.4	Implantable Defibrillators . . . . .	14
2.5	Defibrillator Voltage Waveforms . . . . .	17
2.6	Glossary . . . . .	18
<b>3</b>	<b>Literature Review</b>	<b>20</b>
3.1	Introduction . . . . .	20
3.2	Modelling . . . . .	20
3.3	Clinical Results using Implantable Defibrillators . . . . .	34
3.4	Discussion . . . . .	40
<b>4</b>	<b>Numerical Methods</b>	<b>42</b>
4.1	Introduction . . . . .	42
4.2	Boundary Element Method . . . . .	43
4.3	Finite Element Method . . . . .	48
<b>5</b>	<b>Implementation of Numerical Methods</b>	<b>50</b>
5.1	Introduction . . . . .	50

5.2	Torso Construction . . . . .	51
5.3	Boundary Element Method Implementation . . . . .	60
<b>6</b>	<b>Validation of Numerical Methods</b>	<b>67</b>
6.1	Introduction . . . . .	67
6.2	Comparison with Analytical Solution for Concentric Spheres . .	68
6.3	Comparison with Finite Element Solution for a Cube . . . . .	71
6.4	Comparison with Finite Element Solution for Realistic Torso and Electrodes . . . . .	72
<b>7</b>	<b>Validation in Sheep and Humans</b>	<b>76</b>
7.1	Introduction . . . . .	76
7.2	Sheep Validation . . . . .	77
7.3	Human Comparison . . . . .	82
<b>8</b>	<b>Investigations</b>	<b>86</b>
8.1	Introduction . . . . .	86
8.2	Electrode Types . . . . .	86
8.3	Electrode Configurations Tested . . . . .	88
8.4	Performance Calculations . . . . .	99
8.5	Results . . . . .	104
8.6	Discussion . . . . .	108
8.7	Conclusion . . . . .	130
<b>9</b>	<b>Conclusion</b>	<b>131</b>
<b>A</b>	<b>Detail of the Boundary Element Model</b>	<b>138</b>
<b>B</b>	<b>Element Integrals</b>	<b>149</b>
<b>C</b>	<b>Statistical Definitions</b>	<b>152</b>
<b>D</b>	<b>Enguard Electrodes</b>	<b>153</b>

# List of Figures

2.1	<i>Heart structure . . . . .</i>	5
2.2	<i>The probability curve for defibrillation (from Ideker et al. [1]) . .</i>	11
2.3	<i>Example of a common implantable defibrillator system, with a pulse generator, transvenous electrodes in the right ventricle (RV) and superior vena cava (SVC) and a subcutaneous (SQ) patch electrode . . . . .</i>	16
2.4	<i>Examples of potential defibrillator waveforms, plotted as voltage versus time. Truncated exponential, biphasic and sequential waveforms are commonly used with implantable defibrillators. . .</i>	18
3.1	<i>Minimum energy (mean <math>\pm</math> standard deviation) for defibrillation in humans for various electrode configurations (data from Table 3.3). Dotted line indicates mean energy. . . . .</i>	39
5.1	<i>Slice through the torso showing regions in the model . . . . .</i>	52
5.2	<i>Components of the human torso discretised into boundary elements (also see Plates 1 and 2) . . . . .</i>	55
5.3	<i>Components of the sheep torso discretised into boundary elements</i>	56
5.4	<i>Types of electrodes implemented in the boundary element model .</i>	57

5.5	<i>Cross-section through the (a) first, (b) second, (c) third and (d) sixth (and final) brick meshes during construction of the finite element torso. On the final brick mesh, bricks outside the torso have been removed and the boundary element mesh superimposed . . . . .</i>	58
5.6	<i>Components of the finite element torso . . . . .</i>	59
5.7	<i>The block structure of matrix A in equation (4.20) . . . . .</i>	61
5.8	<i>Matrix A and vector b from equation (4.20) after processing as far as possible to upper-diagonal form before the transvenous electrodes were defined . . . . .</i>	62
5.9	<i>Procedure for solving equation (4.20) . . . . .</i>	63
5.10	<i>Normal and tangential components of gradient on a boundary element. . . . .</i>	65
6.1	<i>Slice through the center of the concentric spheres model . . . . .</i>	69
6.2	<i>Potential and potential gradient within concentric spheres . . . . .</i>	70
6.3	<i>Finite element meshes (a) coarse, (b) each element split once (c) each element split twice. Surface nodes beneath the markers are set to the potentials indicated. . . . .</i>	72
6.4	<i>FE and BE results for meshes that are progressively refined . . . . .</i>	73
6.5	<i>Comparison of FE and BE results for endocardial electrodes in the RV and SVC (<math>RE = 2.8\%</math>) . . . . .</i>	74
7.1	<i>Apparatus to recording potentials from sheep . . . . .</i>	78
7.2	<i>Epicardial potential maps (mV) for experimental and model results for endocardial electrodes (50mV signal) in a sheep . . . . .</i>	80
7.3	<i>Correlation of epicardial potentials for experimental and model results for endocardial electrodes (50mV signal) in a sheep . . . . .</i>	81
7.4	<i>Comparison of defibrillation voltage and resistance from the model and from measurements in humans . . . . .</i>	84

8.1	<i>Example of a configuration with endocardial electrodes in the IVC and RV . . . . .</i>	87
8.2	<i>Anode at or above the standard position (configuration TA-VS) .</i>	90
8.3	<i>Anode below the standard position (configuration TA-VS) . . . .</i>	91
8.4	<i>Pulmonary artery transvenous electrode (configuration TA-PA) .</i>	92
8.5	<i>Modified transvenous right ventricular electrode (configuration EC) . . . . .</i>	93
8.6	<i>Different length right ventricular electrodes (configuration CL) .</i>	94
8.7	<i>Epicardial patch pair (configuration EPP) . . . . .</i>	95
8.8	<i>67cm<sup>2</sup> epicardial patch (configuration EP-T 1) . . . . .</i>	96
8.9	<i>131cm<sup>2</sup> epicardial patch (configuration EP-T 2) . . . . .</i>	96
8.10	<i>220cm<sup>2</sup> epicardial patch (configuration EP-T 3) . . . . .</i>	97
8.11	<i>25cm<sup>2</sup> epicardial patch and large (32cm<sup>2</sup>) right ventricular electrode (configuration EP-T 5) . . . . .</i>	98
8.12	<i>Apical, sub-apical and pectoral subcutaneous patch locations (configuration SQ) . . . . .</i>	100
8.13	<i>Left posterior epicardial and anterior subcutaneous patch combination (configuration SQ 4) . . . . .</i>	101
8.14	<i>Healthy and infarcted hearts: the infarcted heart was represented as having an infarct in the left-anterior wall of the left ventricle resulting in myopathy and bulging of the affected region into the lung cavity (configuration INF) . . . . .</i>	102
8.15	<i>Slices through healthy and infarcted hearts (configuration INF) .</i>	103
8.16	<i>Configuration TA-VS results showing how the location of the transvenous anode affects defibrillation performance with a standard cathode in the right ventricle. Height was measured to the inferior end of the electrode braid. . . . .</i>	105

8.17	<i>Configuration CL results showing how the length of the cathode in the right ventricle effects defibrillation performance with a standard anode in the superior vena cava . . . . .</i>	106
8.18	<i>Potential distribution, cathode &amp; anode 040-020 (TA-VS 1) . . .</i>	109
8.19	<i>Potential gradient distribution, cathode &amp; anode 040-020 (TA-VS 1) . . . . .</i>	110
8.20	<i>Potential distribution, cathode &amp; anode 040-024 (TA-VS 3) . . .</i>	111
8.21	<i>Potential gradient distribution, cathode &amp; anode 040-024 (TA-VS 3) . . . . .</i>	112
8.22	<i>Potential distribution, cathode &amp; optimal anode in inferior vena cava (TA-VS 4) . . . . .</i>	113
8.23	<i>Potential gradient distribution, cathode &amp; optimal anode in inferior vena cava (TA-VS 4) . . . . .</i>	114
8.24	<i>Potential distribution, cathode, anode 040-020 and apical subcutaneous patch (TA-SQ 1) . . . . .</i>	115
8.25	<i>Potential gradient distribution, cathode, anode 040-020 and apical subcutaneous patch (TA-SQ 1) . . . . .</i>	116
8.26	<i>Potential distribution, transvenous cathode and pulmonary artery anode (TA-PA 1) . . . . .</i>	117
8.27	<i>Potential gradient distribution, transvenous cathode and pulmonary artery anode (TA-PA 1) . . . . .</i>	118
8.28	<i>Potential distribution, epicardial patch pair (EPP) . . . . .</i>	119
8.29	<i>Potential gradient distribution, epicardial patch pair (EPP) . . .</i>	120
8.30	<i>Potential distribution, transvenous cathode and epicardial patch anode (EP-T 1) . . . . .</i>	121
8.31	<i>Potential gradient distribution, transvenous cathode and epicardial patch anode (EP-T 1) . . . . .</i>	122

8.32 (a) efficient ‘myocardial sandwich’ configuration where the voltage and energy is dissipated entirely within the myocardium (b) less efficient standard configuration with additional voltage and energy dissipation within other parts of the thorax . . . . . 129

D.1 Enguard ventricular electrode . . . . . 153

D.2 Enguard ventricular electrode-tip detail . . . . . 154

D.3 Enguard Standard Atrial Lead 040-020 . . . . . 155

D.4 Enguard Atrial Lead 040-022 . . . . . 156

D.5 Enguard Atrial Lead 040-024 . . . . . 157

# List of Tables

3.1	<i>Internal defibrillation simulation results (from Kinst et al. [2]). Epicardial patch pairs were: 54cm<sup>2</sup> conformal (epi-conform), 32cm<sup>2</sup> (epi-32) and 16cm<sup>2</sup> (epi-16). RV-10, RV-5 and SVC-5 designate location and length (in cm) of endocardial electrodes and SQ was a 25cm<sup>2</sup> subcutaneous patch. Energy was derived assuming 150μF capacitor and 7ms pulse. . . . .</i>	27
3.2	<i>Reported values of conductivity ('l' is longitudinal, 't' is transverse). . . . .</i>	31
3.3	<i>Reported performance of electrode configurations in humans. RA = right atrium, RV = right ventricle, SVC = superior vena cava, AC = active can pulse generator, SQ = subcutaneous patch (with subscript indicating location), CS = coronary sinus and (s) = stored energy. Energy data from this data is plotted in Figure 3.1. <i>p</i> values are between value on row and values below and/or above. <i>p</i>=NS for resistance. . . . .</i>	35
5.1	<i>Values of resistivity (Ωcm) used in the model. . . . .</i>	54
6.1	<i>Results from the concentric sphere model . . . . .</i>	69

7.1	<i>Relative error (%) (RE) between clinical and model results for configurations with endocardial electrodes in the right ventricle (RV) and superior vena cava (SVC) and an apical subcutaneous patch (SQ) . . . . .</i>	85
8.1	<i>Results of investigations for different electrode configurations in the human torso boundary element model. Results are for the resistance between the electrodes, electrode voltage, energy dissipated in the torso and the maximum voltage gradient in the ventricular myocardium. Results were calculated for defibrillation using a <math>150\mu F</math> capacitor and a monophasic 7ms pulse with a minimum voltage gradient in the ventricular myocardium of 5V/cm. . . . .</i>	107

# Plates

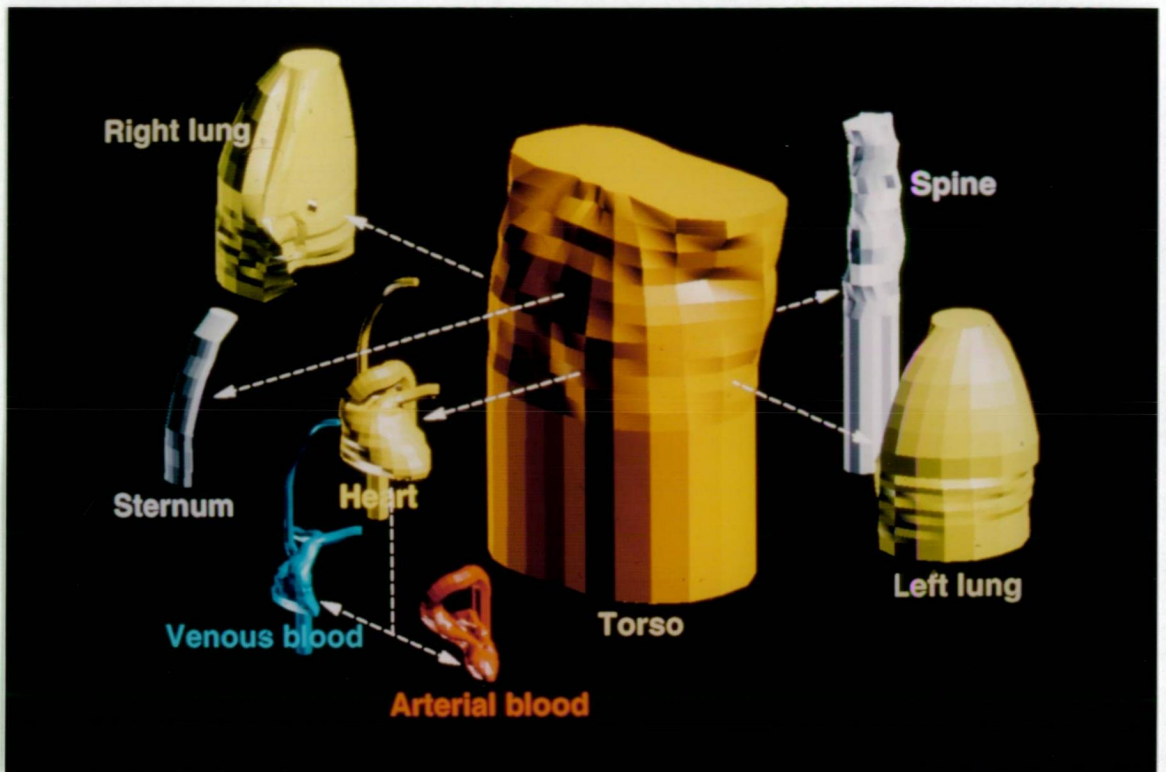


Plate 1: *Components of the boundary element human torso—exploded*

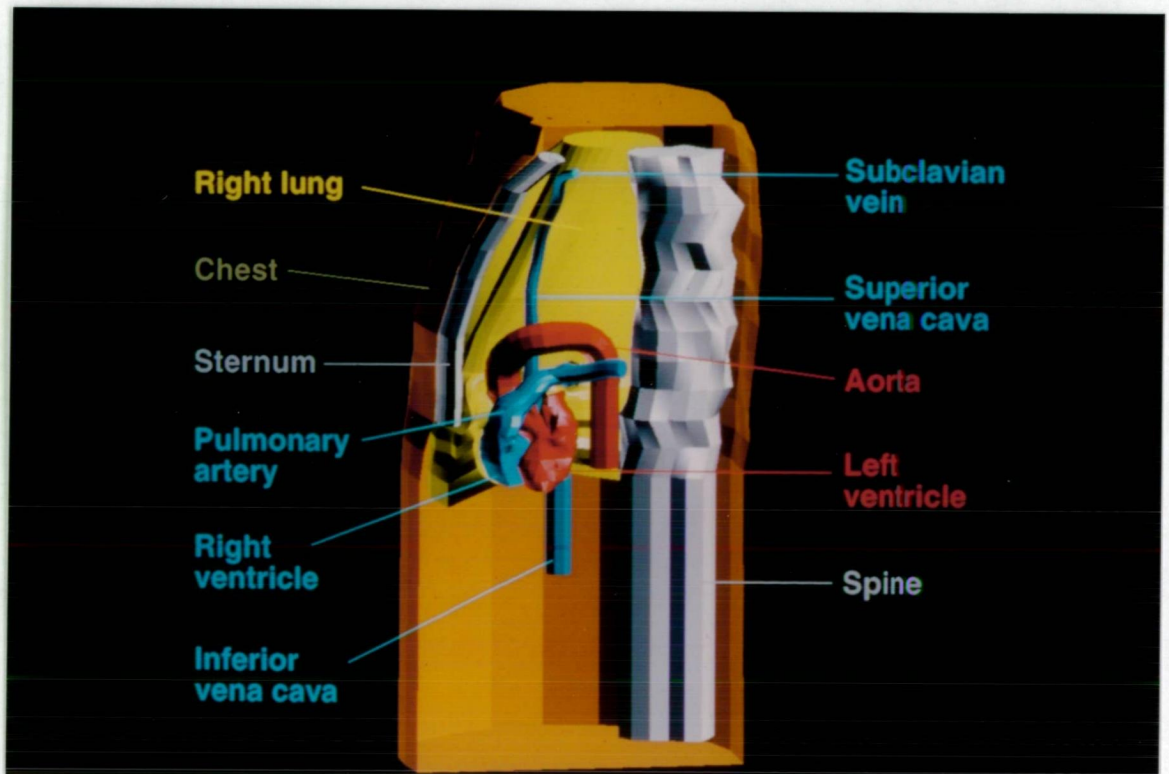


Plate 2: *Components of the boundary element human torso—in situ*

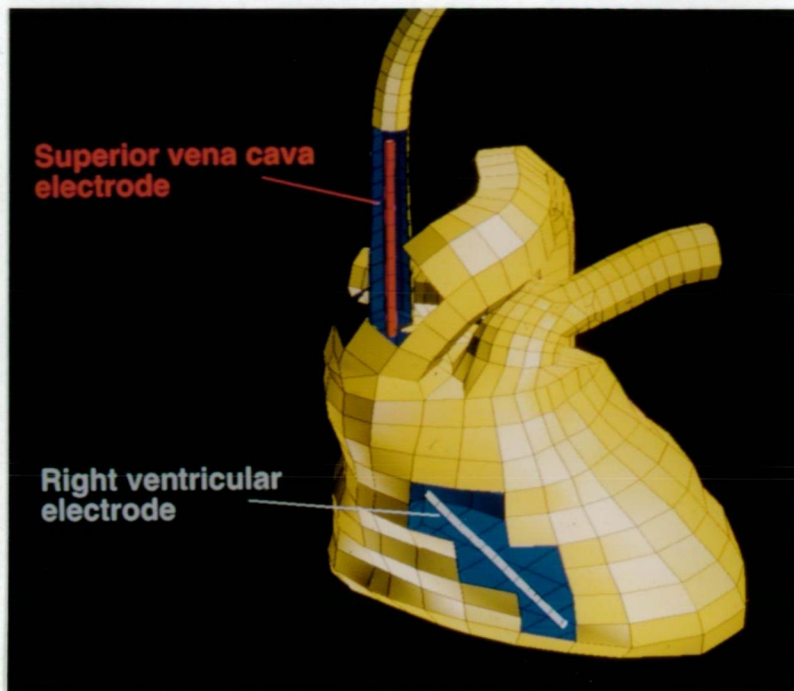


Plate 3: *Standard transvenous electrode configuration within heart (anode is red, cathode is white)*

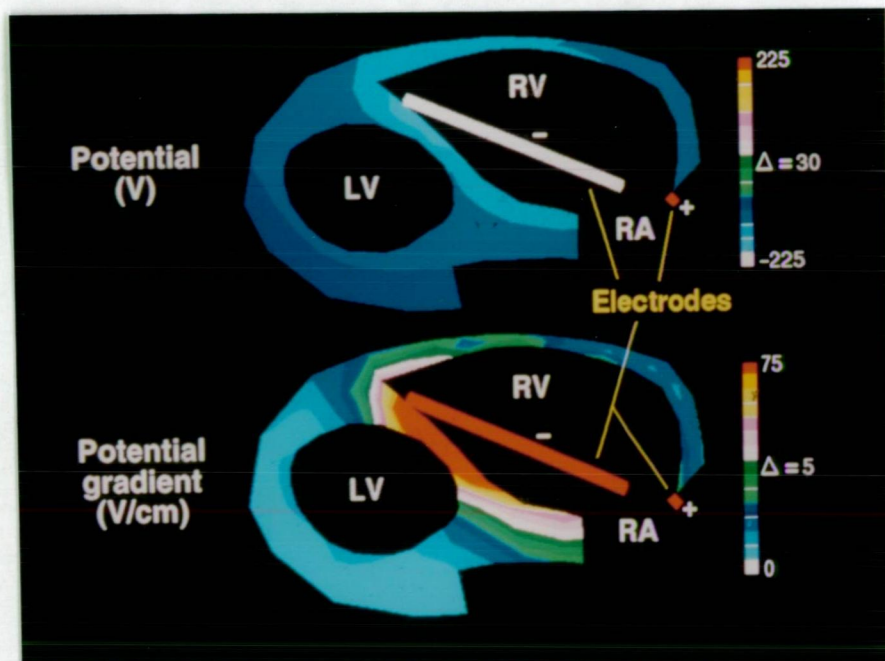


Plate 4: *Potential and potential gradient on a section through the ventricles. The electrode voltage (447V) was just sufficient for defibrillation, resulting in a potential gradient of at least 5V/cm everywhere within the ventricular myocardium.*

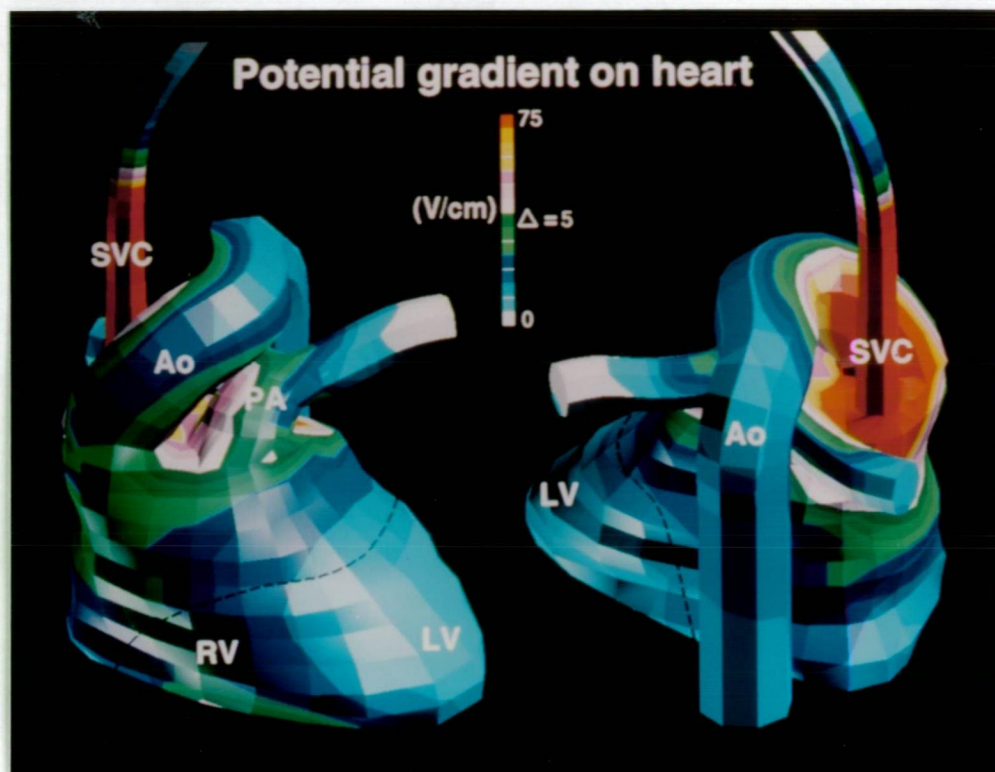


Plate 5: *Potential gradient on the heart for the standard transvenous electrode configuration. The electrode voltage was again 447V. The black dashed line marks the approximate extent of the ventricles.*

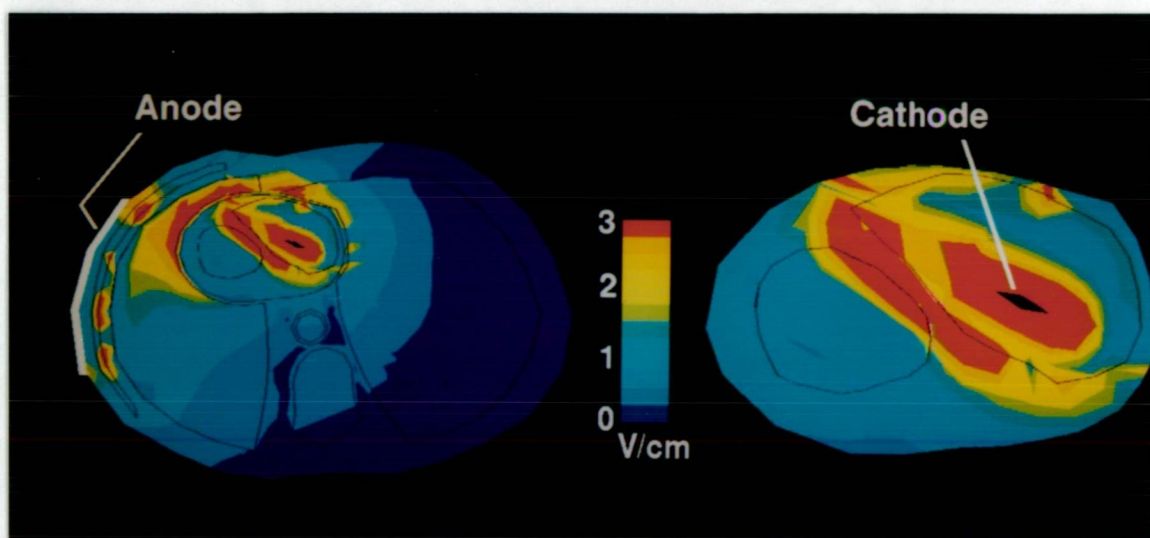


Plate 6: *Potential gradient on a section through the torso for the standard transvenous electrode configuration plus apical subcutaneous patch. The electrode voltage (215V) was just sufficient for defibrillation.*

# Chapter 1

## Introduction

This thesis is concerned with modelling the electric field produced by implantable defibrillators within the human torso. Implantable defibrillators are devices capable of delivering high voltage defibrillation shocks through implanted electrodes. They are used in patients to lower the risk of sudden death due to ventricular fibrillation. The technology and use of implantable defibrillators is advancing rapidly due to the rapid development of the devices, electrodes and surgical techniques and because of improved understanding of the mechanisms and principles of defibrillation.

A model of the electric field allows the potential effectiveness of a defibrillation shock to be assessed. In general, the effectiveness of a defibrillation shock depends on the torso structure, on the electrode configuration used to deliver the shock and on the electrical properties of the heart. The effectiveness of a shock from a particular electrode configuration can be assessed by firstly solving for the electric field. Then appropriate criteria can be applied to assess the suitability of the field for defibrillation and the shock strength required. Information can be obtained about the electric field that would be unavailable without the model. This can be used to optimise a system to a patient, to evaluate new ideas in regard to electrode configurations and to investigate otherwise hidden properties of the electric field.

The model developed in this thesis used Laplace's equation as the governing equation for the electric field in the torso. Laplace's equation was solved using the boundary element method applied to a discretised torso. The major structures of the torso were included in the model and each was assigned an appropriate value of isotropic conductivity.

The boundary element method had several advantages over a purely domain based method in this application. The advantages included discretisation using surface rather than volume elements, ease of modification of the discretised torso to match patient torso geometry, attainment of accurate values of potentials and gradients for many configurations without extensive re-meshing or mesh refinement and the avoidance of iterative methods and associated convergence issues.

Some approximations were made in the implementation of the model. These include the level of detail of some of the torso structures, the values used for tissue conductivity, the representation of the electrode-torso interface and the criteria used to determine defibrillation success.

The model was verified using a number of techniques to ensure adequate performance. These included verification against analytical, experimental and clinical results and also against a finite element model developed specifically for this purpose.

As part of the model implementation, a method was developed that significantly reduced the computation required when optimising electrode configurations. Various electrode configurations were then investigated and a number of developments were identified for future work.

The topics introduced above are addressed in the chapters that follow. The chapters are organised to deal with background material, relevant literature, numerical methods, implementation of the numerical methods, modelling of the thorax geometry, validation of the numerical methods, validation of the model in sheep and humans and results of investigations using the boundary

element model with various electrode configurations.

Before continuing, a note regarding the discussion of methods in the thesis. The methods relate to a number of quite different subjects and so separate methods sections were retained for each. The numerical methods command a whole chapter while the methods of the validations and investigations are included as sections within the respective chapters.

A further note is appropriate regarding the company referred to as Teletronics throughout this thesis. Teletronics was involved in this thesis as the industry partner in an Australian Postgraduate Research Award (Industry). The company details are: Teletronics Pty. Ltd., 7 Sirius Road, Lane Cove, NSW 2066, Australia.

# Chapter 2

## Biomedical Background

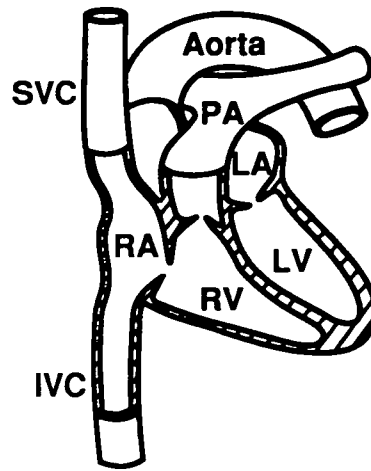
### 2.1 Introduction

This chapter presents background material relevant to the thesis on the heart (including the physical structure, electrical operation and mechanisms of fibrillation and defibrillation), the mechanism and criteria for successful defibrillation and how this may be included in a model, a description of implantable defibrillators and the defibrillation waveforms they generate and a glossary of terms associated with fibrillation and defibrillation. This chapter is, of necessity, brief. References to more detailed discussion of these issues are given in the appropriate sections.

### 2.2 Heart Structure and Function

#### Heart structure

The heart (Figure 2.1) is a hollow muscular organ with four chambers. The left and right atrium (LA and RA, respectively) are thin-walled chambers separated by the interatrial septum. The left and right ventricles (LV and RV, respectively) are thick-walled chambers separated by the interventricular septum and with the left wall thicker than the right. The pulmonary artery

Figure 2.1: *Heart structure*

(PA) exits from the right ventricle then branches left and right to the lungs. The aorta, the other major artery, exits from the left ventricle, loops over the heart and descends to the lower body, with branches that supply the mid- and upper body and the heart itself. The superior and inferior vena cava (SVC and IVC, respectively) are large veins from the upper and lower body that enter the right atrium.

In the pulmonary circulation, blood is pumped from the right ventricle through the pulmonary arteries to the lungs and returns through the pulmonary veins to the left atrium. In the systemic circulation, blood is pumped from the left ventricle, through the aorta to the arteries, arterioles and capillaries and returns through the venules to the veins and then to the right atrium. The systemic circulation is a high-resistance system with relatively high pressures (normally 90-140 mm Hg) generated by the action of the left ventricle. The left ventricle is consequently very muscular with thick walls. The pulmonary circulation has a much lower resistance and is a relatively low pressure system (normally 15-28 mm Hg). The right ventricle is therefore not as thick as the left ventricle.

There are four interconnecting fibrous rings that surround the openings between the atria and ventricles and between the ventricles and great arteries.

Apart from having mechanical functions, these rings electrically isolate the ventricular and atrial muscle.

### **Heart's conducting system**

The body's natural system for stimulating heart contraction is through the heart's conducting system. The conducting system starts with the pacemaker region (the sinoatrial or SA node) located in the groove between the superior vena cava and the right atrium, which starts the heartbeat by generating a pacemaker potential. This potential spreads through the right atrial myocardium. The atrioventricular (or AV) node receives this potential and conducts it to a bundle of conductive fibres known as the AV bundle, or bundle of His, which passes through the atrioventricular septum and branches left and right down the interventricular septum. This is the only electrical connection between ventricles and atria in the normal heart. These branches pass under the endocardium and divide into a further number of branches (Purkinje fibres) that finally connect to the cardiac muscle fibre. The potential travels through this conduction system and stimulates ventricular contraction.

### **Normal electrical activity of heart muscle cells**

Normal cardiac rhythm consists of rhythmic contraction and relaxation of the heart muscle. The potential delivered from the pacemaker region through the heart's conducting system triggers depolarisation in cardiac cells in contact with the Purkinje fibres. The action potentials from these cells trigger the next cells, and so on. Previously activated cells are inhibited from immediate re-activation due to a refractory period after the action potential and this ensures activation occurs as travelling wavefronts through the myocardium and also that the activation, having started at the sinus node, dies out after the last ventricular cell has been activated.

The cardiac muscle fibres contract and relax in response to the electrical

stimuli generated by individual cardiac cells. The stimuli are electric potentials generated by ionic changes in the cells, made possible by the cell's ionic composition and semi-permeable membrane. The membrane has a differential permeability to ions which is dependent on the cell's state of activation.

The most important diffusable ions are calcium, potassium and sodium. At rest, there is a high concentration of potassium inside and of sodium outside the cell, resulting from the differential permeability of the cell membrane to these ions. It is this, primarily, that causes a potential difference, or polarisation, of between  $-70$  to  $-90mV$  found between the outside (reference) and inside of the resting cell. This potential is effectively an equilibrium potential resulting from the ionic imbalance.

Cardiac cells are activated by a change in the resting transmembrane potential. The first stage of activation is depolarisation, a rapid influx of  $Na^+$  followed by a slower influx of  $Ca^{2+}$ , resulting in the release of calcium ions from the sarcoplasmic reticulum (semi-fluid matrix of the muscle fibre) into the myofibrils (the active contractile component of the muscle fibre) which activates the contractile process. Depolarisation occurs very quickly and results in the cell transmembrane potential rising to approximately  $10mV$ . This is followed by the relatively slow repolarisation of the cell. This sequence lasts approximately  $200msec$  and is called the action potential.

The electrical response of the heart has the property that the magnitude of the response may be greater than the stimulus. In this sense, the heart's electrical response is nonlinear.

### **Ventricular fibrillation**

Ventricular fibrillation is a life-threatening state where there is an uncoordinated and ineffectual chaotic rhythm with the result that the ventricular muscle no longer contracts and relaxes normally. This confused, self-sustaining state results from disturbance to the normal activation sequence in the myocardium

and leads to activation wavefronts proceeding abnormally.

The mechanism for initiation and self-sustaining of ventricular fibrillation is, in many cases, thought to be some form of re-entrant loop activity, a pattern of myocardial activation that travels a closed path and is self-propagating. A re-entrant loop starts with a region of unidirectional conduction and completes with the right timing for the myocardium to be ready for re-activation when the activation front returns. The loop may occur around an obstacle, such as the orifice of the aorta, the pulmonary artery or scar tissue. In myocardium that has normal conduction rates, loops would be expected to be at least 10cm long [3] so for more realistic small loops to form there must be regions of slow propagation in the loop. Slow propagation will occur if the myocardium is activated in the refractory period, which may happen with abnormal (such as ischaemically injured) myocardium.

Functional re-entry is another mechanism for re-entry where the loop travels not around an obstacle but around tissue that remains refractory [4]. This type of loop starts in a region where there is an abnormal distribution of refractoriness. The wavefront circulates around a region that remains refractory due to wavelets emanating from the wavefront travelling into the region and colliding, their refractory wakes resulting in annihilation of the wavelets.

Other forms of re-entrant activity have been suggested. Spiral wave activity [5], for example, is a re-entrant activity that relies on the nonlinear behaviour of impulse propagation in cardiac muscle.

The nonlinear behaviour of cardiac muscle leads to the question of whether ventricular fibrillation is chaotic. In this sense, chaos refers to aperiodic, irregular dynamics in deterministic systems where dynamic behaviour is determined by definite laws [6]. It seems that there are conflicting viewpoints to this question [7, 8, 9] which remains unresolved.

## Ventricular defibrillation

The following discussion will consider the determinants of defibrillation, including the shock strength and distribution required for defibrillation to be successful, bearing in mind that the precise mechanism of defibrillation with electric shocks is still not fully understood and that the theory of defibrillation is still evolving. This section will provide the background on how success or failure of defibrillation may be included in the model.

Defibrillation involves halting the fibrillation activation wavefronts. This is normally done by applying an electrical stimulus which depolarises all or most of the ventricular myocardium rendering it refractory. In the refractory state wavefronts can not exist so fibrillation ceases. Fibrillation can spontaneously re-occur if insufficient myocardium is depolarised by the stimulus or the electrical stimulus is too weak or too strong.

The strength of a defibrillation shock is generally described in terms of potential gradient or current density. The distribution of this shock in the myocardium is determined by the position and structure of defibrillation electrodes, the voltage waveform applied and the shape and structure of the heart and thorax. For successful defibrillation, the shock strength must be within certain limits. According to Ideker, *et al.*, “To defibrillate, a shock must halt the activation fronts of fibrillation without giving rise to new activation fronts that re-induce fibrillation” [1]. Recently proposed mechanisms of defibrillation have considered the ability of the shock to initiate new activation fronts and to alter refractoriness [1].

**Critical mass** Early proposals for the method of defibrillation, based around halting activation fronts, involved halting fronts in all of the myocardium [10, 11]. Later, it was proposed that activation fronts need only be halted in a “critical mass” of myocardium [12, 13], which was postulated to be around 75% of the ventricular mass (from experiments in dogs). It was thought that

activation fronts in the remainder would not be self-sustaining and would die out. More recently, information obtained using cardiac mapping techniques indicates the critical mass is at least 90% of the ventricular mass [14].

**Minimum shock strength** Even though a low gradient field may halt the activation fronts during defibrillation it is possible for new activation fronts to arise leading to the resumption of fibrillation. To prevent new activation fronts arising, a much larger shock than the minimum to halt activation fronts must be applied. Minimum potential gradients of 5 to 6V/cm [15] and 4 to 9V/cm [16] have been suggested as the minimum required if the shock is monophasic. A minimum current density of  $35 \pm 5mA/cm^2$  [17] has also been suggested, corresponding to approximately 10 – 20V/cm, depending on the conductivity of the myocardium. Winfree suggests a minimum current density of approximately  $20mA/cm^2$  based on empirical considerations of the heart's electrical responses [18]. Zhou, *et al*, found post-shock activation fronts were prevented by potential gradients greater than 5V/cm [14].

Shocks of this magnitude raise all the myocardium above the upper limit of vulnerability (the maximum stimulus beyond which fibrillation is not evoked) so that the myocardium remains unexcited after the shock thereby inhibiting the development of new activation fronts and preventing the re-establishment of fibrillation.

There is no sharp cut-off in the relationship between shock strength and defibrillation success, rather there is a dose-response type curve, as illustrated in Figure 2.2. Strong shocks have a higher chance of success than weak shocks. A very strong shock will virtually guarantee defibrillation while a very weak shock will usually fail. When discussing defibrillation, it is usual to refer to a ventricular defibrillation threshold (DFT) which is usually defined as the shock strength giving a 50% (or sometimes 80 or 90%) probability of success.

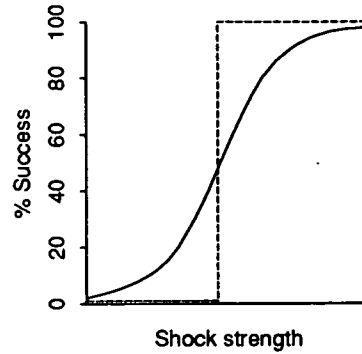


Figure 2.2: *The probability curve for defibrillation (from Ideker et al. [1])*

**Maximum shock strength** As we have seen, it is necessary to apply a relatively large shock to virtually all of the myocardium for successful defibrillation. It is important, though, not to apply an excessively large shock as this may cause the resumption of fibrillation and temporary or permanent damage to the myocardium. Potential gradients above  $60V/cm$  temporarily disable pacing and conduction [19] while a potential gradient of  $80V/cm$  is sufficient to induce permanent damage to myocardial cell cultures [20].

Babbs *et al* [21] investigated the ability of transchest defibrillator shocks to produce defibrillation, myocardial damage and death in 101 dogs. Damage was assessed by physical examination of the myocardium. They found that damage occurred at 5 times the current and 20 times the energy required for defibrillation, and death occurred at 22 times the current and 320 times the energy for defibrillation. Also, the risk of detectable damage was 2 to 4% for 90% successful shocks and 5 to 10% for 99% successful shocks.

**Monophasic versus biphasic waveforms** Waveform shape also influences defibrillator performance. As biphasic waveforms have been found to be more effective than monophasic, it has been suggested that different mechanisms of threshold reduction may operate [22]. Blanchard and Ideker discuss possible mechanisms that increase biphasic over monophasic efficacy, including less conduction block in regions of high potential gradient, lower potential gradient

required for defibrillation in low gradient regions, less ability of some biphasic shocks to stimulate the myocardium and the effect of the second phase on reversing or returning the transmembrane potential to its original level [23]. There has also been evidence against the extension of the refractory period with biphasic shocks [24].

Zhou, *et al*, found potential gradients of approximately  $5V/cm$  for monophasic waveforms and  $3V/cm$  for biphasic gave an 80% chance of successful defibrillation [14]. They found no clear reason for the greater efficacy of the biphasic waveform.

**Spatial variation in minimum shock strength that induces fibrillation** There is spatial variation in the shock strength needed for fibrillation. Horowitz, *et al*, found the shock strength needed was at least 50% higher in the left ventricle than in the right ventricle [25] while Burgess, *et al*, found the shock strength needed to be higher in the anterior than the posterior wall of the left ventricle [26].

**Variation in required shock strength between patients** Hillsley, *et al*, discuss high defibrillation thresholds in some patients [27]. They say that

“A high defibrillation threshold may occur because: (1) a shock creates a subthreshold potential gradient in the low gradient areas; (2) a patient has a higher minimum potential gradient threshold than other patients; or (3) a shock leads to refrillation in the high gradient areas.”

As always, the natural variation within humans means it is difficult to interpret the clinical data.

There is still considerable debate about the actual mechanisms of defibrillation and the reasons why there is a dose-response curve, but while the exact

mechanisms of defibrillation are still to some degree uncertain, a workable criteria for defibrillation is that the defibrillation threshold (DFT) is the shock strength giving a minimum potential gradient everywhere in the myocardium of approximately  $5V/cm$  (for monophasic waveforms) and a maximum not exceeding approximately  $80V/cm$ . This is the criteria that will be used in the model that is the subject of this thesis.

It has also been shown that defibrillation response is partly dependent on electrode polarity [28], though the reasons for the dependance are not fully explained. The above defibrillation criteria is therefore a simplification of the true mechanism of defibrillation as it does not take into account the dependance on polarity. While it is desirable to avoid such a simplification, the rigorous treatment of polarity dependance is beyond the scope of this thesis.

## 2.3 Early History of Defibrillation

In 1899 Prevost and Battelli found that ventricular fibrillation was induced by applying alternating current (AC) directly onto the heart of animals [29]. They also found that stronger intensity AC applications and capacitor discharges could be used to defibrillate the heart. Their AC results were confirmed in 1930 by Langworthy and Kouwenhoven, who also suggested that the defibrillating shock needed to affect the entire heart to be successful, and showed a ventricular fibrillation duration of two minutes or more generally led to death [30, 31, 32]. Prevost and Battelli's capacitor discharge results were confirmed in the 1940's by Gurvich and Yuniev [33]. The first successful human defibrillation was in 1947, using a 110V AC device with the heart exposed [34]. This technique required immediate thoracotomy. Zoll, in 1955, performed the first transthoracic defibrillation, using 240-270V AC and 7.5cm diameter copper electrodes [35]. At this stage, AC, rather than DC, waveforms were established as the preferred method of defibrillation.

Lown, *et al*, in 1962, found that direct current (DC) shocks with a damped sinusoidal waveform reduce the chance of post-shock arrhythmias and electrocardiographic repolarisation changes (in dogs) [36]. This work led to the recognition of the superiority of damped sinusoidal DC waveforms over AC waveforms. DC defibrillators were subsequently developed that were small and could be battery powered and therefore portable. These defibrillators still needed a relatively large inductor to generate the required waveform.

During the 1960's and early 1970's, truncated exponential waveforms were recognised as effective waveforms that eliminated the need for an inductor [37, 38, 39, 40]. This advance was one of the factors that enabled the development of an automatic defibrillator that could be implanted in humans.

Further and more complete discussion may be found in articles such as those by Troup [41] and Mitrani *et al* [42]. The discussion of implantable defibrillators is continued in the following section.

## 2.4 Implantable Defibrillators

The implantable defibrillator was developed independently by the groups of Mirowski [43] and Schuder [44]. These early proponents of implantable defibrillators encountered spirited discussion with their peers, including, for example, a disparaging editorial by Lown and Axelrod [45]. They implied implantable defibrillators were impractical because of potential electrical injury to the heart and difficulty in determining satisfactory electrode positions because of “the complex geometry and electrophysiologic properties of a particular heart which cannot be readily modelled”. They even went on to say “...the implantable defibrillator system represents an imperfect solution in search of a plausible and practical application” and likened an implantable defibrillator to an electronic gadget that “was developed only because it was possible”. This discouragement, though, most likely reflects the magnitude of the difficulties involved

with developing the implantable defibrillator, and the scepticism surrounding its feasibility.

In spite of the discouragement, Mirowski's group continued with the development of the implantable defibrillator. They overcame problems relating to miniaturisation of the device, determination of effective energy levels, selection of an appropriate waveform and electrode configuration, development of special power sources and creation of a reliable sensing system [46]. Early tests of the implanted system in dogs were successful [46] and were followed by trials in humans [47], leading to approval by the USA Food and Drug Administration in 1985 and manufacture by Cardiac Pacemakers, Inc. Since then, many types from various manufacturers have been approved and the implantable defibrillator is now in widespread use, with good acceptance by the medical community.

A typical implantable defibrillator system (Figure 2.3) consists of a pulse generator connected to implanted electrodes. The pulse generator contains capacitors which are charged from batteries then discharged between implanted electrodes. Pulse generators have a titanium shell and generally use two lithium silver vanadium oxide batteries to supply a total of  $6.4V$  to the defibrillator circuitry. The circuitry enables the defibrillator to be programmed to sense the heart's electrical or physical activity and to deliver the appropriate response, and incorporates voltage multiplication circuitry to attain high voltage output for defibrillation. Defibrillators weigh from about  $240g$  for older models to just over half that for new models. Defibrillation output is up to  $40J$  and  $750V$ .

Implanted electrodes were originally titanium mesh patches that were sewn to the epicardium. Although efficacy was good, implantation required thoracotomy with associated complications and mortality. Transvenous lead systems were introduced in 1993 [48, 49] and were associated with less serious complications and decreased mortality from implantation. Transvenous leads

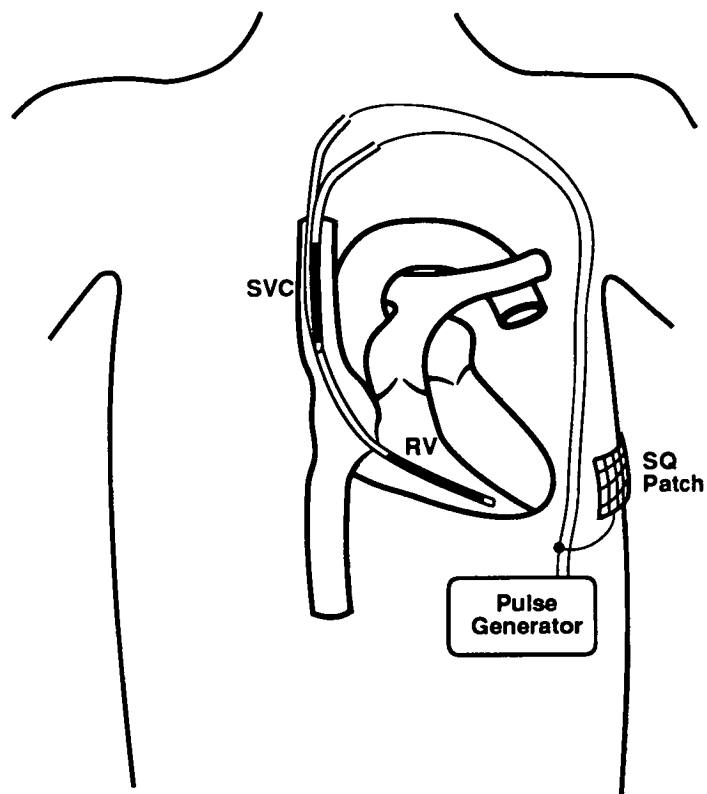


Figure 2.3: *Example of a common implantable defibrillator system, with a pulse generator, transvenous electrodes in the right ventricle (RV) and superior vena cava (SVC) and a subcutaneous (SQ) patch electrode*

are implanted through the venous system and consist of small diameter leads incorporating sensing, pacing and defibrillating electrodes. Typically, one defibrillator electrode is positioned in the right ventricle combined with at least one other electrode. Possibilities include transvenous electrodes in the right atrium, coronary sinus or superior vena cava, subcutaneous patches or the pulse generator casing. Sometimes combinations are used without a right ventricular electrode.

## 2.5 Defibrillator Voltage Waveforms

Many defibrillator waveforms (Figure 2.4) have been tested with different degrees of success. The descending ramp (a) has been found to have a high likelihood of failure, probably because of the descending tail [50], while square waves (b) are more effective [51]. AC waveforms (c) are successful [34, 52], but are disadvantaged by their need for large transformers and gated output [53] and their tendency to induce atrial fibrillation [36]. Damped sinusoidal waveforms (d), though, are effective [54, 55, 36] and are used in most commercially available external defibrillators [56].

The capacitor discharge (e) is a simple waveform which, unfortunately, produces unpredictable outcomes since the long tail can re-induce fibrillation [50], and which requires about twice the energy of a damped sinusoidal waveform [54]. Truncated exponential waveforms, though, are effective and are used extensively. Three types of truncated exponential waveforms used are monophasic, biphasic and sequential (f, g and h). The efficacy of monophasic waveforms is comparable to that of damped sinusoidal waveforms [57]. Recently, though, the superior efficacy of the biphasic waveform has been shown [58, 59, 60, 61, 62, 63] and it is now commonly used in implantable defibrillators. There has been no conclusive evidence that sequential waveforms are superior to monophasic [64, 65].

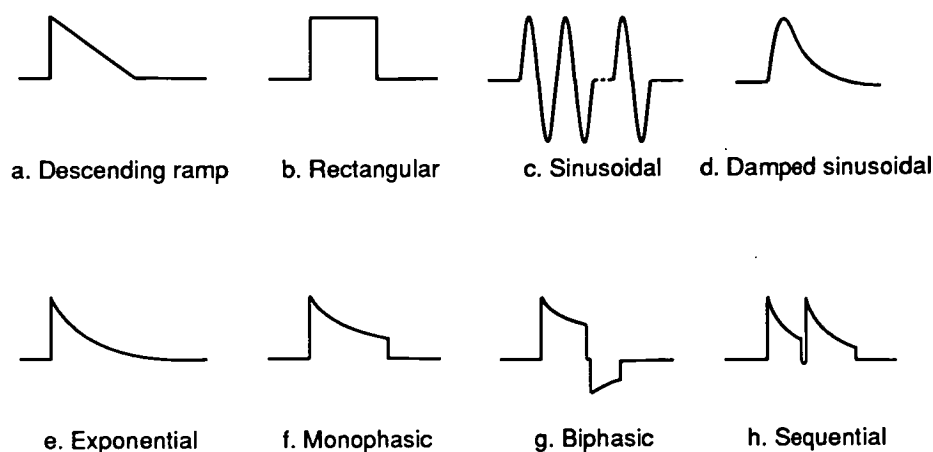


Figure 2.4: *Examples of potential defibrillator waveforms, plotted as voltage versus time. Truncated exponential, biphasic and sequential waveforms are commonly used with implantable defibrillators.*

## 2.6 Glossary

### Ventricular fibrillation threshold

The ventricular fibrillation threshold (VFT) is the minimum stimulus that will evoke fibrillation and is usually specified in terms of voltage or energy.

### Vulnerable period

The vulnerable period is the period of ventricular activation during which fibrillation is most easily induced. This is the repolarisation interval of normal rhythm.

### Defibrillation threshold

The ventricular defibrillation threshold (DFT) is a measure of the shock strength required for successful defibrillation. In practice, this is usually the shock giving a 50% probability of success.

**Myocardium**

The heart muscle.

**Epicardium**

The outside surface of the heart.

**Endocardium**

The inside surface of the heart.

**MRI**

Magnetic Resonance Imaging.

**CT**

Computerised Tomography.

# Chapter 3

## Literature Review

### 3.1 Introduction

This review will focus on modelling of the electric field in the torso, particularly numerical models of implantable defibrillators, but also the related issues of the electrical properties of tissues, the interface between electrodes and the torso, the construction of torso geometry for models, the numerical solution strategy employed in models, model validation and the optimisation of electrode configurations. The review will also include discussion of defibrillation threshold and resistance values that have been measured in humans from use of implantable defibrillators with numerous electrode configurations.

### 3.2 Modelling

The modelling of the electric field in the torso considered in the thesis fits into the category of forward models of electrocardiology. In forward models, sources of potential in the torso are known and the electric field is calculated, given the structure of the torso. This is distinct from inverse models, where knowledge of the surface electric field is used to find unknown source potentials. We will consider various models that have been developed to date and, in particular,

those models that predict the electric field of defibrillators.

### **Torso models**

Early models of the electric field in the torso include both physical and analytic models. Physical models include those of Burger and Milaan [66], Nelson *et al* [67] and Rush [68]. These models used resistor networks, electrolytic solutions, tanks, bladders, electrodes, and so on, in their construction making them time-consuming to create and modify. Though often ingenious in concept, they also often had limited application. Analytic models include those of Rush and Nelson [69] and of Rudy and Plonsey [70]. These were used to arrive at various theoretical predictions, but, were limited by the degree of complexity of torso structure that could be represented.

Numerical models became feasible with the advent of the modern computer in the 1960's and 1970's. In a numerical model, the electric field can be found using potential theory by solving Laplace's equation [71], which applies in this case because torso tissue is almost purely resistive at low frequencies. Initially, numerical torso models were often limited to two-dimensions to match their size and complexity to the early computers. Increases in computer capacity and processing power subsequently allowed realistic three-dimensional models to be developed. Some of the limitations of two-dimensional models were that representation of three-dimensional geometry was often unsatisfactory, values for electrode resistance, defibrillation voltage and energy was often in gross error, and electrode configurations were often unrealistic. Sepulveda *et al* [17], for example, developed a two-dimensional finite element model of the canine heart and torso and used it to compare a number of implantable defibrillator electrode configurations. The model included muscle, lung, myocardium and blood with isotropic conductivities. Although the model was useful to some degree, some of their findings, such as the shunting of current through the blood when using a two-electrode catheter, were exaggerated because the field

was constrained to be two-dimensional and because it was only possible to space the electrodes close together.

The remainder of the discussion will be of three-dimensional models. Numerical torso models developed in the 1960's include those of Gelernter and Swihart [72] and Gelernter *et al* [73], who calculated torso potentials using integral equations for a hemispherical dipole layer within a torso. Another was developed by Barnard *et al* [74], who used a unit dipole source and realistically shaped blood masses. Selvester *et al* [75] and Cuffin and Geselowitz [76] used 20-dipole heart models within a torso that included lungs. They found that the body surface potentials were not changed much by inclusion of the lungs.

Horacek [77] developed a model in the early 1970's which was modified by Gulrajani and Mailloux [78] a decade later. They used an integral equation approach to study the effects of inhomogeneities on the electrocardiogram, vectorcardiogram and the body surface potential map. Their model included the torso surface, lungs and the heart's blood masses. The anisotropic-conductivity skeletal muscle layer was taken into account by the boundary-extension method, with the body surface moved outward, as suggested by Rush *et al* [79]. In the mid 1980's, Stanley *et al* also used Rush's boundary-extension method [80], and then discussed its accuracy [81], concluding that it could be utilised only for regions of constant anisotropy and was only accurate for flat or slowly changing surfaces.

Also in the mid 1980's, Walker and Kilpatrick [82, 83] developed models for the forward and inverse problem of electrocardiology. These were based on a finite difference method using a resistive network and included the heart, lungs, spine and sternum. The models defined the torso geometry using a mesh constructed from digitised CT scans. Each mesh contained approximately 20,000 nodes, arranged with a variable spacing to attain an increased density near the heart. Although the node spacing was irregular, the sides of each element were constrained to be parallel, to satisfy the requirements of the

finite difference method. In a later study of acute inferior myocardial infarction Kilpatrick et al [84] recorded body surface potentials of 219 patients and then used the inverse model to calculate epicardial potential maps. They found that 31% of the patients had two characteristic dipole patterns on their epicardial maps and that these patterns were associated with a mortality rate of 35% compared with 5% in the remaining patients.

In the late 1980's and early 1990's, Stanley and Pilkington [85, 86] presented a numerical method for electrocardiographic potential calculations which combined the boundary and finite element methods. They were the first to apply the combined method to an electrocardiographic calculation. The advantage of the method was in finding potentials in a volume that had both isotropic and anisotropic regions. The advantages of the boundary and finite element methods could be exploited in the respective regions.

This decade, Johnston and Kilpatrick [87, 88] developed a boundary element model of the forward problem of electrocardiology. The model mapped the potential from the epicardial and endocardial surfaces of the heart onto the body surface. The model used approximately 5000 linear quadrilateral elements and included the heart, lungs, spine, sternum and general body tissue. The heart was subdivided into regions of heart muscle and blood, with the blood providing an electrical pathway from the endocardium to the body surface. The electric field at the body surface was found to be influenced by this previously omitted electrical pathway.

Recently, Pullan *et al* [89] developed a coupled boundary and finite element torso model for use in the forward (and inverse) problems of electrocardiology. This model used higher order elements, which made creating the mesh difficult but resulted in good definition of the surfaces with few elements. Meshing the epicardium, lungs, skeletal muscle, fat and outer torso required only 658 elements. The coupling of boundary and finite elements allowed finite elements to be used in regions of anisotropic conductivity.

### Defibrillation models

Defibrillation models have been developed for both transthoracic and implantable defibrillators. Most of the relevant literature is work that has been done concurrently with the work described in this thesis and has been reported only in conference proceedings.

A volume conductor model of the torso was developed by Claydon *et al* [90] for the study of defibrillation fields in the late 1980's. The model included skeletal muscle surrounding a body compartment containing the lungs and heart. The model represented skeletal muscle by the boundary-extension approximation of Rush (discussed above), allowing this anisotropic region to be represented as isotropic. The simplified heart was modelled as isotropic and without cavities. They used boundary integral equations to predict epicardial potentials from a transthoracic stimulus and compared this to measured values in experiments on three dogs. They found average RMS error and correlation coefficient of 47.3% and 0.901, respectively, for a homogeneous torso with or without lungs (!), and 42.1% and 0.914 with the skeletal muscle layer. The relatively good correlations were surprising considering their model had very simple geometry and only a relatively small number of nodes to represent the body structure. It is also surprising that the inclusion of the lungs had no discernible effect, especially considering the low conductivity of the lungs.

There have been a number of recent conference papers relating to models for transthoracic defibrillation. Karlon *et al* [91] developed a finite element model of the canine torso for use in the study of transthoracic electrical defibrillation. The model was constructed from 21 cross-sectional CT scans, each separated by 0.82cm. Eight distinct tissues were incorporated, including anisotropic properties of skeletal muscle. The model contained approximately 9,000 nodes and 45,000 linear tetrahedral elements. Results obtained using the model were found to compare well with published *in vivo* experimental data.

A transthoracic defibrillation model was developed by Camacho *et al* [92, 93]. The torso was of an average adult male torso constructed from 22 serial cross-sectional CT scans spaced 1cm apart obtained from an atlas of computerised tomography [94]. The model included 130,000 linear tetrahedral finite elements defined by 23,000 nodes with isotropic conductivities for cardiac muscle, liver, lung, bone, blood, skin, fat, mediastinum and anisotropic conductivity for skeletal muscle. In one study [92], they compared 4 defibrillator paddle pairings and 2 paddle sizes. They used a critical mass criterion that 75% of the heart needed to be exposed to a threshold current density of at least  $30mA/cm^2$  for defibrillation to be successful. They found that none of the myocardium was exposed to current densities greater than four times the threshold, noting that myocardial damage has been found with current densities of ten times the threshold or more. The fraction of total current flowing through the myocardium was 20 – 45%, which was within the range estimated by others, and impedance values were similar to reported human transthoracic impedance. They concluded that the agreement between their finite element model results and physical measurements of others suggested that finite element modelling provided a reasonable description of the conduction process during defibrillation. In a further study [93], they considered the effects of epicardial patch electrodes on transthoracic defibrillation. They found that the presence of conformal patches on the epicardium increased the current necessary for defibrillation by up to 33%.

A boundary element model of transthoracic defibrillation was developed by deJong *et al* [95]. The torso was constructed from 90 transverse MRI images of the human torso, using 1008 triangular elements for the torso surface and 480 for the epicardium. Although not included in this model, they also constructed surfaces representing the fat, skeletal muscle, lungs, spine and endocardium. From knowledge of the defibrillation electrode position and voltage, they calculated the applied intrathoracic current and epicardial potentials, and from

these the epicardial current distributions and amount of transcardiac current, which was within the range of 21 – 31% of the total electrode current.

Patterson and Wang [96] developed a finite difference model for external defibrillation. The torso geometry was constructed from 40 MRI scans at 1cm spacings from an adult male and contained 216,000 elements. Values of resistivity used in the model were measured in their laboratory and had values of  $150\Omega\text{cm}$  for blood,  $400\Omega\text{cm}$  for myocardium,  $400\Omega\text{cm}$  for skeletal muscle,  $1400\Omega\text{cm}$  for lung and  $2000\Omega\text{cm}$  for fat and bone. They compared the performance of different electrode sizes and positions finding that from 16% to 23% of the total current flowed through the heart.

Cansell *et al* [97] developed a resistor network finite difference model for finding the electric field from implantable defibrillators. They used the model to find the optimal position of electrodes in a right-ventricular to multiple subcutaneous patch configuration and compared this to results found experimentally on pigs and dogs. It seems they found good agreement between the model and pig experiments, though their discussion was not particularly clear on this point. However, they did find that their experiments on pigs were more valuable than those on dogs because the anatomy and size of pigs more closely matched humans. Electrode positions in pigs had a significant effect on defibrillation thresholds, whereas in dogs, electrode positions were found to have only a small effect.

There have been a number of recent conference papers relating to models of implantable defibrillators. A FE model of the human torso was used by Kinst *et al* [2] to find the electric field from epicardial, endocardial and subcutaneous electrodes. This appears to be basically the same model used by Camacho *et al* [92, 93] but used with internal rather than external electrodes. They found values of inter-electrode impedance and defibrillation threshold voltage and current to be comparable to reported clinical values. Their calculated impedance and voltage, and energy derived from these assuming a  $150\mu\text{F}$

Pairing	$Z$ ( $\Omega$ )	$V_{th}$ ( $V$ )	Energy ( $J$ )
epi-conform	36	253	4.44
epi-32	49	318	6.49
epi-16	72	430	10.1
RV-10 to SQ	71	733	29.5
RV-5 ro SQ	76	689	25.1
RV-5 to SVC-5	46	537	18.9

Table 3.1: *Internal defibrillation simulation results (from Kinst et al. [2]). Epicardial patch pairs were:  $54\text{cm}^2$  conformal (epi-conform),  $32\text{cm}^2$  (epi-32) and  $16\text{cm}^2$  (epi-16). RV-10, RV-5 and SVC-5 designate location and length (in cm) of endocardial electrodes and SQ was a  $25\text{cm}^2$  subcutaneous patch. Energy was derived assuming  $150\mu\text{F}$  capacitor and  $7\text{ms}$  pulse.*

capacitor and  $7\text{ms}$  pulse, is shown in Table 3.2.

Some finite element models have been based on a regular grid approach. One such model was developed by Seneta and Holley [98] for implantable defibrillators. The model was based on a regular orthogonal mesh using linear tetrahedral elements combined to form cubic structures. In concept, the model was similar to to a finite difference model, with similarly short solution times due to the regular mesh. The main disadvantage with the model is that the enforced regularity of the mesh means it is impossible to have local concentrations of nodes if required for physical or computational accuracy. This may result in difficulties when modelling fine anatomical structures, small electrodes or regions of large potential gradient. Another model was developed by Gao *et al* [99], who dealt with the resolution difficulties of regular grids by using a very fine grid combined with a massively parallel computer to do the computations. Using over 4 million nodes they could arrive at a solution in less than 10 minutes for a three dimensional anisotropic medium.

In 1995, Jorgenson *et al* [100] described a finite element model for transthoracic and transvenous defibrillation. Their model contained approximately 400,000 nodes and hexahedral elements arranged as a uniform mesh. They

found that commercial packages using banded matrix solvers could not handle their large problems (running on an IBM RS/6000 with 128 Mbytes of memory) so they successfully implemented their own solver using a Gauss-Seidel iterative scheme with over-relaxation. The torso mesh used was constructed from 56 transverse CT scans at 6mm intervals of an adult male human. They used a fast scanner and radiopaque contrast material to enhance the CT images and allow detailed anatomy of the heart to be extracted. They averaged blocks of 4x4 pixels on each scan and the resulting pixels were used as nodes in the model. Tissue was classified as either skin, fat, skeletal muscle, blood, bone, lung internal air, myocardium, gut or liver using an image segmentation algorithm followed by manual completion of unresolved or incorrect classifications. The myocardial tissue was represented by 6611 elements. They tested the model's sensitivity to tissue resistivity values and electrode size and position. To validate the model results, they predicted thoracic voltages in 3 experimental animals, finding squared correlation coefficients between experimental and calculated voltages from 0.89 to 0.98, indicating excellent agreement.

It is possible to automatically optimise electrode position by repetitively solving the model using appropriate optimisation algorithms to suggest modifications to the electrode configurations. Seneta and Holley [101] developed a program to automatically optimise electrodes for a number of geometric and performance criteria when used with their regular grid finite element model [98]. The optimisation algorithm used was "very fast simulated re-annealing" [102] and the performance criteria included bounds on electrode positions and goals such as maximising the magnitude or uniformity of the electric field. A cost function determined how closely the results from the finite element model matched the user-defined goal and the optimisation algorithm found the global minimum over the range of variation of the parameters. Hutchinson and Kwong [103] developed an optimisation algorithm for a finite element transcardiac defibrillation model. Their method was to optimise for

electrode position and voltage using current density in the myocardium as the performance criteria and the quasi-Newton optimisation algorithm [104].

### **Torso construction**

Min *et al* [105] developed a detailed torso geometry suitable for use in a finite element model. They used 49 CT slices with 6mm separation covering the torso from neck to diaphragm. They first generated two-dimensional contours to classify the boundaries of 27 tissues or organs of interest. They generated three-dimensional solids from these contours using commercial solid modelling software (IDEAS by SDRC, Milford, OH) or a Delauney mesh generator [106, 107] after defining an electrode geometry. Their method of torso construction could realistically represent anatomical and electrode geometry which, they suggest, may be difficult to do using simpler techniques (brick elements, for example).

The high order mesh developed by Pullan *et al* [89] was developed from an array of points on MRI slices at 5mm separation defining the boundaries of the lungs, heart, skeletal muscle, fat and outer torso. One dimensional cubic hermite elements were fitted to the points using a finite element procedure that minimised the root mean square (RMS) error of the orthogonal distance of the data points to the mesh. The two-dimensional boundaries were then connected vertically to form three-dimensional surfaces. They then used the finite element fitting procedure to minimise the RMS error between these surface elements and the original data points. Three-dimensional finite elements were created manually in the skeletal muscle and fat layers.

Odesanya *et al* [108] describe a method of constructing biological surface models from cross-sections and demonstrated their method by reconstructing the bone of a human hand. Their method was to first fit piecewise cubic B-splines through representative data points on the cross-sections, then create a mesh of quadrilateral patches over adjacent cross-sections using bicubic B-

spline surfaces, with second derivative continuity between the patches. They suggested that renderings of models indicated the method produced qualitatively acceptable results.

Image processing techniques can be used to extract boundary regions from cross-sectional scans. Although one of the main advantages in doing this is to automate the process of generating the torso geometry for a model, full automation is difficult to achieve. For example, Nadeem *et al* [109] presented an image processing technique and a boundary approximation algorithm for use in model construction. Although the boundaries for the heart, lungs and skeletal muscle were successfully extracted from a cross-sectional CT scan of a human, it was still necessary for human interpretation of the results and building of the final mesh.

### Tissue properties

Human tissue has resistive and reactive components of impedance and therefore, in general, tissue impedance is frequency dependent [110]. However, the characteristic frequency of implantable defibrillator waveforms is about  $100\text{Hz}$  and at this frequency the reactive components reduce to near zero [111, 112] and so the tissue may be considered to be purely resistive.

Many people have measured tissue resistance. The values found depend on the method and specimens used and consequently some of the reported values are spread over a wide range. Some reported values are listed in Table 3.2. Though the electrical resistance of muscle is anisotropic, some workers have measured just an average value of resistance for this tissue.

Swerdlow *et al* [116] looked at the effects of voltage and respiration on impedance in nonthoracotomy defibrillation pathways. They used shocks ranging from 65 to 745V and found impedance varied inversely with voltage (by up to 17% for transvenous-SQ, 8% for transvenous and 3% for epicardial) while respiration increased impedance only for transvenous-SQ. The voltage

Author	Resistivity ( $\Omega cm$ )						
	Heart	Muscle	Lung	Blood	Fat	Bone	Abdomen
Geddes and Baker [113]	400	300(l) 1600(t)	1500	150	2500		
Barber and Brown <sup>a</sup> [114]	410(l) 750(t)	530	1500 727-2364 <sup>b</sup>	150	2430	1660	
Rush [79]	400		2100	160	2100	$\infty$	
Pluta [115]		147(l) 250(t)	555	140	2000	$\infty$	285

<sup>a</sup>Mostly averaged results from many authors

<sup>b</sup>Range from expiration to inspiration

Table 3.2: *Reported values of conductivity ('l' is longitudinal, 't' is transverse).*

dependence of impedance was found to be greatest in the lungs.

Wharton *et al* [117] investigated the effect of shock strength on impedance in dogs using epicardial electrodes and shock strengths ranging from 1 to 1000V. They found that at low voltage (less than 25V) impedance was higher than at high voltage by up to a factor of four. Although some of this effect may have been from electrode polarisation, they suggested that the capacitance of the myocardium changed as a function of the delivered potential. Nevertheless, they concluded that impedance appears to be primarily resistive in the range of potentials necessary for defibrillation.

### Electrode-torso interface

The interface of the implanted electrode and the torso is usually modelled as a perfect interface with zero impedance. In reality, however, the impedance is not zero, though it is usually relatively small. Brigitte and Gisela [118] reported on energy loss due to polarisation for several electrode materials. Schimpf *et al* examined the impedance of an electrode-electrolyte interface for

transvenous electrodes [119], finding a polarisation impedance of between 2% and 5% of the overall impedance for typical transvenous pathways in humans and pigs.

Panescu *et al* [120] developed a nonlinear finite element model of the electrode-electrolyte-skin system. The model took into account the nonlinear behaviour of the skin with respect to the amplitude of the voltage.

### Model validation

Validation of torso models is an interesting topic that presents many practical difficulties. The following discussion illustrates examples of torso model validation procedures and results from a number of workers.

Barr and Spach [121] calculated epicardial potential distributions from measured body surface potentials for twelve dogs. Epicardial electrodes were implanted, with insulated wires extending subcutaneously to the lower abdomen, and the body surface potentials were allowed to return to normal (taking about 2 weeks). They then recorded the potential distributions on the 75 epicardial and 150 body surface electrodes, and calculated forward and inverse transfer coefficients between the epicardium and body surface, assuming the torso was a homogeneous volume conductor. They found that between the inverse computed and measured epicardial distributions, the relative error was high, often 0.7 or more, while the correlation coefficients were in the range 0.6-0.8. They concluded that the main physical features of epicardial potential distributions could be found from body surface measurements.

Messinger-Rapport and Rudy [122] placed a beating dog's heart in an epicardial cage and placed this in the correct anatomical position in a human-torso tank. They compared epicardial potentials measured on the epicardial cage to those calculated with an inverse model. Through the cardiac cycle, they found that the relative error was a minimum of 0.35 and a maximum of 1.0, with an average of 0.51. They also found that positions and shapes of features of the

potential map were recovered with good accuracy, with an error in position of 1cm being typical, while the amplitudes of these features were reduced slightly.

Derfus *et al* modelled a multi-electrode intracavity probe in the left ventricle and used the model to calculate the left ventricle intracavitary potentials from measured subendocardial potentials during pacing from a number of alternative sites [123]. Their model used the Boundary Element method to solve Laplace's equation. They compared the calculated potentials to potentials measured on the intracavity probe. They found that the accuracy of their prediction depended on the pacing site, the best being from apical pacing sites with a correlation coefficient of  $0.989 \pm 0.002$ , indicating excellent agreement for this type of study. However, from other pacing sites the correlation coefficient was lower (averaging  $0.873 \pm 0.092$ ) due to errors in measuring probe position and LV cavity geometry.

Shahidi *et al* [124], recorded epicardial and body surface potentials in a human to validate their model of the inverse problem of electrocardiology. The model was a FE torso model which they used to compute transfer matrices relating epicardial to body surface potentials for a patient, using different mesh resolutions and conductivity inhomogeneities. The epicardial potentials were measured using a 63 electrode heart sock during open chest surgery, while the body surface potentials were measured, also with 63 electrodes, prior to surgery. They found the measured epicardial potential distributions could not be adequately recovered from the body surface potential distributions using the inverse model, finding relative errors  $> 1$  and correlation coefficients  $< 0.4$ . However, they were able to locate the ventricular pre-excitation site. They suggested that the main experimental errors occurred due to the chest being open and the heart exposed to air when the epicardial potentials were recorded, and due to difficulties in determining the epicardial lead locations.

Kilpatrick and Walker [125] validated their inverse model in humans by predicting the coronary artery that had been involved in episodes of acute

myocardial infarction. They used a body surface mapping jacket with 51 electrodes and a resistor network model of the human torso. They found that the epicardial map correctly predicted the coronary artery involved in 40 out of 55 patients, and partially predicted the artery involved in 8 of the remaining patients. They concluded that the model did predict sensible epicardial maps from body surface potentials.

### **3.3 Clinical Results using Implantable Defibrillators**

Current practice using implantable defibrillators [126, 127, 128, 42] is tending towards simple endocardial configurations whenever possible and away from surgically invasive epicardial systems requiring thoracotomy. This has resulted in implantation being safer and cheaper in most instances and implantation is now sometimes as straightforward as with a pacemaker, though there are still a significant proportion of patients who, because of their high defibrillation thresholds, require one of the more complicated electrode systems and must undergo more extensive surgical procedures[129]. For all patients, use of systems with lower energy requirements is better physiologically and allows use of smaller defibrillator units.

Reported configurations and performance from sixteen investigations are summarised in Table 3.3. This table lists the object of each investigation, the electrodes, waveform and number of patients used, the anode-cathode resistance and voltage and the delivered energy.

Investigation	Defibrillation pathway	Waveform phase & %tilt	No. of patients	Resistance ( $\Omega$ )	Voltage (V)	p	Energy (J)	p	Ref.
01a	Waveform phase	RA $\rightarrow$ epi	27	37.2 $\pm$ 5.5	417 $\pm$ 66	< .0001	10.9 $\pm$ 3.3	< .0001	[130]
01b		RA $\rightarrow$ epi	27	38.0 $\pm$ 6.6	353 $\pm$ 67		7.6 $\pm$ 2.9		
02a	SQ patch position	RV $\rightarrow$ SVC+SQ <sub>pectoral</sub>	9				16.9 $\pm$ 5.4	< .04	[131]
02b		RV $\rightarrow$ SVC+SQ <sub>subscapular</sub>	9				11.2 $\pm$ 3.9		
03a	SQ patch position	RV $\rightarrow$ SVC/CS+SQ <sub>mid-axillary</sub>	30				17.4 $\pm$ 1.3	< .005	[129]
03b		RV $\rightarrow$ SVC/CS+SQ <sub>subscapular</sub>	30				14.2 $\pm$ 1.2		
03c	Simultaneous vs	RV $\rightarrow$ SVC/CS+SQ <sub>mid-axillary</sub>	30				20.2 $\pm$ 1.5	< .002	
03d	sequential shocks	RV $\rightarrow$ SVC/CS+SQ <sub>subscapular</sub>	30				18.5 $\pm$ 1.1		
04a	Additional CS	RV <sup>+</sup> $\rightarrow$ AC <sup>-</sup>	10		451 $\pm$ 104	.37	12.9 $\pm$ 5.7(s)	.39	[132]
04b	electrode	(RV+CS) <sup>+</sup> $\rightarrow$ AC <sup>-</sup>	10		408 $\pm$ 115		10.8 $\pm$ 5.4(s)		
05a	Waveform tilt	RV <sup>+</sup> $\rightarrow$ AC <sup>-</sup>	15		347 $\pm$ 125	.67	7.6 $\pm$ 5.0	.17	[133]
05b		RV <sup>+</sup> $\rightarrow$ AC <sup>-</sup>	15		359 $\pm$ 124		6.1 $\pm$ 4.0		
06a	Electrode polarity	proximal <sup>+</sup> $\rightarrow$ distal <sup>-</sup>	16	50 $\pm$ 6			16.4 $\pm$ 7.3	< .01	[28]
06b		proximal <sup>-</sup> $\rightarrow$ distal <sup>+</sup>	16	51 $\pm$ 5			11.7 $\pm$ 5.7		
07a	Trans vs Epi	epicardial	434				13.8	< .001	[134]
07b		transvenous	317				9.2		
08a	SQ patch	transvenous + SQ	21				9 $\pm$ 4	< .05	[135]
08b		transvenous	21				12 $\pm$ 4		
09a	Mono/biphasic	transvenous and/or SQ	42				9 $\pm$ 4	< .001	[135]
09b		transvenous and/or SQ	21				14 $\pm$ 5		
10	Trans. efficacy	transvenous	68				11.1 $\pm$ 4.6		[136]
11	Trans. efficacy	transvenous	25				14.0 $\pm$ 4.4		[137]
12	Epi. efficacy	epicardial (2 or 3 patches)	238				8.6 $\pm$ 5.3		[138]
13a	SQ patch	RV <sup>-</sup> $\rightarrow$ RA+SQ <sub>left-infra-clavicular</sub>	12-14		473 $\pm$ 97	< .01	14.3 $\pm$ 5.3	< .02	[139]
13b	position	RV <sup>-</sup> $\rightarrow$ RA+SQ <sub>infra-axillary</sub>	12-14		405 $\pm$ 80		10.2 $\pm$ 3.8		
13c		RV <sup>-</sup> $\rightarrow$ RA+SQ <sub>apical-cardiac</sub>	12-14		479 $\pm$ 84		14.4 $\pm$ 4.8		
14a	Simultaneous vs	RV $\rightarrow$ SVC/CS+SQ <sub>left-chest</sub>	14				6.7 $\pm$ 0.6	< .01	[140]
14b	sequential shocks	RV $\rightarrow$ SVC/CS+SQ <sub>left-chest</sub>	14				13.2 $\pm$ 3.8		
15	Unipolar	RV <sup>+</sup> $\rightarrow$ AC <sup>-</sup>	25				9.3 $\pm$ 4.6		[141]
16a	Sequential	RV $\rightarrow$ SVC+CS	9		504 $\pm$ 73	.001	16.0 $\pm$ 4.4	.019	[142]
16b	Active can	RV $\rightarrow$ AC	9		348 $\pm$ 63	.027	9.6 $\pm$ 4.2	.039	
16c	SVC	RV $\rightarrow$ SVC	9		399 $\pm$ 60		12.7 $\pm$ 43.7		
"mean"							12.2 $\pm$ 3.8		

Table 3.3: Reported performance of electrode configurations in humans. RA = right atrium, RV = right ventricle, SVC = superior vena cava, AC = active can pulse generator, SQ = subcutaneous patch (with subscript indicating location), CS = coronary sinus and (s) = stored energy. Energy data from this data is plotted in Figure 3.1.  $p$  values are between value on row and values below and/or above.  $p$ =NS for resistance.

First, consider each individual investigation. Gold *et al* (Investigation 01) reported a study where the implanted electrodes were a spring coil in the mid right atrium and a large extra-pericardial patch over the left ventricle [130]. They found biphasic waveforms lowered energy by 30% and voltage by 15% compared to monophasic. Resistance was unchanged and energy changed by approximately the square of the voltage ratio, which agrees with the relationship ( $E = V^2/R$ ) expected for resistive materials.

Schwartzman *et al* (Investigation 02) found DFT energy was 34% lower for a subscapular compared to a pectoral SQ patch when used with a RV and SVC electrode, though there was no significant difference in voltage or resistance [131]. This result is surprising as either resistance, voltage of both should have changed with energy. The best explanation for this is that the uncertainty in the resistance and voltage values meant changes could not be resolved.

Swartz *et al* (Investigation 03) also investigated SQ patch position, finding that the DFT energy was 18% less in the subscapular than the mid-axillary position, when used with a RV and either a SVC or CS electrode [129]. They also found approximately 22% higher DFT energy with sequential than simultaneous shocks.

Bardy *et al* (Investigation 04) compared an RV (anode) and AC electrode configuration to one with an additional anode in the coronary sinus, and suggested they had found a small decrease in DFT energy and voltage [132]. However, their results suffered from low resolution, indicated by their high  $p$  values and their results were not conclusive.

In Investigation 05, the results of Bardy *et al* again suffered from a high degree of uncertainty. They were unable to distinguish between the DFT voltage and energy for 65% and 50% tilt waveforms, applied through an RV electrode to pectoral active can configuration to 15 patients.

Strickberger *et al* (Investigation 06) looked at the effect of electrode polar-

ity using a transvenous two-electrode system. They found that DFT energy was raised 40% if the proximal (RV) electrode was the anode rather than the cathode, while the resistance was unchanged.

Saksena *et al* (Investigation 07) compared the DFT in two large groups of patients implanted with either epicardial or endocardial electrodes and found that mean DFT energy was 33% less in the endocardial group. They found, though, that sudden death incidence was comparable for both groups, but perioperative mortality (5.5% epicardial, 0.3% endocardial) was reduced with endocardial leads.

Block *et al* (Investigations 08 and 09) looked at defibrillation using a two-electrode transvenous system with and without a SQ patch and with mono- and bi-phasic waveforms. They found that DFT energy was reduced 25% using a SQ patch and 35% using a biphasic waveform, and that a single transvenous lead was effective in 90% of patients while transvenous-SQ was effective in 100% of patients.

Bardy *et al*, Venditti *et al*, Leitch *et al* and Bardy *et al* (Investigations 10, 11, 12 and 15) found DFT energy for transvenous, epicardial and RV-AC configurations. Their individual results are difficult to compare because they were not controlled experiments within a single investigation. It is interesting though that the transvenous results (11.1 and 14.0J) were higher than the epicardial result (8.6J), which opposes the finding of Saksena *et al* in Investigation 07.

Saksena *et al* (Investigation 13) compared SQ patch position for a three-electrode RV to RA and SQ system. Compared to left infraclavicular and apical-cardiac positions, an infra-axillary position was found to reduce DFT energy and voltage by 29% and 15%, respectively.

Hsia *et al* (Investigation 14) compared simultaneous and sequential pathways using a RV to (SVC or CS) and SQ patch configuration. They found that the DFT energy was reduced by 50% for sequential compared to simultaneous

shocks. This is at odds with Investigation 03 where DFT energy for sequential shocks increased by 22%.

Zardini *et al* (Investigation 16) compared a three-electrode transvenous system (RV to SVC and CS) with sequential pulses and two biphasic two-electrode systems (RV to SVC and RV to AC) with biphasic pulses. The active can configuration performed best, while the three-electrode system performed the worst, requiring 67% greater energy and 45% greater voltage. The three-electrode sequential pulsing pathways were similar and may not have been of great benefit compared to biphasic pulses, while the relatively large surface area of the active can configuration could account for its superiority over the SVC electrode configuration.

Using data from the table, it is possible to compare configurations, but only within an individual investigation. Although tempting, it is difficult to compare energy and voltage data between studies because of differences in experimental methods and subjects. For example, in an (unrelated) experimental study—using a RV transvenous coil and LV epicardial patch ( $14\text{cm}^2$ ) in pigs—the defibrillation energy for 50% and 90% probability of success was reported as  $9.0 \pm 0.6$  and  $16.2 \pm 2.1\text{J}$ , respectively, indicating the large variation in results corresponding to a change in this variable alone [143]. Also, electrodes with the same description (e.g. RV endocardial) may be quite different in size, shape and location. Despite these difficulties, there are interesting observations that can be made.

In discussing the results in Table 3.3, first consider the column of energy data (which is presented graphically in Figure 3.1 as bars of mean  $\pm$  standard deviation) and the column of  $p$  values. The standard deviation of most of the results was relatively large at approximately  $5\text{J}$ , compared to the means at approximately  $13\text{J}$ , but in general, in each study the numbers of patients and statistical techniques used ensured the mean values of energy for different treatments were clearly differentiated, as evidenced by the low ( $< 0.01$ )  $p$  values

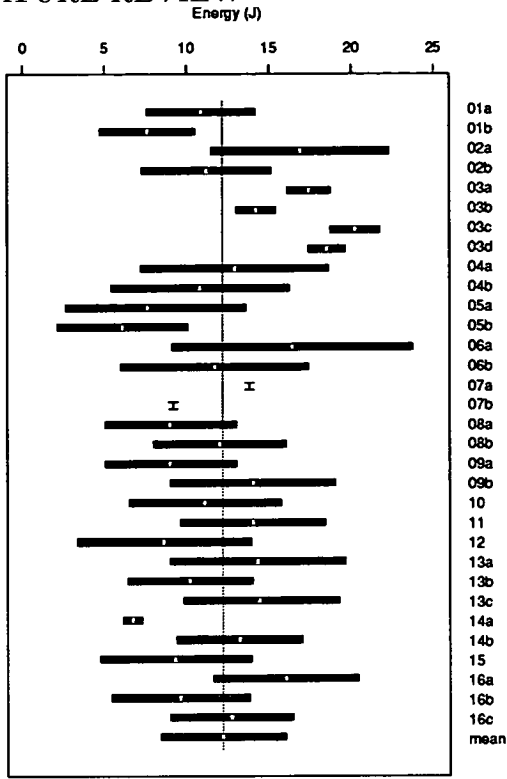


Figure 3.1: Minimum energy (mean  $\pm$  standard deviation) for defibrillation in humans for various electrode configurations (data from Table 3.3). Dotted line indicates mean energy.

in most of the studies. Exceptions were studies 04, with  $p$  values for voltage and energy of 0.37 and 0.39, respectively, even though there were relatively large differences between mean values, and 05 ( $p$ 's of 0.67 and 0.17), though in this case differences between means was relatively small.

Two studies, 03 and 14a, had standard deviations that were relatively low ( $\leq 1.5J$ ). The reasons for low standard deviation in these studies is potentially of great interest. For the electrode configurations and waveforms used, thresholds were very similar between patients and were inherently predictable. The reasons for this behaviour may be connected to the mechanics of defibrillation. It is interesting that the configurations with small standard deviations had two transvenous electrodes (RV and SVC/CS) and a subcutaneous patch (though the other configurations of this type (02, 04b, 08b, 09, 13) did not have small standard deviations).

These published clinical results show a quite bewildering array of apparently unrelated results where often one study seems to contradict another, but

when taken individually the results mostly seem logical.

### 3.4 Discussion

This chapter has reviewed relevant modelling literature and clinical studies of defibrillator performance. Recently, a number of finite element models have been presented, mainly in conference proceedings rather than in refereed journals. Although, in general, they are satisfactory models, they all are subject to disadvantages of the finite element method. The disadvantages include: the necessity to generate a mesh throughout the torso using volume elements; the necessity to use a sufficiently fine mesh in critical regions, such as near electrodes or in regions where the conductivity changes rapidly, to ensure convergence of iterative methods and accurate solutions; the necessity to generate new meshes for different electrode configuration or torso geometry; the necessity to use iterative methods to solve large problems which can lead to difficulties in ensuring convergence and accuracy of the solution. Some of these disadvantages may be a significant handicap in certain circumstances.

The boundary element model presented in this thesis avoids these disadvantages. The surface meshes are relatively easy to construct and may be easily refined in critical areas. The solution is obtained using a direct solver, which avoids problems with solution convergence. The solver developed enables different electrode configurations to be solved without the need to repeat the majority of the calculations, leading to relatively quick optimisation of electrode configurations.

The main advantage of the finite element models is the ability to include detailed anisotropy. This would be a significant advantage if anisotropy was widely distributed throughout the torso. However, torso anisotropy is limited to a small number of localised regions and, if desired, can be included in a boundary element model by modelling these regions using finite elements or a

number of boundary element subregions each having anisotropy in a constant direction.

The results from the clinical studies of defibrillator performance provide useful data with which to compare results obtained from models for similar electrode configurations. This comparison will indicate how closely model results compare to clinical results. With knowledge of these results it is possible to realise how well the boundary element model predicts defibrillator performance. The clinical results also show the relatively large range in performance of similar configurations in different studies, the difficulty of conducting well controlled experiments and comparisons between configurations, and sometimes the contradiction of results by different studies. This all adds to the arguments for modelling defibrillator configurations. Modelling allows the variables to be controlled and for clear distinctions to be made between the performance of different electrode configurations.

# Chapter 4

## Numerical Methods

### 4.1 Introduction

The numerical methods that may be used to solve the modelling equations for the electric field in the torso include the boundary element, finite element and finite difference methods. Models based on both the boundary and finite element methods were implemented. The boundary element solution method was implemented in original software after discretisation of the governing mathematical equations. The finite element method was implemented using a commercial package.

In the models, human tissue was considered to be a volume conductor with electrical conductivity that was purely resistive. This followed from the assumption that defibrillation waveforms do not induce significant capacitive or inductive effects in human tissue, as discussed in Section 3.2 (page 30).

The mathematical basis of both models was that the electric field in the torso was governed by Laplace's equation,

$$\nabla \cdot (\mathbf{k} \nabla u) = 0, \quad (4.1)$$

where  $u$  is the potential and  $\mathbf{k}$  the conductivity tensor. Boundary conditions

were as follows: on the surface of the torso,

$$\nabla u \cdot \mathbf{n} = 0, \quad (4.2)$$

where  $\mathbf{n}$  is the vector normal to the surface; on the surface of electrodes,

$$u = e(x, y, z), \quad (4.3)$$

where  $e$  describes the electrode positions and potentials.

## 4.2 Boundary Element Method

In the boundary element method, elements divide the torso into regions of constant conductivity. To apply this method, elements of the torso were grouped into regions where the electrical properties were approximated as isotropic and homogeneous. Laplace's equation was applied within each region and interface conditions were enforced between regions.

Within a region, the conductivity was constant and therefore equation (4.1) reduces to

$$\nabla^2 u = 0. \quad (4.4)$$

If we let

$$q = \frac{\partial u}{\partial \mathbf{n}}, \quad (4.5)$$

be the potential gradient normal to the region boundary, where  $\mathbf{n}$  is the geometric normal to the boundary, and  $u^*$  be the fundamental solution of Laplace's equation, then the fundamental equation of the boundary element method can be written (based on a weighted residuals formulation) as [144]

$$u^i + \int_{\Gamma} u q^* d\Gamma = \int_{\Gamma} q u^* d\Gamma, \quad (4.6)$$

where  $\Gamma$  is the boundary and the point  $i$  is within the region. For three-dimensional problems, the fundamental solution is

$$u^* = \frac{1}{4\pi r} \quad (4.7)$$

and

$$q^* = \frac{\partial u^*}{\partial \mathbf{n}} = \frac{\partial u^*}{\partial r} \frac{\partial r}{\partial \mathbf{n}} = -\frac{1}{4\pi r^2} \frac{\partial r}{\partial \mathbf{n}} \quad (4.8)$$

where  $r$  is the distance from point  $i$  to the boundary. Equation (4.6) is valid for point  $i$  within the region, but for point  $i$  on the boundary of the region we get

$$c_i u^i + \int_{\Gamma} u q^* d\Gamma = \int_{\Gamma} q u^* d\Gamma, \quad (4.9)$$

where  $c_i$  is a coefficient to be determined.

The boundary element method involves numerically solving equation (4.9) to find the potential and gradient over the region boundary. The boundary of the region,  $\Gamma$ , is therefore divided into  $N$  discrete elements,  $\Gamma_j$ , resulting in the following equation:

$$c_i u^i + \sum_{j=1}^N \int_{\Gamma_j} u_j q^* d\Gamma = \sum_{j=1}^N \int_{\Gamma_j} q_j u^* d\Gamma. \quad (4.10)$$

The boundary discretisation was done using quadrilateral elements. It would have also been possible to use triangular elements or elements of more complex shape (curved, for example). The variation of potential and normal gradient was assumed constant over each element and equal to the value at the mid-point. Again, other schemes, with linear or quadratic variation, for example, could have been used. Constant quadrilateral elements were chosen primarily for ease of implementation, both computationally and in mesh construction. The constant variation of potential did present challenges in accurately calculating potential gradient on elements in postprocessing calcu-

lations.

For constant elements,  $u_j$  and  $q_j$  may be taken out of the integrals and  $c_i = 1/2$ . Therefore, equation (4.10) becomes

$$\frac{1}{2}u^i + \sum_{j=1}^N u_j \int_{\Gamma_j} q^* d\Gamma = \sum_{j=1}^N q_j \int_{\Gamma_j} u^* d\Gamma. \quad (4.11)$$

The remaining integrals apply only over individual elements and may be calculated numerically using two dimensional Gaussian quadrature rules. The element integration implementation is detailed in Appendix B and is similar that implemented by Kilpatrick and Johnston [88]. The result of integration over the elements can be written as  $\hat{H}$  and  $G$  terms where

$$\hat{H}_{ij} = \int_{\Gamma_j} q^* d\Gamma, \quad (4.12)$$

and

$$G_{ij} = \int_{\Gamma_j} u^* d\Gamma, \quad (4.13)$$

Equation 4.11 now becomes

$$\frac{1}{2}u^i + \sum_{j=1}^N \hat{H}_{ij} u_j = \sum_{j=1}^N G_{ij} q_j \quad (4.14)$$

or simply

$$\sum_{j=1}^N H_{ij} u_j = \sum_{j=1}^N G_{ij} q_j \quad (4.15)$$

where

$$\begin{aligned} H_{ij} &= \hat{H}_{ij} & \text{for } i \neq j \\ H_{ij} &= \hat{H}_{ij} + \frac{1}{2} & \text{for } i = j \end{aligned} \quad (4.16)$$

This results in a set of equations that can be written in matrix form as

$$\mathbf{H}\mathbf{u} = \mathbf{G}\mathbf{q}, \quad (4.17)$$

where  $\mathbf{H}$  and  $\mathbf{G}$  are both square ( $N \times N$ ) matrices and  $\mathbf{u}$  and  $\mathbf{q}$  are vectors (of length  $N$ ) of potential and potential gradient on each boundary element.

Matrix equations of type (4.17) were derived for each region in the model. These equations were combined using interface conditions between connected regions. This resulted in a set of equations describing the electric field through the whole torso.

The interface boundary conditions between connected regions were compatibility of voltage and continuity of current. That is, if  $k_i$ ,  $u_i$  and  $q_i$  were, respectively, the conductivity of region  $i$  and the potential and normal gradient on the boundary of region  $i$ , then on a common boundary between regions 1 and 2,

$$u_1 = u_2 \quad (4.18)$$

and

$$k_1 q_1 = -k_2 q_2. \quad (4.19)$$

Boundary conditions arose due to no current flow across the outer region boundary or across electrode surfaces (Neumann boundary condition), and due to applied potential on electrodes (Dirichlet boundary condition).

Applying the boundary conditions resulted in matrix equations that fully described the problem. The assembled matrix equations, though, had a mixture of known and unknown values of  $u$  and  $q$  on each side. The equations were therefore rearranged to form a global matrix equation:

$$\mathbf{A}\mathbf{x} = \mathbf{b}. \quad (4.20)$$

This consists of: a square matrix,  $\mathbf{A}$ , of known values that were dependent on the geometry; a vector,  $\mathbf{x}$ , of unknowns; and a vector,  $\mathbf{b}$ , of known values that were dependent on the geometry and the boundary conditions. A detailed description of the assembly of the matrix equations is given in Appendix A.

Equation (4.20) was solved to yield the unknown values of  $u_j$  and  $q_j$  contained in  $\mathbf{x}$ . The solution method employed was Gaussian elimination <sup>1</sup>.

After solution of equation (4.20), the potential  $u$  and normal gradient  $q$  were known on each boundary element. Values of  $u$  and  $q$  elsewhere in the torso, such as at an internal point  $i$ , were found using the known boundary  $u$ 's and  $q$ 's applied to the integral equation

$$u^i = \int_{\Gamma} q u^* d\Gamma - \int_{\Gamma} u q^* d\Gamma \quad (4.21)$$

Equation (4.21) is simply a rearrangement of equation (4.6). At the point  $i$ , the equation describing the potential gradient in a direction  $x$  was found by differentiating equation (4.21) to get

$$q_x^i = \left( \frac{\partial u}{\partial x} \right)^i = \int_{\Gamma} q \frac{\partial u^*}{\partial x} d\Gamma - \int_{\Gamma} u \frac{\partial q^*}{\partial x} d\Gamma \quad (4.22)$$

with similar expressions for the  $y$  and  $z$  directions. Equations (4.21) and (4.22) were discretised in a similar way to equation (4.10) and the values of  $u^i$ ,  $q_x^i$ ,  $q_y^i$  and  $q_z^i$  were found by direct substitution of the known boundary potentials and normal gradients.

The gradient on a boundary was calculated by adding the vectors describing the normal and tangential gradients. The normal gradient was known from the initial boundary element solution. The two tangential gradients were calculated using an approximate method where the known element potentials were linearly interpolated onto the element nodes to get nodal potentials, which were used with the element geometry to calculate the gradient.

---

<sup>1</sup>The implementation of Gaussian elimination used a novel method that reduced the numerical processing requirements when solving multiple problems. Also, by using efficient out-of-core techniques, any size problem could be solved, subject only to limitations in disk space and processing time. (Refer to Section 5.3)

### 4.3 Finite Element Method

To apply the finite element method, elements of the torso were again grouped into regions where the electrical properties were approximated as isotropic and homogeneous. Laplace's equation (equation (4.1)) and the boundary conditions from equations (4.2) and (4.3) were then applied to the complete torso.

The electrical conductivity varied within the torso so the conductivity term was retained in Laplace's equation. The governing equation was therefore

$$\nabla \cdot (\mathbf{k} \nabla u) = 0, \quad (4.23)$$

where  $\mathbf{k}$  was the conductivity tensor and  $u$  the potential.

Consider now Green's theorem:

$$\int_V \phi \nabla \cdot (\mathbf{k} \nabla \psi) dV = - \int_V \mathbf{k} \nabla \phi \cdot \nabla \psi dV + \int_S \mathbf{k} \phi \frac{\partial \psi}{\partial n} dS \quad (4.24)$$

where  $V$  is a volume,  $S$  is the bounding surface and  $n$  is the geometric normal to the surface. Green's theorem holds throughout  $V$  for functions  $\phi$  and  $\psi$ . If  $\psi = u$ , then equation (4.23) can be substituted into equation (4.24). The left hand side vanishes, resulting in the relation:

$$\int_V \mathbf{k} \nabla \phi \cdot \nabla u dV = \int_S \phi \mathbf{k} \frac{\partial u}{\partial n} dS \quad (4.25)$$

In FIDAP, this equation is discretised forming a set of matrix equations. The type of elements used were 8 node linear bricks. For these elements, the matrix components were evaluated using three dimensional Gaussian quadrature. The resulting set of equations were solved using FIDAP's conjugate gradient solver yielding values for potential at each node.

Details of the discretisation of equation (4.25) have not been reproduced here since they are described in detail in the FIDAP manuals. Also, many

finite element method texts are available that describe the method (for example, [145]).

# Chapter 5

## Implementation of Numerical Methods

### 5.1 Introduction

This chapter discusses implementation of the numerical methods of Chapter 4. The implementation involved discretisation of the torso and embodiment of the discretised equations into computer code. A number of steps were therefore involved in the implementation: the torso geometry was constructed; boundary conditions and electrodes were specified; the governing matrix equations were built; the equations were solved to find the unknowns; and postprocessing was done to calculate potentials and gradients inside regions and gradients on boundaries.

It should be noted that the implementation was performed for Silicon Graphics Iris Indigo XZ 4000<sup>1</sup> or Sun 4.330<sup>2</sup> computers with 96 megabytes of random access memory. Software was developed using the C programming language. Solution times given in the text are for programs running on the Indigo, which was the faster of the two computing platforms.

---

<sup>1</sup>Silicon Graphics, Inc., Mountain View, California, U.S.A.

<sup>2</sup>Sun Microsystems Computer Corporation, Inc., Fremont, California, U.S.A.

## 5.2 Torso Construction

One human and one sheep torso were constructed for use with the boundary element method and one human torso was constructed for use with the finite element method. This allowed modelling of realistic electrodes, investigation of new electrode configurations, comparison of model and experimental results and comparison of model results with published results from numerical and clinical studies. It was desirable for the two human torsos to be as similar as possible because boundary element results were to be compared to finite element results as part of the validation of the boundary element model. Consequently, the human torso was first constructed from boundary elements, then this was used as the basis for the finite element torso.

### Boundary element torsos

The available data for the construction of the human boundary element torso included a series of 25 CT scans at 1cm spacing of a normal male and a series of 11 MRI scans at 1cm spacing of a normal female. Torso geometry was obtained from the CT scans while heart geometry was obtained from the MRI scans. Although this was not the ideal of having all scans from the same person, the torso and heart were compatible and only slight modification to the shape of the lungs was required when the heart was placed inside the torso. The outline of each major structure in the torso was digitised from the scans using a Hipad<sup>3</sup> digitising pad. The digitised outlines were then used to build three dimensional surface meshes representing the structures. The structures digitised were the heart, venous and arterial blood cavities, major vessels, lungs, spine, sternum and the third, fourth, fifth and sixth ribs on the left side (Figure 5.1). All other torso components were grouped together as torso tissue. Each structure

---

<sup>3</sup>Hipad<sup>T.M.</sup> Digitising Pad, Bausch and Lomb, Austin, Texas., U.S.A.

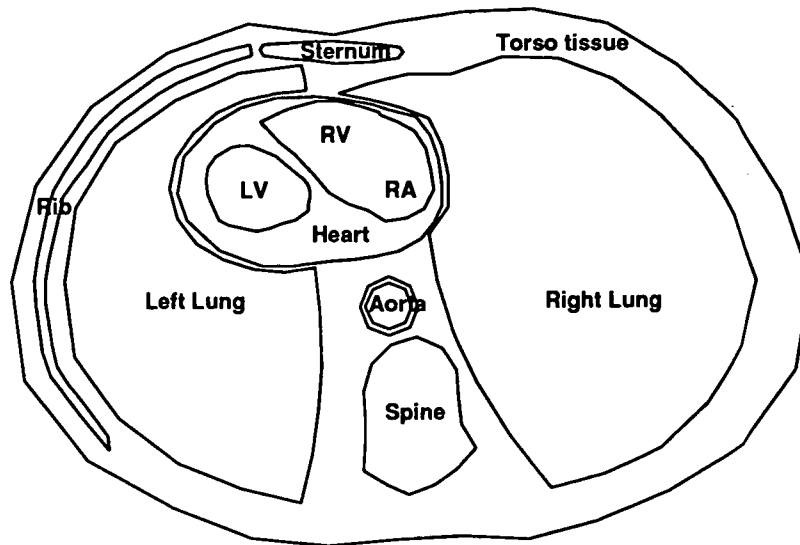


Figure 5.1: *Slice through the torso showing regions in the model*

represented one region in the model.

The data for the construction of the sheep boundary element torso was obtained from CT scans of a sheep taken specifically for this purpose. The sheep was a normal Australian cross-bred ewe. The sheep's torso was CT scanned at 1cm intervals resulting in thirty three images from neck to abdomen. The boundaries of the torso, spine, sternum, lungs, epicardium and major vessels were digitised from the scans, while the endocardial cavities were digitised from 1cm sections taken through the explanted heart. The torso structures were then built from the digitised boundaries using quadrilateral elements. The sheep model was therefore similar to the human torso model although the aorta and inferior vena cava were not fully defined in the sheep model.

The structures in the human and sheep boundary element torsos were built using the pre- and post-processing package Patran<sup>4</sup> and routines developed to partly automate the building. The building procedure involved creating nodes around the digitised boundaries at appropriate points. The nodes were then connected on and between slices to create quadrilateral elements defining the

<sup>4</sup>Patran was from PDA Engineering, Costa Mesa, California

surface of each region.

A number of strategies were used in the building process. One strategy involved spacing a constant number of nodes evenly around each digitised boundary. Nodes on adjacent boundaries were then connected to form the mesh. The use of transition elements were sometimes combined with this strategy. Transition elements were quadrilateral elements that were constructed such that adjacent boundaries could contain different numbers of nodes.

Another strategy was used for regions with boundaries that were reasonably regular in shape. After digitising the scans, an open-ended cylindrical surface mesh was constructed that had a layer of nodes corresponding to each digitised slice. The cylindrical mesh was placed over the digitised points and then shrunk onto them. This mesh was then smoothed by maximising the corner angles of the elements. The mesh was then modified manually, if necessary. In both of these steps, element node positions were moved to alternative digitised points to preserve the integrity of the region shape, rather than allow unrestricted movement of the nodes. The open ends of the mesh were then enclosed manually. Following this, a second mesh could be shrunk over the first, if desired. The second mesh was shrunk until its element nodes were about to enter the region defined by the first mesh. This allowed a high density mesh to be created with nodes that were not constrained to lie on the same cross-sections as the original digitised points. The second mesh could also be smoothed, if necessary.

Patran was used to modify or to add details to each mesh, or sometimes to construct portions of the surface that were difficult to create by other means. Patran was especially useful in creating transition regions, where the region shape changed rapidly or where two parts of a region were connected after being meshed separately. Another use of Patran was the construction of geometry using splines or parametric cubic curves fitted through the digitised points, then creation of the mesh from this geometry.

Heart	Lung	Blood	Fat	Bone	Thoracic tissue
556	2000	150	2500	$\infty$	435

Table 5.1: *Values of resistivity ( $\Omega cm$ ) used in the model.*

The final form of the surface meshes representing the human and sheep torso structures are shown in Figures 5.2 (and Plates 1 and 2) and 5.3. In total, approximately 6000 quadrilateral elements were used in the human torso and 7000 in the sheep. The conductivity of each region was set to the values in table (5.1). These values were taken as representative from the literature, as discussed in section 3.2.

A variety of methods were used to represent electrodes (Figure 5.4). Electrodes in the venous blood were represented as additional regions within the blood and were created using Patran. The boundary condition applied was a constant potential over their surface. Epicardial electrodes were represented by an additional region over the epicardium. They were created by defining elements on the epicardium that were to be covered and then running a purpose-written computer program that automatically created the electrodes. If necessary, the lung surfaces were displaced to make room for the epicardial patches. The boundary conditions applied were constant potential on the covered epicardial elements and zero normal gradient on the sides and back of each patch. Subcutaneous patches were represented simply by boundary conditions on the torso surface. The boundary condition applied was a constant potential on selected elements.

### Finite element torso

As previously mentioned, it was desirable for the finite element torso to be as similar as possible to the boundary element torso. Consequently, the finite element torso was constructed directly from the boundary element torso.

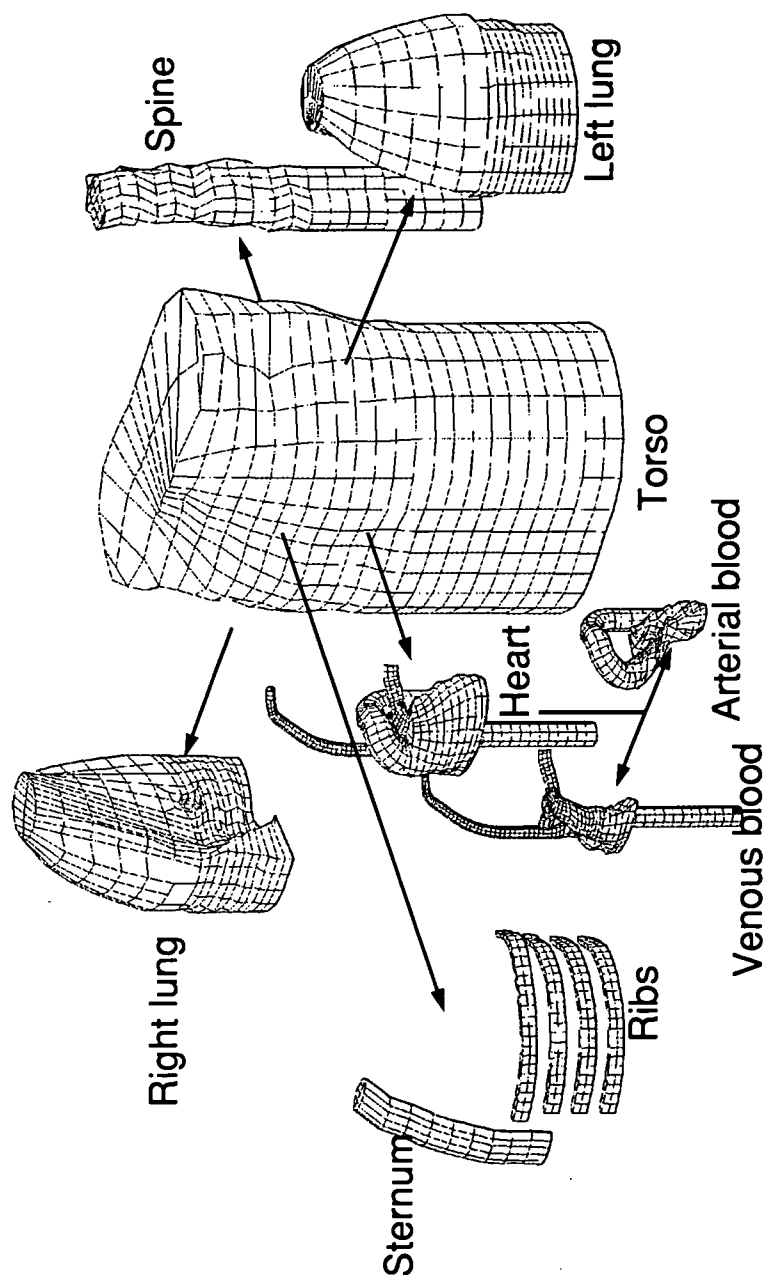


Figure 5.2: *Components of the human torso discretised into boundary elements (also see Plates 1 and 2)*

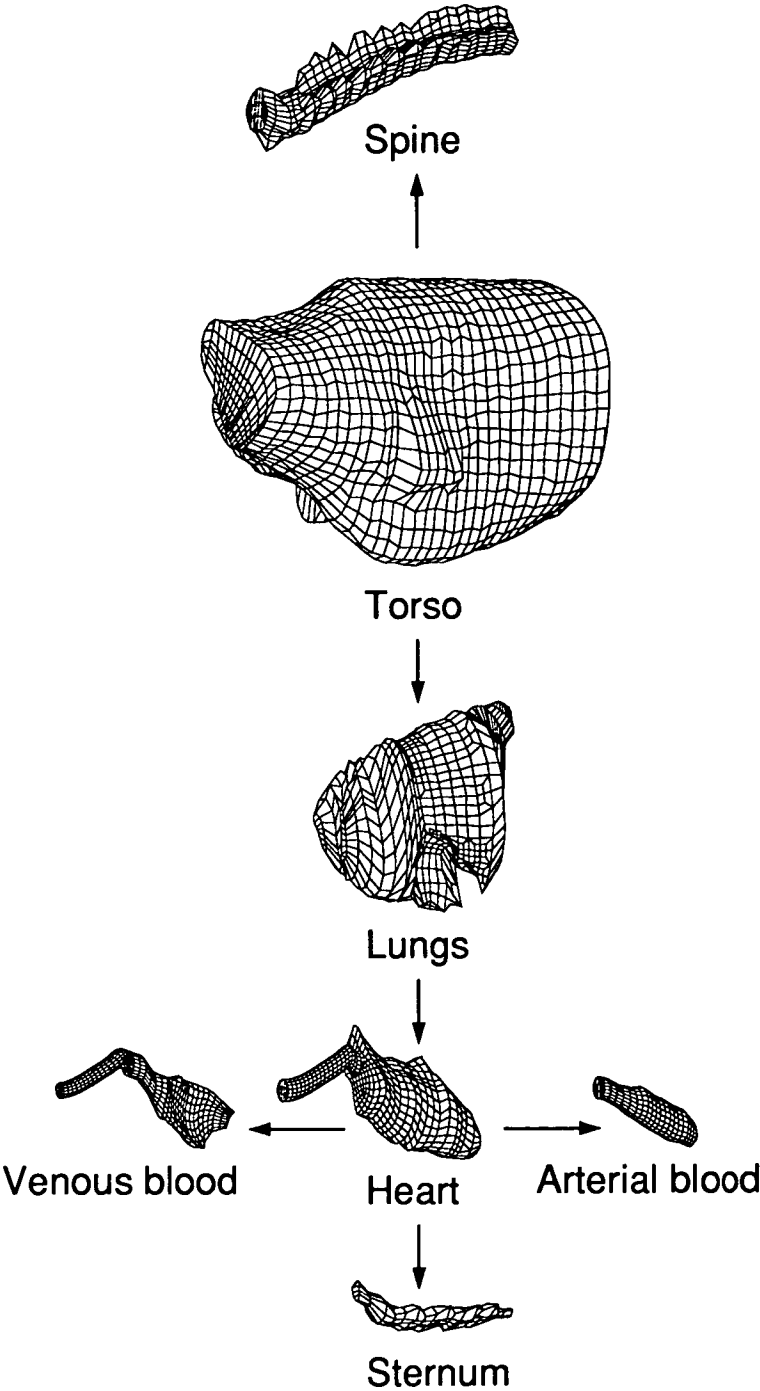


Figure 5.3: *Components of the sheep torso discretised into boundary elements*

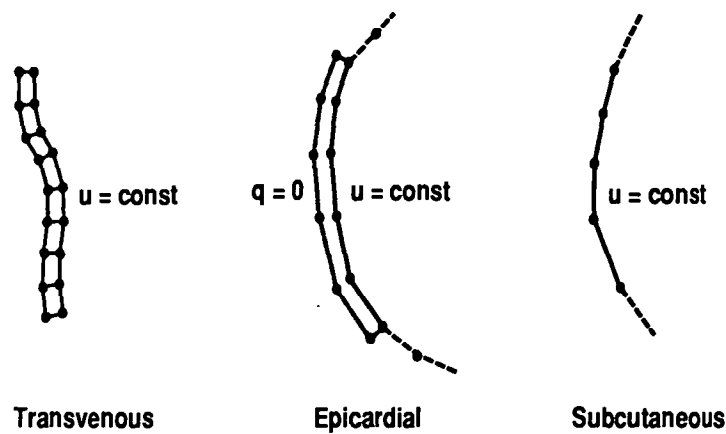


Figure 5.4: *Types of electrodes implemented in the boundary element model*

The boundary element torso was used to establish the location of the torso structures.

The first stage in construction was to specify the locations of the electrodes. An extremely coarse finite element mesh was then constructed that encompassed the whole torso using 8 node brick elements (Figure 5.5(a)). The construction was such that there would eventually be a high density of nodes around the specified electrodes. The next stage involved splitting each brick element into 8 smaller bricks, Figure 5.5(b). The sub-division process was then repeated Figure 5.5(c). After six subdivisions the desired node density was achieved. The mesh density was such that each major feature in the boundary element mesh was adequately resolved using finite elements. The mesh was related to the boundary element torso by comparing the location of the centroid of each brick to the positions of the boundary element structures. Those bricks outside the torso were removed. Those inside were assigned the conductivity of the corresponding structure. A cross-section through the final finite element mesh with the boundary element mesh superimposed is shown in Figure 5.5(d). A total of 159952 nodes and 153082 elements were used.

Boundary conditions were applied by finding the finite element nodes that corresponded to the electrodes in the boundary element model and setting the potential on those nodes. The boundary condition on the torso boundary was

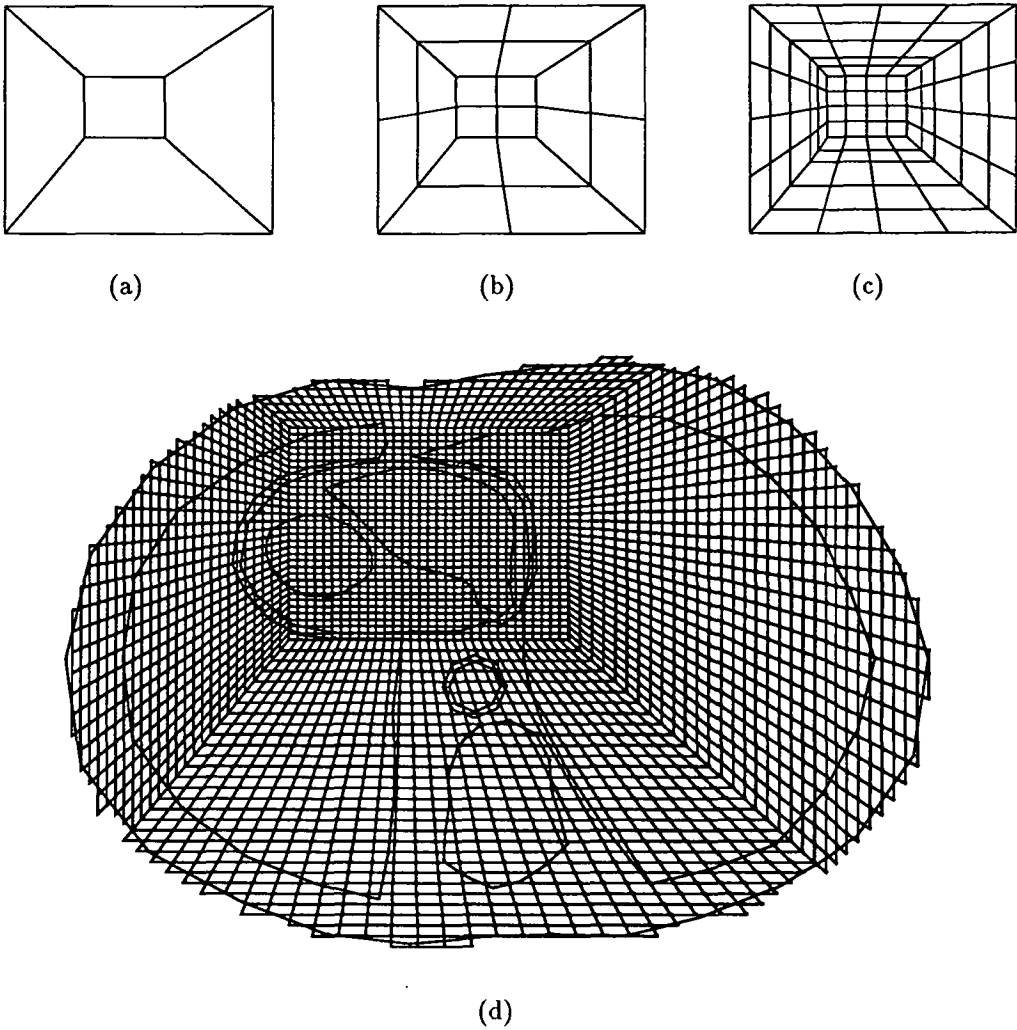


Figure 5.5: *Cross-section through the (a) first, (b) second, (c) third and (d) sixth (and final) brick meshes during construction of the finite element torso. On the final brick mesh, bricks outside the torso have been removed and the boundary element mesh superimposed*

zero normal flux. An exploded view of the finite element torso is shown in Figure 5.6.

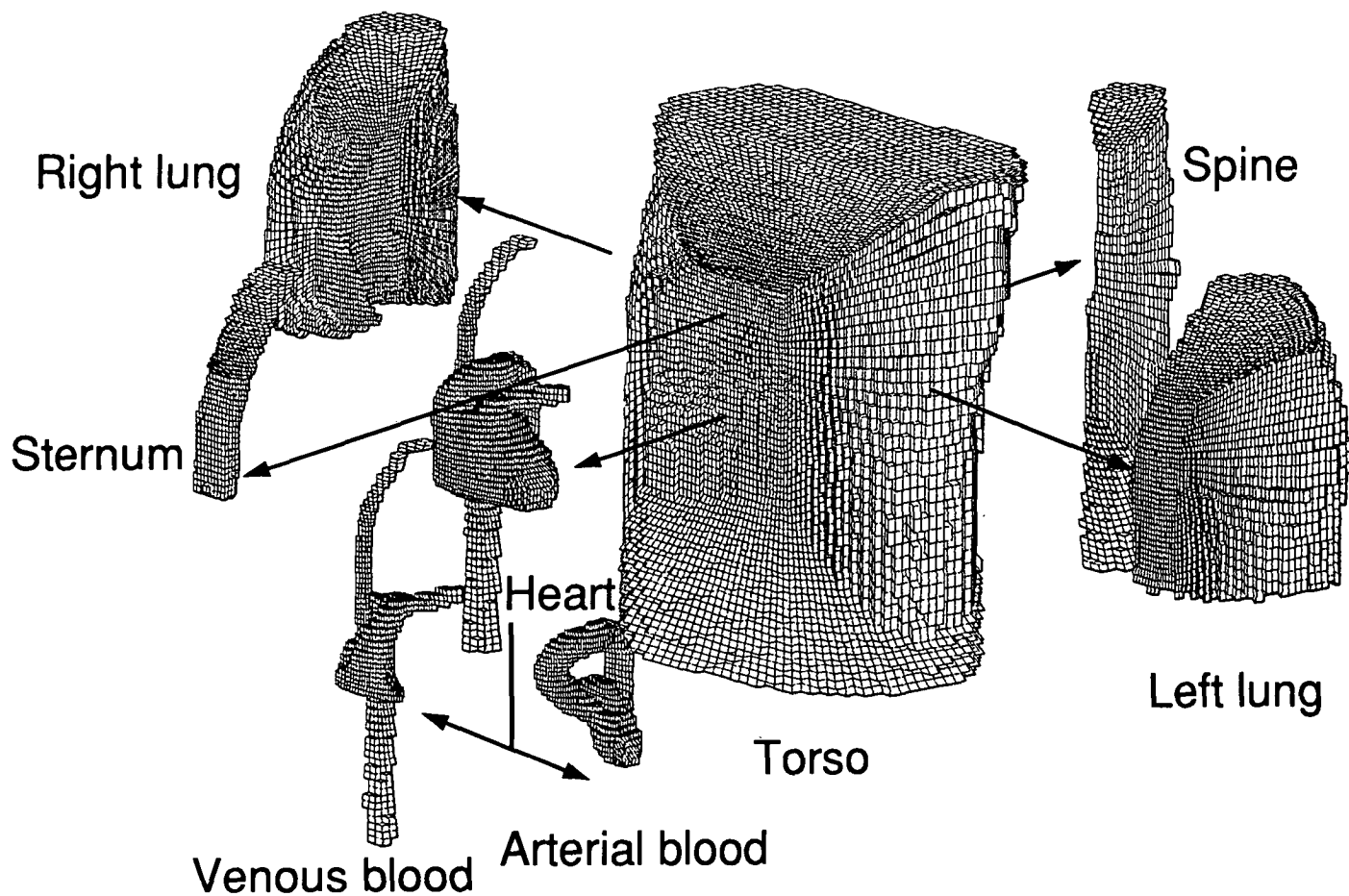


Figure 5.6: *Components of the finite element torso*

### 5.3 Boundary Element Method Implementation

#### Building equation matrices

The boundary element implementation involved building matrix  $\mathbf{A}$  and vector  $\mathbf{b}$  from equation (4.20). The first step in building  $\mathbf{A}$  and  $\mathbf{b}$  was to build sub-matrices by applying equation (4.17) to each region of the discretised torso. The sub-matrices were combined using equations (4.18) and (4.19) then rearranged with the unknown potentials and gradients were on the left hand side and the known values were on the right hand side. The matrix on the left was  $\mathbf{A}$ , while the matrix on the right was multiplied by the known values to form  $\mathbf{b}$ .

The block structure of  $\mathbf{A}$  is shown in Figure 5.7. The size and structure of  $\mathbf{A}$  determined the solution techniques employed. The dimension of  $\mathbf{A}$  was typically around  $10000 \times 10000$ . Also,  $\mathbf{A}$  contained blocks of values for each region in the torso. Blocks representing the torso tissue, heart and venous blood regions were relatively large because of the number and complexity of surfaces in those regions. The torso tissue and heart blocks were particularly large. The venous blood only enclosed electrodes, so the blocks for this region were not particularly large because of the relatively small number of elements associated with the electrodes.

The size of the large individual blocks in  $\mathbf{A}$  could be reduced by adding additional surfaces inside the torso. The surfaces would be constructed specifically to reduce the number and size of subregions within the torso tissue and heart. These would result in  $\mathbf{A}$  becoming more narrowly banded which could potentially reduce the computation time.

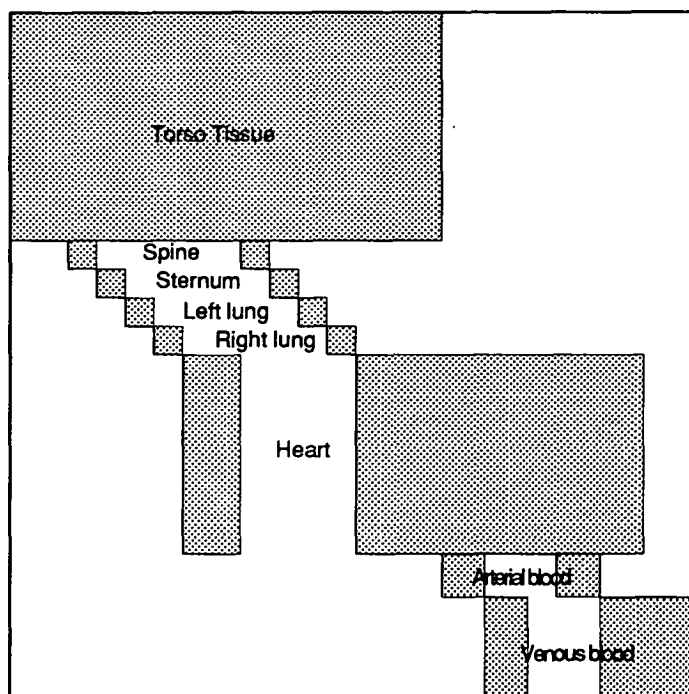


Figure 5.7: *The block structure of matrix  $A$  in equation (4.20)*

### Solving the matrix equations

The matrix equations derived from equation (4.20) were solved using Gaussian elimination. This involved converting  $A$  to upper-diagonal form then back-substituting to find the unknowns  $x$ . Although the dimensions of  $A$  were relatively small (compared, say, to a finite element implementation), it was a relatively full matrix and typically consumed approximately 500 megabytes or more of storage space. This was more storage than was available in random access memory, so it was necessary to store  $A$  on disk and to use out-of-core techniques when performing the Gaussian elimination. A specific out-of-core method was developed to ensure an efficient solution. The method involved manipulating matrix elements in the same order in which they were stored. This allowed large blocks of the matrix to be read from disk, processed, then returned to disk. This was much more efficient than alternative methods of processing the matrix elements.

In addition to the out-of-core capabilities, the solution method allowed a

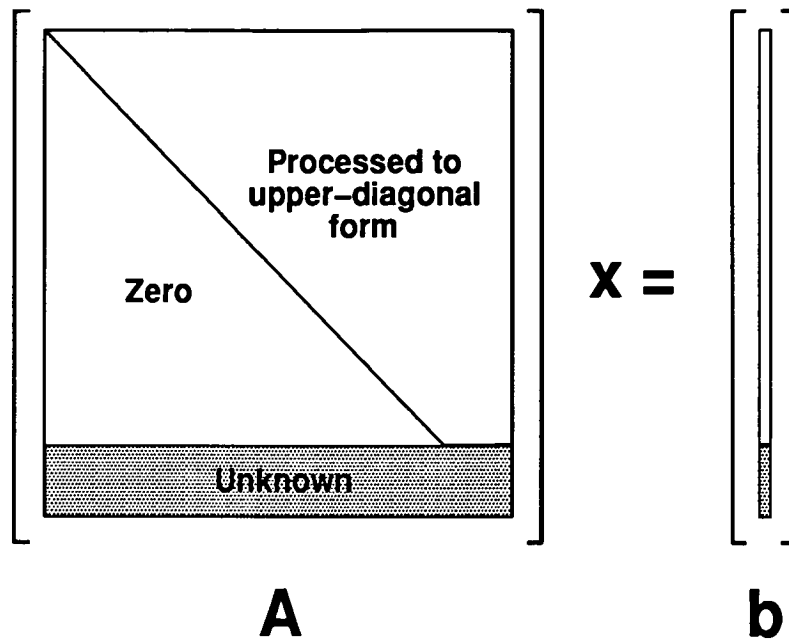


Figure 5.8: *Matrix  $\mathbf{A}$  and vector  $\mathbf{b}$  from equation (4.20) after processing as far as possible to upper-diagonal form before the transvenous electrodes were defined*

solution to be almost fully calculated then used as the basis of calculations for new electrode configurations. This feature was especially advantageous when considering different transvenous electrodes and often resulted in substantial savings in processing effort and time. In this procedure, most or all of the torso structure was defined, along with any invariant electrodes, with appropriate use of subregions, and this part of the problem was processed to the stage of equation (4.20). The aim was to build  $\mathbf{A}$  so that all the pre-determined parts were in the upper rows and all the new parts were in the lower rows. Matrix  $\mathbf{A}$  was turned into upper-diagonal form but only down to the last known row. At this point processing was stopped and the matrix saved, along with the appropriately modified vector  $\mathbf{b}$  and a string of numbers indicating the status of the calculation (Figure 5.8). In many cases, most of the processing of the problem had been encountered by this stage. For each variation of the problem to be considered, the unknown parts of the torso and electrodes were defined and the remaining rows of  $\mathbf{A}$  and  $\mathbf{b}$  calculated. The process of converting  $\mathbf{A}$

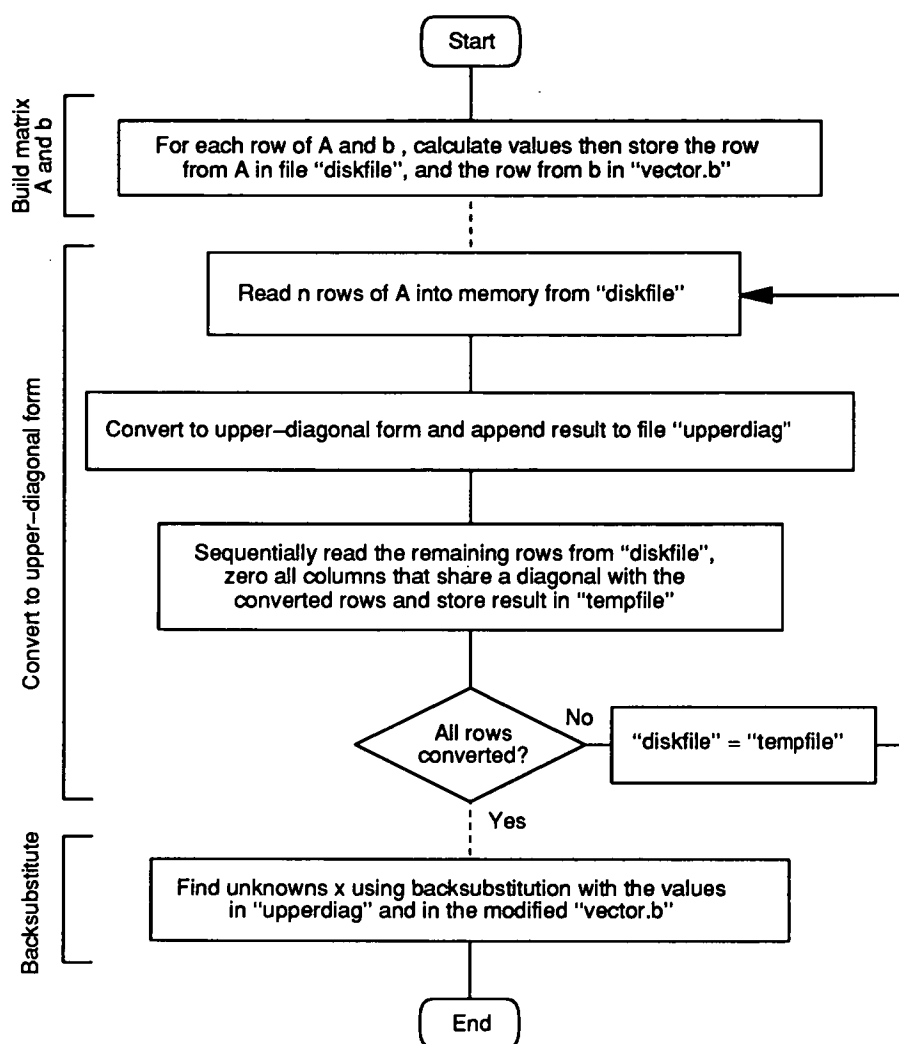


Figure 5.9: Procedure for solving equation (4.20)

to upper-diagonal form was then resumed and the final solution found. This procedure allowed, for example, different transvenous electrodes to be tested in the one torso, and was used to relatively quickly optimise electrode type and position. The solution procedure is summarised in Figure 5.9.

### Postprocessing

The postprocessing done after solving the matrix equations included the calculation of potentials and gradients at points inside regions and the calculation of the boundary potential gradients. Internal potentials and gradients were found by calculating matrix elements for the discretisation of equations (4.21)

and (4.22) then multiplying out the matrix elements with the known boundary values. These were then stored on disk and could then be used in calculations for different electrode configurations if none of the region elements changed. This avoided the need for recalculation of the matrix elements and greatly reduced the calculation time for the new configurations.

The potential gradient on the boundary of the regions was calculated as the vector sum of the components of the gradient. There were three components to the gradient at the boundary, one in the normal direction and two in the tangential directions (Figure (5.10)). The component in the normal direction was already known from the solution of equation (4.20). The components in the tangential directions were not already known and had to be calculated. This involved using an approximation because it was not possible to calculate the tangential gradients directly using the boundary element method. This was because the boundary element discretisation assumed a constant potential over the surface of individual elements. Therefore, the tangential component of the gradient on the surface of the individual boundary elements was zero. However, the potential varied as step functions between adjacent elements, so on this scale the tangential gradient was not zero. The tangential gradient was calculated by fitting linear approximations to these step functions. To do this, the potential at the four nodes of each element was calculated by applying a spatial weighted average to potentials on adjacent elements. Then the tangential components of potential were calculated by linearly interpolating the nodal potentials.

### **Solution speed**

The speed at which a solution was obtained using the model was of interest, particularly when considering the practicality of the solution method. With the full human torso geometry, the time taken to solve for one electrode configuration took a total of nearly 69 hours. However, each modified electrode

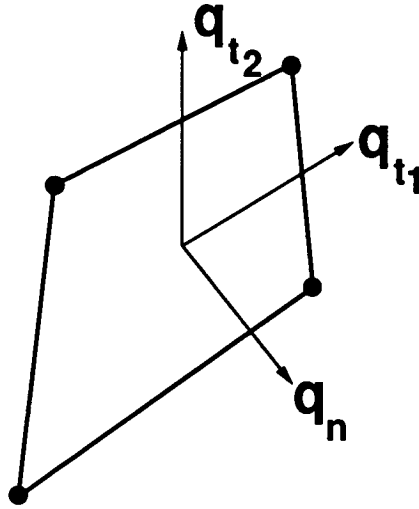


Figure 5.10: *Normal and tangential components of gradient on a boundary element.*

configuration only took approximately 2 hours to solve. The exact durations depended on the number of elements used to define the electrodes and on the extent of any mesh refinement.

The solution time was proportioned as follows for a typical solution. Calculating the geometry matrices  $\mathbf{A}$  and  $\mathbf{b}$  from equation (4.20) for all regions other than for venous blood and transvenous electrodes took approximately 11.5 hours. Converting matrix  $\mathbf{A}$  to upper-diagonal form, as far as possible without the venous blood and transvenous electrodes being defined, took a further 54 hours. This made a total of 65.5 hours. With the electrodes defined, construction of the remainder of matrix  $\mathbf{A}$  took 42 minutes and completing the conversion of matrix  $\mathbf{A}$  to upper diagonal form took an additional 1 hour 18 minutes. Back-substitution to find the vector  $\mathbf{x}$  of unknown boundary potentials and normal gradients took only a further 1 minute. Calculation of the potential and gradient at points inside the myocardium was done by first calculating the matrix relating the internal potentials and gradients to those on the boundary, taking 1 hour 18 minutes (coincidentally, the same duration as a previous calculation). This matrix was multiplied with the boundary values to obtain the potential and gradient at the internal points, taking approximately

1 minute. Subsequent internal point calculations for other electrode configurations used this same matrix and took only 1 minute. Calculating the gradient on the boundary, using the element normal gradients and the tangential gradients, calculated from interpolating the element potentials onto the element nodes, took approximately 5 minutes.

The solution time could be substantially reduced if better use was made of subregions to reduce the size of the blocks in  $\mathbf{A}$  and make it a more narrowly banded matrix. However, this may impact on the versatility of the model as it would make the mesh more complicated and therefore more time consuming to generate and more difficult to change.

# Chapter 6

## Validation of Numerical Methods

### 6.1 Introduction

There were a number of issues to consider when validating the model. These were conveniently separated into two groups: one concerning the implementation of the numerical methods and other the difference between the model and reality. The validation of the numerical methods is considered in this chapter. The numerical methods were validated by comparing the model with results from analytical and finite element models. Comparison with an analytical solution was to verify that the code was correct and to indicate the accuracy of the method. Comparison with finite element implementations was to more completely verify the code using realistic torso and electrode configurations. The closeness to reality is considered in the next chapter, where validation against experimental and clinical results is presented.

## 6.2 Comparison with Analytical Solution for Concentric Spheres

A concentric spheres model was used that consisted of four spheres: the outer sphere represented the chest and was configured as a subcutaneous patch electrode (+100V), the next sphere represented the epicardium, the next represented the endocardium and the inner sphere represented an endocardial electrode (-100V). Each sphere was constructed from 600 elements, the entire surface of both the outermost and innermost spheres were configured as electrodes to facilitate a simple analytic solution and the regions between the spheres were given the conductivity of body tissue, myocardium and blood. A section through the center of the spheres is shown in Figure 6.1. The radius of the spheres was 40, 30, 20 and 10mm.

The analytical solution for this problem is derived by first considering that the current flowing between spheres  $i$  and  $i + 1$  is

$$I_{i,i+1} = \frac{4\pi k_i^{i+1}(u_{i+1} - u_i)}{1/r_{i+1} - 1/r_i} \quad (6.1)$$

and that the total current flowing through each region is the same for each of the three regions. Also, the potential in the region between spheres  $i$  and  $i + 1$  at a radius  $r$  is

$$u_r = u_i + \frac{I}{4\pi k_i^{i+1}}(1/r_{i+1} - 1/r_i) \quad (6.2)$$

These expressions can be used to find the potential anywhere between the inner and outer spheres, while the potential gradient may be found by differentiating equation (6.2), so that the gradient at  $r$  is

$$q_r = \frac{\partial u_r}{\partial r} = -\frac{I}{4\pi k_i^{i+1} r^2} \quad (6.3)$$

Results are given in Table 6.1 and Figure 6.2. Table 6.1 gives values for

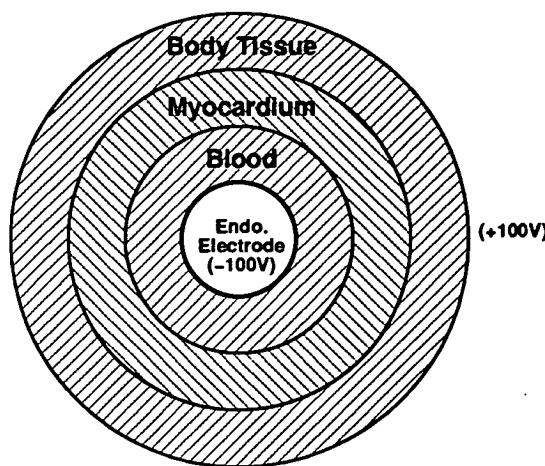


Figure 6.1: *Slice through the center of the concentric spheres model*

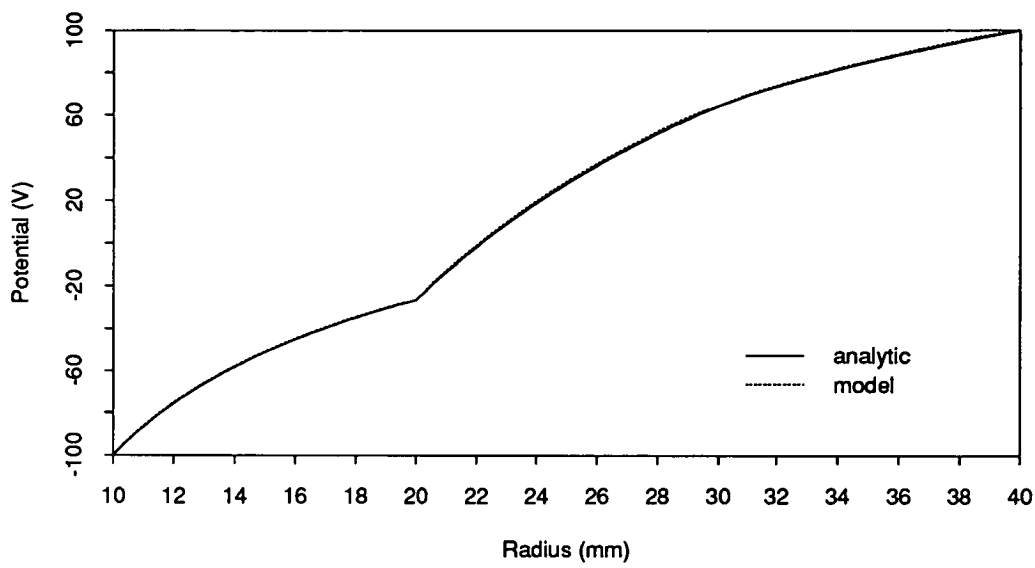
	Radius (mm)	Potential			Potential gradient		
		Model (V)	Analytic (V)	Error <sup>a</sup> (%)	Model (V/mm)	Analytic (V/mm)	Error (%)
endocardium	20	-26.753	-26.640	0.06	13.735	13.653	0.60
myocardium	25	28.975	27.973	0.50	8.756	8.738	0.21
epicardium	30	64.255	64.382	0.06	6.153	6.068	1.40

<sup>a</sup>with respect to the anode-cathode voltage of 200V

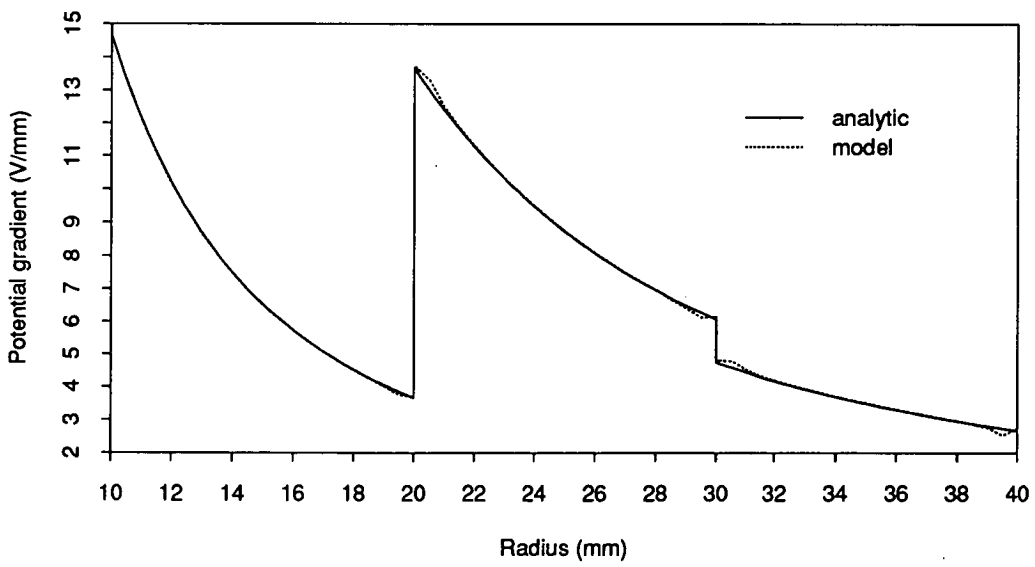
Table 6.1: *Results from the concentric sphere model*

the potential and potential gradient on the epi- and endocardium and in the myocardium and it is evident that the model closely replicates the analytic solution. The errors that arise are small and occur mainly because the analytic solution uses spheres of perfect shape, whereas the model uses spheres with surfaces that are approximated by flat quadrilateral elements.

Figure 6.2 shows the potential and potential gradient along a radius from the inner to the outer sphere. Extremely good agreement is observed between the analytic and model solutions. The slight loss of accuracy that can be observed in the gradient for radii close to the surface of each sphere, though a characteristic of the BE method, can be reduced by applying appropriate techniques, if necessary.



(a) Potential



(b) Potential gradient

Figure 6.2: *Potential and potential gradient within concentric spheres*

### 6.3 Comparison with Finite Element Solution for a Cube

The concentric spheres results verified the model for regularly shaped electrodes and for different conductivity material but not for electrodes covering only part of a surface. This latter case is important because high potential gradients are developed near these electrodes and may result in relatively large numerical errors. Consequently, the model was also tested using a cube with surface patches and the results were compared to a FE solution. Some of the nodes on the surface of the cube were set to  $+100V$  and some were set to  $-100V$  so as to simulate two surface patches. The patches were on opposite faces of the cube, were square and occupied  $1/25^{th}$  of the face area. It was expected that the accuracy of the BE and FE solutions would increase as the number of nodes in the cubes were increased so a number of cubes were constructed to test this.

Figure 6.3 shows a cross-section through the three FE meshes modelled. The elements were 8 node bricks. The first mesh had 1037 nodes, the second had 7417 nodes and the third 56177 nodes. They were constructed by creating the first mesh, then splitting the elements in this to form the second mesh, and splitting again to form the third. Each split resulted in eight bricks being formed from each original brick. Four BE meshes were used. These were constructed of quadrilateral surface elements. There were 150, 276, 492 and 948 nodes in the four meshes.

Figure 6.4 shows the potential along a line joining the centers of the patches for both the FE and BE solutions. The solutions were very different for the coarse meshes, but converged as the meshes were refined. As they converged, FE potentials decreased while BE potentials increased in value, indicating that the exact solution was probably spanned by the original coarse solutions.

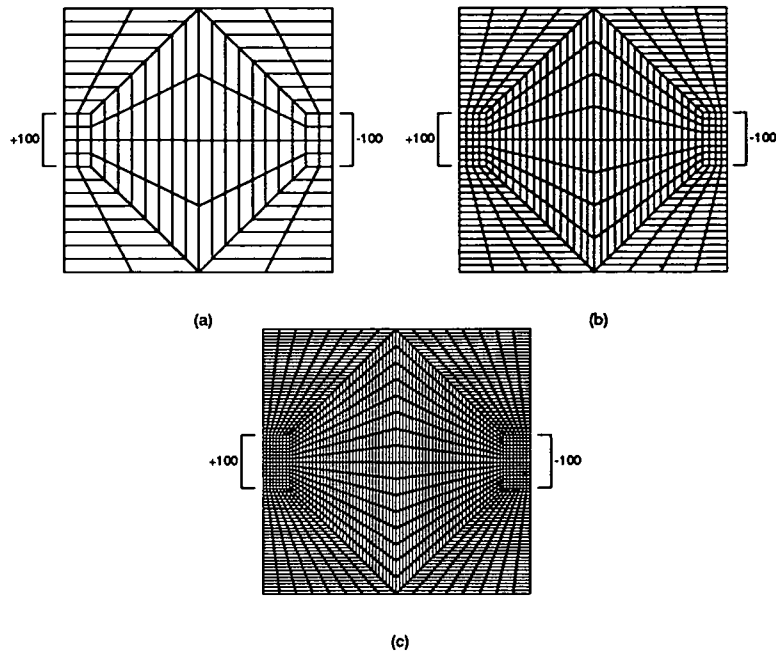


Figure 6.3: *Finite element meshes (a) coarse, (b) each element split once (c) each element split twice. Surface nodes beneath the markers are set to the potentials indicated.*

Convergence of the solutions indicated the error, arising mainly from high potential gradients near the patches, became relatively small. As can be seen from Figure 6.3, the FE meshes were made somewhat more dense near the patches to try and overcome this problem, as were the BE meshes.

## 6.4 Comparison with Finite Element Solution for Realistic Torso and Electrodes

Two different models, the BE model and a FE model, were used to calculate the potentials in the myocardium for a realistic thorax and the results were compared. The thorax for the BE model was as described in section 5.2, without ribs. The thorax for the FE model was generated from the BE model and contained approximately 160,000 nodes, with a high density of nodes near the electrodes. The construction of the FE thorax is described in section 5.2.

Standard Enguard atrial and ventricular endocardial electrodes, located

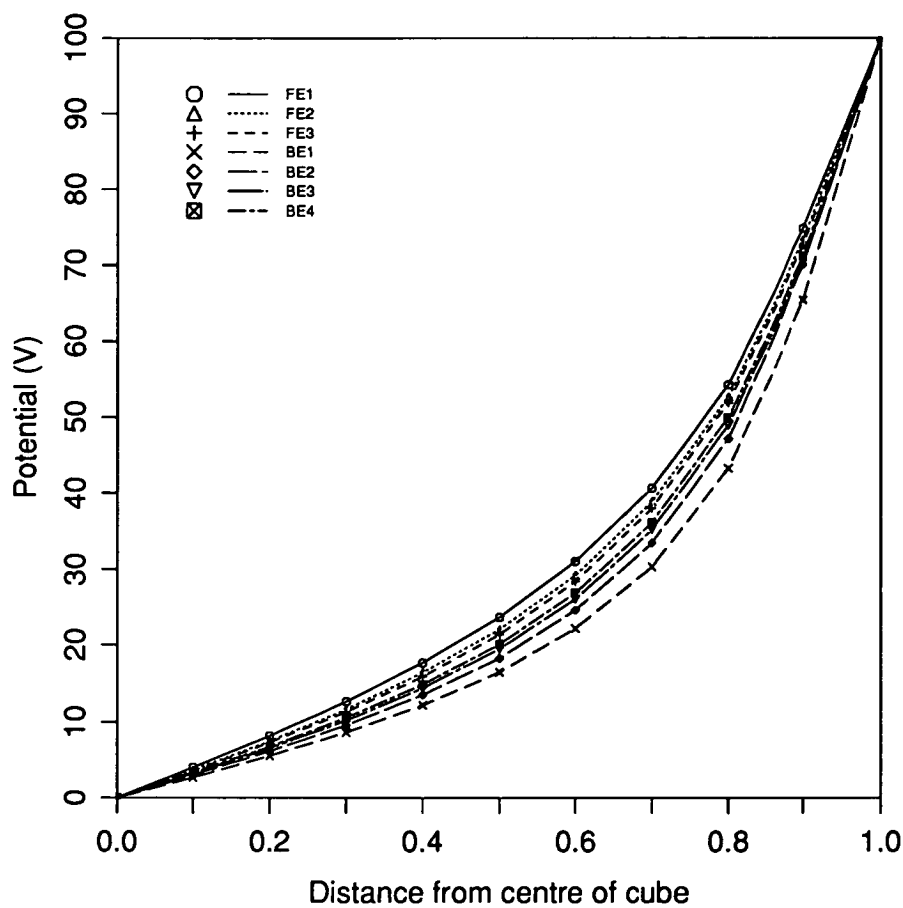


Figure 6.4: *FE* and *BE* results for meshes that are progressively refined

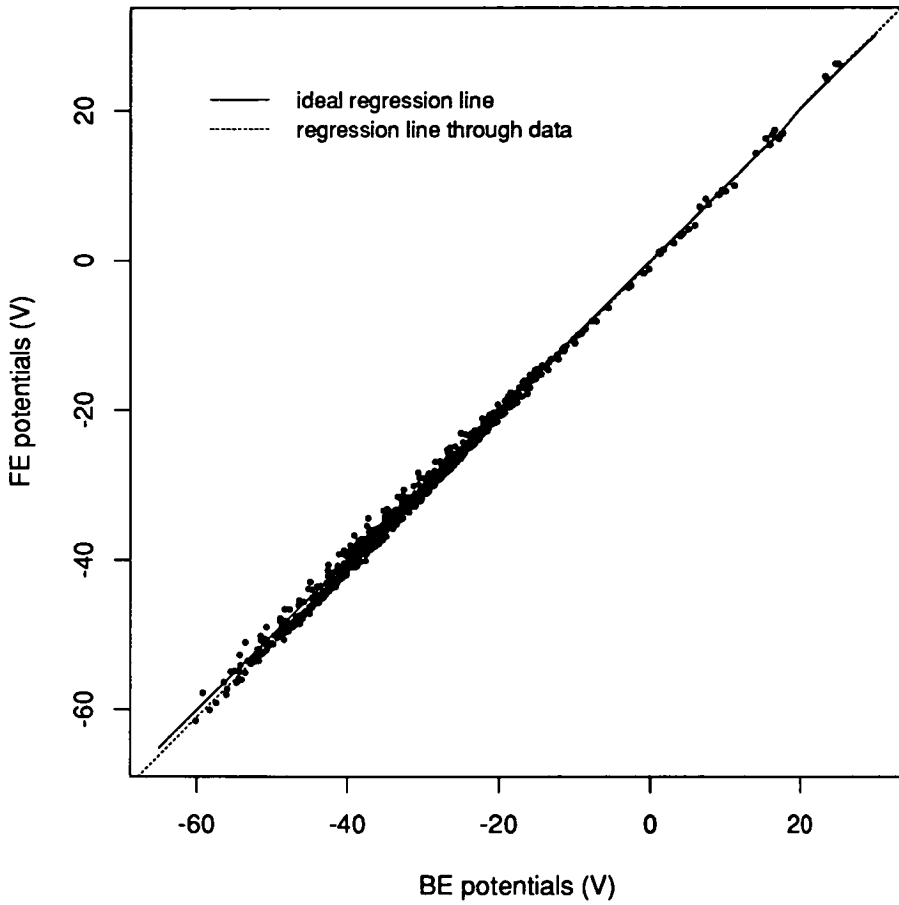


Figure 6.5: *Comparison of FE and BE results for endocardial electrodes in the RV and SVC ( $RE = 2.8\%$ )*

in the superior vena cava and right ventricle, respectively, were used in both models. (Enguard sensing/pacing defibrillation leads are manufactured by Teletronics Pacing Systems. Details of these leads are given in Section 8.2 and Appendix D.) The potential at 1152 locations in the myocardium was found for each model and the models compared by comparing these values.

A plot of FE against BE potential at each point is shown in Figure 6.5. Ideally, the points would lie along the a line through the origin with a slope of 1. Actually, the points were scattered closely about this line. The least squares regression line through the points had a slope of 1.0125 and a  $y$ -intercept of -0.2133. The average relative error between the FE and BE potentials was 2.8%, indicating very good agreement.

This result means that the use of the model with a realistic body was valid

and that even with the complex geometry of the body numerical errors were small.

# Chapter 7

## Validation in Sheep and Humans

### 7.1 Introduction

The previous chapter dealt with validation of the numerical methods used in the boundary element model. The conclusion was that the numerical methods were implemented correctly and gave accurate solutions. This second chapter on validation deals with the accuracy with which the model predicts the electric field in a sheep and the performance of defibrillators in humans.

The accuracy of the model is determined by the the model's representation of reality. There are always some differences for a model of this type, whether it be in regard to the structure and properties of the torso, the nature of the electrode-torso interface or the criteria that determine fibrillation and defibrillation. This validation of the model quantifies the difference between the model and reality by comparing results from the model to measured values in humans and sheep. Comparison with experimental results indicated how closely the approximations inherent in the model matched reality. Comparison with clinical results indicated how well the model results matched a set of results from humans.

## 7.2 Sheep Validation

In this validation, epicardial potentials calculated using a sheep model were compared to epicardial potentials measured on a live sheep implanted with defibrillator electrodes. The purpose was to verify the capability of the model to predict the electric field in a real thorax.

### Experimental apparatus

The experimental apparatus (Figure 7.1) consisted of a sheep, delivery electrodes, a current source, a multichannel recording device and a heart-sock. The sheep was a cross-bred ewe weighing  $43\text{kg}$ . There were two (Enguard) delivery electrodes of identical dimensions ( $3\text{mm}$  diameter,  $6\text{cm}$  long) which were located in the superior vena cava and right ventricle. The two electrodes will be termed the anode and cathode, respectively. The current source was a  $100\text{Hz}$ ,  $0.80\text{mA}$  constant current source. One source output was connected through a resistor (used to verify current) to the anode. The other output was connected directly to the cathode. The multichannel recording device was a 128 channel device for recording potentials with an input range of  $0 - 50\text{mV}$ , was produced in-house and named “EDAS”. Each EDAS channel was operated at  $1000\text{ Hz}$ . The heart-sock was an elastic sock that fitted over the heart with 64 electrodes distributed on it that made contact with the epicardium. The sock was constructed from a thin, closely-knit woven material. Although the material was an insulator, the woven material covered only about 20% of the epicardial surface. Considering the relatively good conductivity of the fluid bathing the sock, the influence of the heart sock on the electric field was considered small compared to other sources of error.

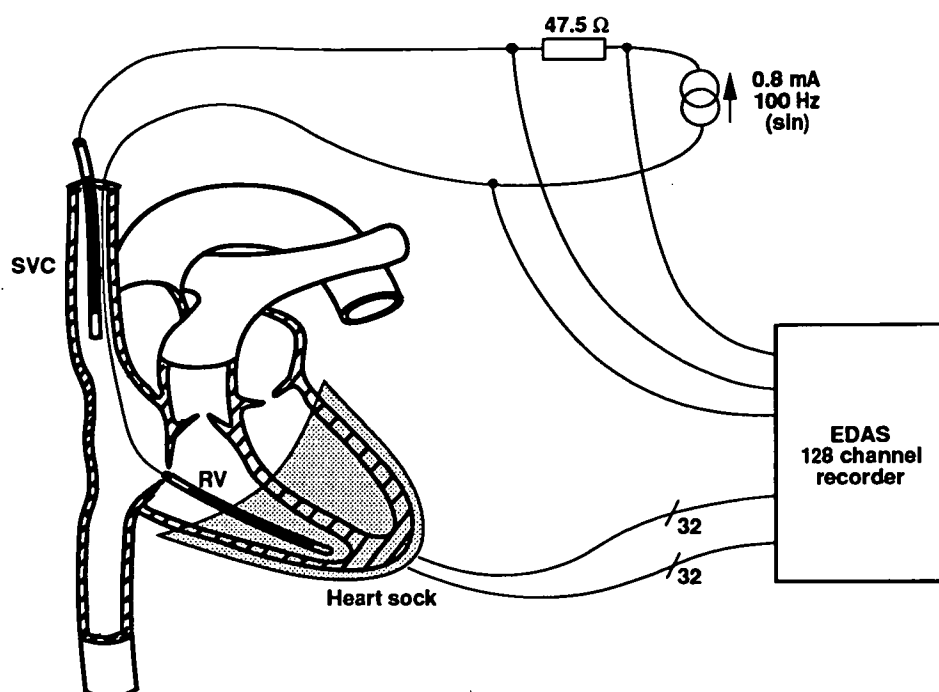


Figure 7.1: Apparatus to recording potentials from sheep

### Experimental procedure

The experimental procedure was as follows. The sheep was placed on an operating table and anaesthetised. The chest was opened and the heart exposed by removing the third rib on the left side and spreading the chest wall. The two delivery electrodes were implanted through the Jugular vein. The correct positioning of the electrodes was ensured manually by feeling their position inside the exposed heart and vessels. The cathode was positioned with the tip of the lead in the apex of the right ventricle. The anode was positioned in the superior vena cava just above the junction with the right atrium. The heart-sock was pulled over the heart (from the apex) such that it covered the ventricles. The heart was repositioned, saline added to the cavity and the chest wall closed. (The saline used was diluted normal saline with a conductivity of approximately  $400\Omega\text{cm.}$ ) With the chest closed, internal suction was applied to remove excess saline. The current source was then connected to the delivery electrodes and the potentials on the heart-sock electrodes were recorded using EDAS. The sheep was then killed, the chest opened and the

heart removed. The position of the heart-sock electrodes on the epicardium were recorded. The heart was frozen and then sliced from the apex into 1cm thick slices. The endocardial surfaces were traced onto paper and the tracings digitised. The sheep's thoracic geometry was discretised for use in the model as outlined in section 5.2. The same tissue conductivity values were used in the sheep model as for the human model. The delivery electrodes used in the model were endocardial electrodes of the same dimensions as those used in the sheep.

## Results

The results are presented for the equivalent of a static applied potential field of zero on the cathode and 50mV on the anode. The epicardial potentials from the sheep model and experiment were mapped onto the epicardial surface (Figure 7.2) and plotted against each other (Figure 7.3).

For the 64 epicardial potentials, the correlation coefficient ( $CC$ ) was 0.464 and the average relative error ( $RE$ ) was 23.6%, with a maximum individual  $RE$  of 57.9%. Resistance between the cathode and anode from the experiment and model were  $75.8\Omega$  and  $57.6\Omega$  respectively, giving a relative error of 31.6%, which was of the same order as the relative error in epicardial potentials.

## Discussion

Both experimental and model-generated epicardial maps had potentials increasing from apex to base with the lowest potentials over the right ventricle. However, the maps were visually different. Part of the reason for this was the high resolution of the maps. The contour spacing was only 2mV, which was just 4% of the applied voltage. The reason for this was that all potentials on the epicardial recording electrodes were grouped within the range 6 – 19mV. This was due to the recording electrodes being spaced relatively uniformly around the cathode (which was at 0mV) while the anode (at 50mV) was relatively

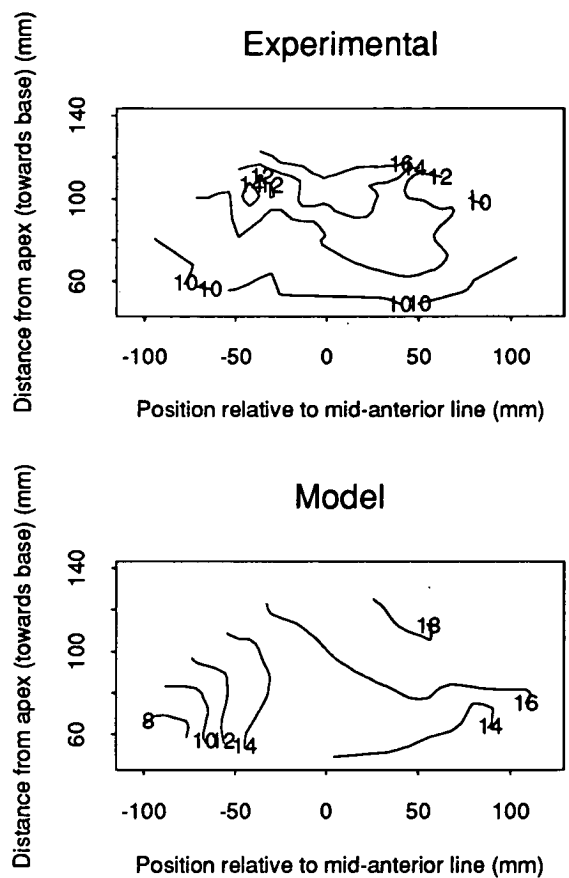


Figure 7.2: *Epicardial potential maps (mV) for experimental and model results for endocardial electrodes (50mV signal) in a sheep*

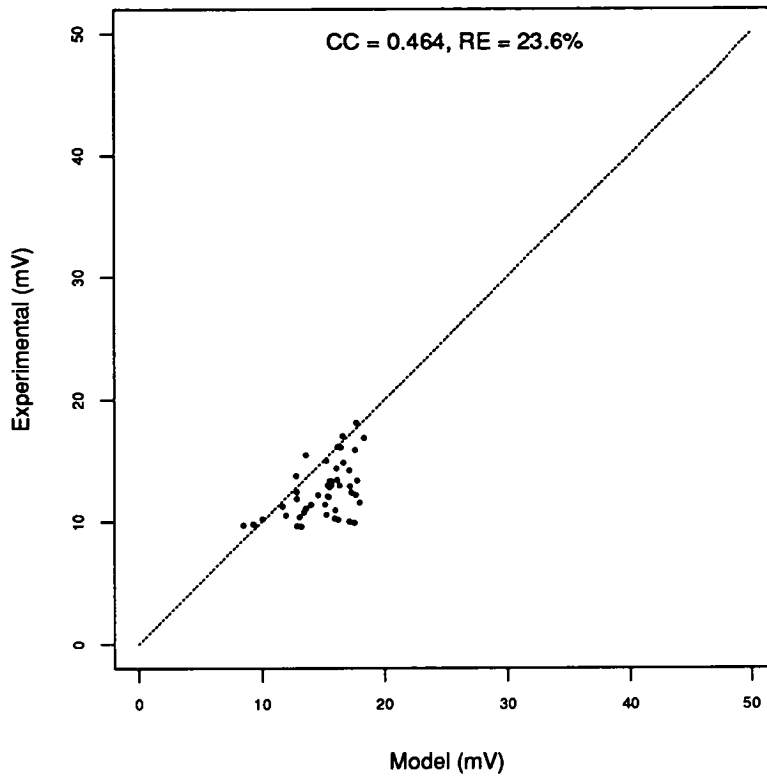


Figure 7.3: *Correlation of epicardial potentials for experimental and model results for endocardial electrodes (50mV signal) in a sheep*

distant.

The low error in potentials and the closeness of the resistance match indicate that, on the whole, the field magnitudes are corrects. The difference in epicardial patterns may be the result of neglecting myocardial anisotropy in the model.

Potentially, the main sources of experimental error were associated with the tissue conductivity values, the sheep torso geometry and the electrode locations used in the sheep model. Of these, errors due to uncertainty in torso geometry and electrode location were probably the most significant. In particular, the exact shape and orientation of the heart was difficult to determine, since it was beating when the CT scans were taken and its position was disturbed when the heart sock was fitted.

In regard to the measuring electrodes, the error due to the uncertainty of location may be estimated from the error in electrode position and the strength

of the electric field near the electrodes. The error in position of the electrodes was estimated as approximately  $1\text{cm}$ . The average field strength near the electrodes was, from the model, approximately  $2.5\text{mV/cm}$ . Therefore, the potential recorded by the epicardial electrodes was in error by up to  $2.5\text{mV}$  due to uncertainty in torso geometry and electrode location.

Improvements to the experiment could include repeating the experiment using many sheep with statistical analysis of the results. Also, sheep tissue conductivity could be measured *in vivo* to provide individually matched conductivity values for use in the model. High resolution CT or MRI scans could be taken of each sheep to accurately model the sheep torso geometry and the exact positions of the electrodes. Electrode position could alternatively be found from two x-ray images taken at right angles.

### 7.3 Human Comparison

A comparison was made between results calculated by the model and measured on humans. Measured values of resistance and voltage at defibrillation threshold were obtained from Teletronics Research and Development department for 29 patients implanted with standard Enguard right ventricular and atrial endocardial electrodes, and for 8 patients implanted with an additional subcutaneous patch ( $28\text{cm}^2$ ). The patients implanted with subcutaneous electrodes could not be adequately defibrillated with endocardial electrodes alone. Predicted values of resistance and voltage at defibrillation threshold were calculated using the model with a single arbitrary human torso geometry (no ribs) and the standard Enguard defibrillator electrodes with and without a subcutaneous patch. The predicted value of resistance was calculated by dividing the applied voltage by the total current. Predicted values were also found for the subcutaneous patch configuration with ribs in the model. Thorax geometry data for the patients was unavailable, so no attempt was made to individually

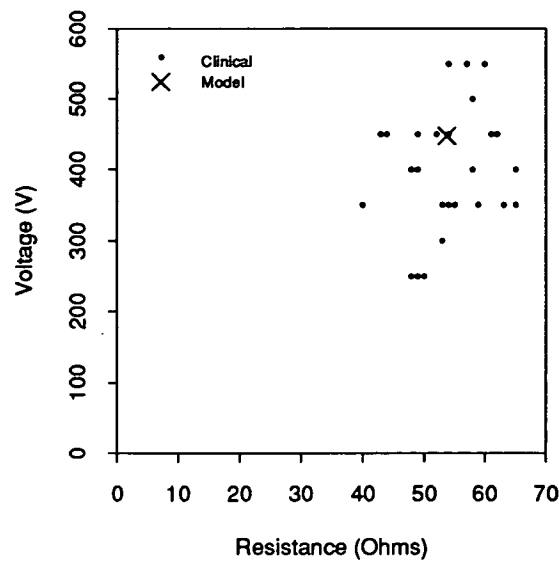
model patients.

The clinical and model results were compared by considering the relative error between the model result and the mean and individual clinical results. The relative error of the mean clinical result and the model result was a measure of how close the model result was to the mean of the clinical results. The mean relative error between the individual clinical results and the model result was a measure of the distribution of the clinical results around the model result, and reflected the natural variation and experimental errors inherent in the clinical data. The relative errors are given in Table 7.1.

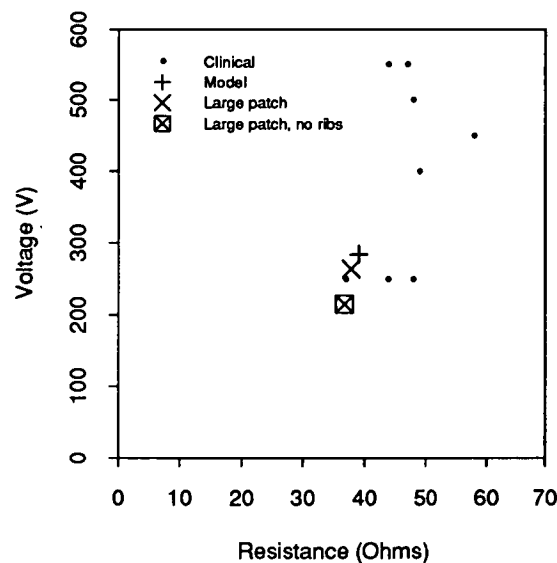
The voltage and resistance values for the endocardial-only configuration were plotted in Figure 7.4(a). The model result ( $53.7\Omega$  and  $447V$ ) was within the range and near the centroid of the clinical values ( $54.1 \pm 6.4\Omega$  and  $408 \pm 92V$ , mean  $\pm$  s.d.). Being near the centroid meant the relative error for the mean clinical results was low, while the spread of the clinical values meant the individual relative error was relatively high. This result supports the premise that, for this configuration, the model adequately predicts defibrillator performance in a clinical setting.

The voltage and resistance values for the endocardial-patch configuration were plotted in Figure 7.4(b). The model result without ribs ( $36.8\Omega$  and  $215V$ ) was outside the range of the clinical values ( $46.9 \pm 5.9\Omega$  and  $400 \pm 134V$ , mean  $\pm$  s.d.). The mean relative error was relatively large because of the large difference between the mean clinical and model results and was of similar magnitude to the individual relative error, which again reflected the large spread of the clinical results. Adding ribs to the model brought the result ( $37.8\Omega$  and  $265V$ ) within the range of the clinical values and improved the relative error values. This result suggests that ribs should be used in the model when considering subcutaneous electrodes. The model was sensitive to patch size with a larger patch ( $78cm^2$ ) lowering voltage and resistance.

That the subcutaneous patch model results were not near the centroid of



(a) Enguard electrodes in the right ventricle and superior vena cava



(b) Enguard electrodes in the right ventricle and superior vena cava and a subcutaneous patch

Figure 7.4: Comparison of defibrillation voltage and resistance from the model and from measurements in humans

Electrodes	Ribs in model	$RE_{(mean\ clinical)\ and\ model}$		mean $RE_{clinical\ and\ model}$	
		voltage	resistance	voltage	resistance
RV <sup>-</sup> , SVC <sup>+</sup>	no	9.4	0.8	23.4	11.6
RV <sup>-</sup> , SVC <sup>+</sup> , SQ <sup>+</sup>	no	46.2	21.6	53.2	24.4
RV <sup>-</sup> , SVC <sup>+</sup> , SQ <sup>+</sup>	yes	33.9	19.4	44.0	22.5

Table 7.1: *Relative error (%) (RE) between clinical and model results for configurations with endocardial electrodes in the right ventricle (RV) and superior vena cava (SVC) and an apical subcutaneous patch (SQ)*

the clinical results is not of great significance in this instance since it was only the patients in which an endocardial-only system was unsuccessful that were implanted with the subcutaneous patch and it is known that the defibrillation thresholds for these patients were higher than average. However, there still remains the question of whether myocardial and skeletal muscle anisotropy would significantly raise the model thresholds if included in the model.

# Chapter 8

## Investigations

### 8.1 Introduction

The boundary element model was used to investigate the performance of different electrode configurations. Some configurations investigated were representations of commercial defibrillator leads while others were created for use with the model. The aim of the investigations was firstly to ensure that it was practical to use the model to test different electrode configurations. A second aim was to compare the performance of configurations to find the most promising for further evaluation in animal or clinical trials. In the sections that follow, the electrode configurations that were modelled are described and the investigations and results are presented and discussed.

### 8.2 Electrode Types

Transvenous, subcutaneous and epicardial electrodes were modelled. Some of the transvenous electrodes were based on Enguard defibrillation leads produced by Teletronics. Other transvenous electrodes were longer or shorter than the Enguard electrodes and were positioned differently in the venous system. Some subcutaneous patch and epicardial electrodes were of similar shape to

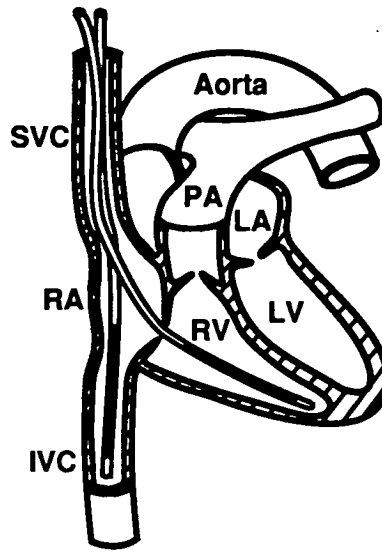


Figure 8.1: *Example of a configuration with endocardial electrodes in the IVC and RV*

commercially available items while others were of quite different shapes and sizes Figure 8.1 illustrates two transvenous electrodes positioned in the heart and venous system.

From the perspective of modelling for defibrillation purposes, Enguard leads were endocardial catheters incorporating a single active braid electrode. Of the whole lead, only the electrode braid was actually modelled, the remainder of the lead being passive and small and having little effect on the field. The braid was  $6\text{cm}$  long and  $3\text{mm}$  in diameter. The location of the braid relative to the electrode tip depended on the model number of the lead.

Four Enguard leads were modelled. One was a right ventricular lead with a tip to braid spacing of  $1\text{cm}$ . The others were atrial leads with the lead tip fixed in the right atrium. One was the standard atrial lead, model number 040-020, and this lead had a tip to braid spacing of  $8.5\text{cm}$ . The remaining two leads, models 040-022 and 040-024, had spacings of  $14.5$  and  $17.5\text{cm}$ , respectively. The tip to braid spacing was the main determining factor in locating the braid for a given tip location and lead orientation. For standard tip positioning, the braid of model 040-020 was in the superior vena cava just above the junction of the right atrium, model 040-022 was  $6\text{cm}$  higher and model 040-024 was  $9\text{cm}$

higher than standard and entered the subclavian vein. The standard position of the right ventricular lead was with the tip of the lead at the apex of the right ventricle and the braid within the ventricle. Refer to Appendix D for further details of Enguard electrodes.

Subcutaneous patch electrodes, as previously discussed (Section 5.2), were represented simply by potentials specified on torso surface elements. Epicardial patch electrodes were represented by a region over the epicardium with the potential specified on the inner surface of the patch and zero current specified normal to the outer surface. The location, size and shape of these regions were located by specifying surface elements from the torso mesh.

### 8.3 Electrode Configurations Tested

The electrode configurations tested included various combinations of the available electrode types. The configurations will be described under the appropriate headings below. Before doing so, though, a note regarding terminology. For transvenous systems, there was usually an electrode in the right ventricle and this was referred to as the cathode. Unless otherwise stated, this was a standard Enguard right ventricular electrode. There was also an electrode located outside the heart and this was referred to as the anode.

#### **Transvenous Anode Within the Venous System (TA-VS)**

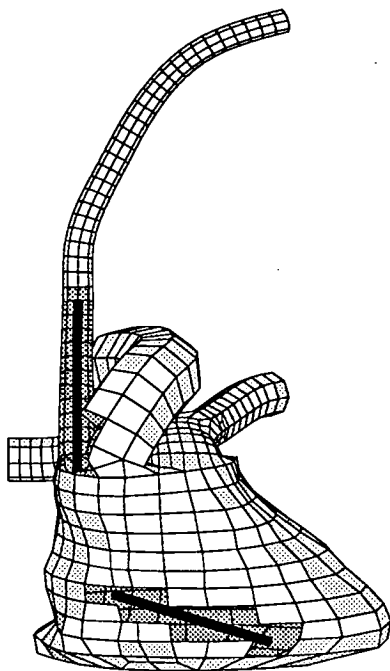
A number of transvenous electrode configurations were modelled. These consisted of a cathode in the right ventricle and an anode elsewhere in the venous system and were labelled as TA-VS configurations. Each anode had the same dimensions as the braid of an Enguard atrial lead. The position of the anode was different in each configuration and encompassed locations in the subclavian vein, superior vena cava, right atrium and inferior vena cava. A total of 29 anode positions were used.

The anode position of configuration TA-VS 1 corresponded to the standard Enguard atrial lead (model number 040-020). This configuration is illustrated in Figure 8.2(a) (and also Plate 3). The figure shows an anterior view of the heart with some surface elements removed to expose the electrodes. The anode positions of configurations TA-VS 2 and TA-VS 3 corresponded to Enguard atrial leads 040-022 and 040-024. These configurations are illustrated in Figures 8.2(c) and 8.2(d), respectively.

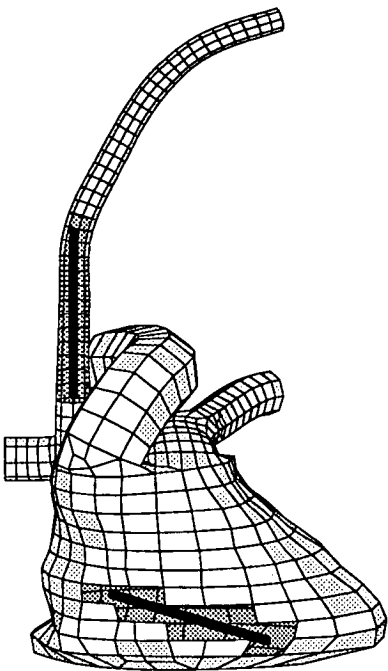
Further configurations had anodes located elsewhere. The anode in the example configuration illustrated in Figure 8.2(b) was positioned in the superior vena cava slightly above the position of the standard anode. Figure 8.3 illustrates configurations with anodes positioned below the standard anode position. These electrodes were partly or wholly in the right atrium or inferior vena cava. The anode in Figure 8.3(a) just entered the right atrium. The anode in Figure 8.3(b) passed through the right atrium and came relatively close to the cathode. The anode in Figure 8.3(c) was partly in the right atrium and partly in the inferior vena cava. The anode in Figure 8.3(d) was mostly within the inferior vena cava. The anodes in Figures 8.3(e) and 8.3(f) were entirely within the inferior vena cava. The anodes shown in Figures 8.2(d) and 8.3(f) were at the extreme upper and lower positions considered.

### **Transvenous Anode with Subcutaneous Patch(TA-SQ)**

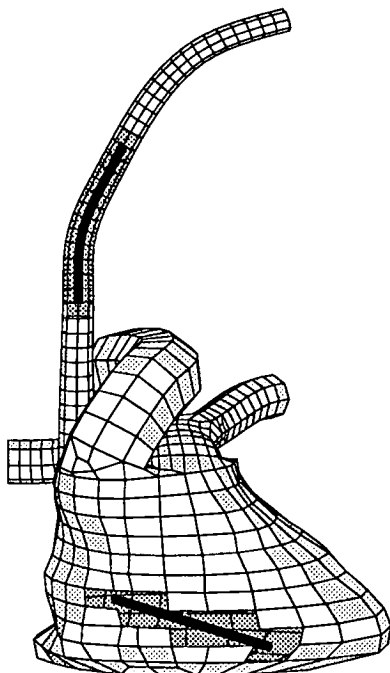
Configurations TA-SQ 1-4 used a subcutaneous patch together with a cathode and Enguard anode. The patch had an area of  $78\text{cm}^2$  and was located on the left chest wall over the apex of the heart. The patch was configured as a second anode in configurations TA-SQ 1-3, in line with normal clinical practice, and as a second cathode in configuration TA-SQ 4.



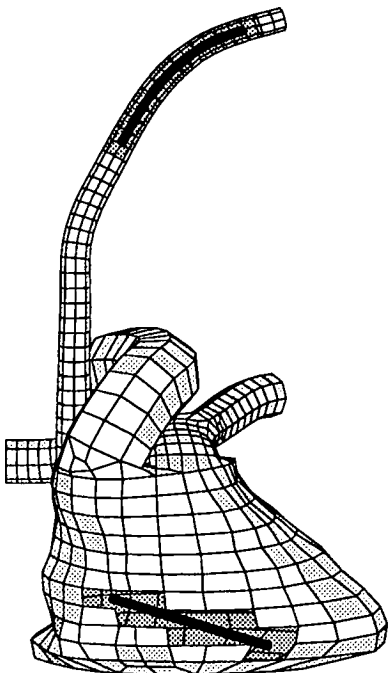
(a) TA-VS 1



(b) 2.5cm above TA-VS 1

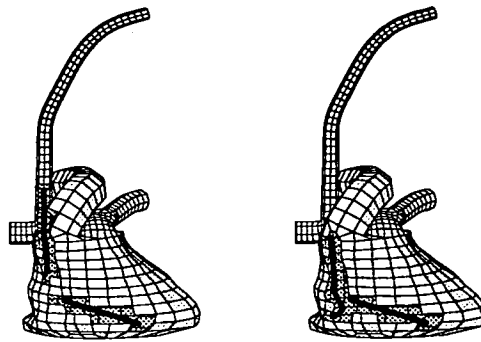


(c) TA-VS 2 (6.0cm above  
TA-VS 1)



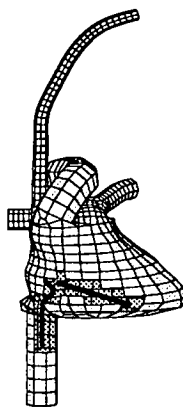
(d) TA-VS 3 (9.0cm above  
TA-VS 1)

Figure 8.2: Anode at or above the standard position (configuration TA-VS)

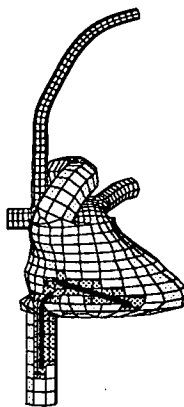


(a)  
2.5cm below  
TA-VS 1

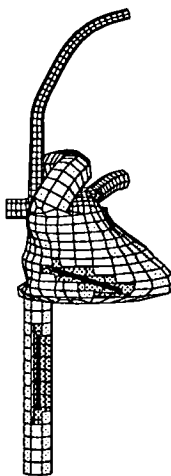
(b)  
6.0cm below  
TA-VS 1



(c) 6.7cm  
below TA-  
VS 1



(d) 8.4cm  
below TA-  
VS 1



(e) 11.0cm  
below TA-  
VS 1



(f) 17.0cm  
below TA-  
VS 1

Figure 8.3: *Anode below the standard position (configuration TA-VS)*

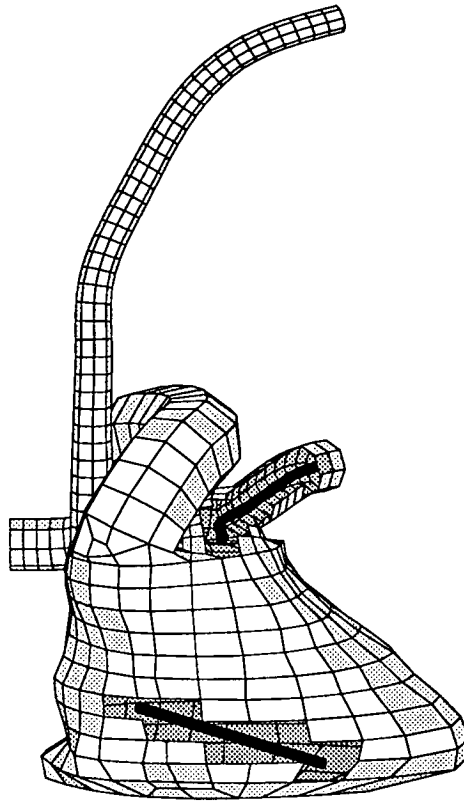


Figure 8.4: *Pulmonary artery transvenous electrode (configuration TA-PA)*

### **Transvenous Anode in the Pulmonary Artery (TA-PA)**

An alternative to the anode being in the venous system was for the anode to be located in the pulmonary artery. This configuration, TA-PA, is illustrated in Figure 8.4. The anode was positioned mainly in the left branch of the pulmonary artery. This was because it would not fit entirely within the main artery and also because positioning in the left branch was more favourable with regard to the field strength in the left ventricle.

In configuration TA-PA 1, the standard cathode was used. A subcutaneous patch was added as an anode in TA-PA 2 and as a cathode in TA-PA 3. A single cathode in the inferior vena cava was used in TA-PA 4.

### **Partly Enlarged Cathode (EC)**

A cathode was constructed with one end partly enlarged (Figure 8.5). This cathode was used with the standard anode in configuration EC. The cathode

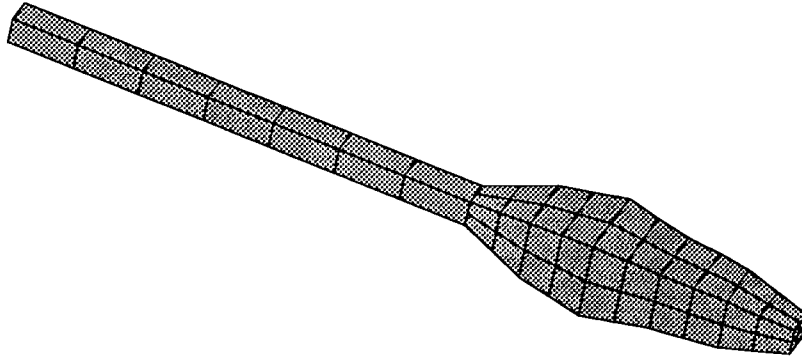


Figure 8.5: *Modified transvenous right ventricular electrode (configuration EC)*

was orientated with the enlarged end near the apex of the right ventricle. The aim was to reduce the current density near the end of the electrode by increasing the electrode size.

### **Cathode Length (CL)**

Configuration CL consisted of a standard anode and a cathode which was either an extended or shortened version of the standard Enguard cathode (Figure 8.6). The standard (Figure 8.6(b)), shortest (Figure 8.6(a)), extended (Figure 8.6(c)) and longest (Figure 8.6(d)) electrodes are illustrated.. In total, 16 different cathodes were tested with lengths from 1.5 to 11.0cm.

### **Epicardial Patch Pair (EPP)**

Configuration EPP consisted of a pair of epicardial patches constructed over the left and right ventricles (Figure 8.7). The size of the patches were  $49\text{cm}^2$  (left) and  $35\text{cm}^2$  (right). The patches were shaped to ensure a minimum separation between the patches of 1.5cm. This helped prevent excessively high current densities between the edges of the patches. A similar configuration was modelled by Kinst *et al.*[2]. They used two  $32\text{cm}^2$  patches located over the left and right ventricles.

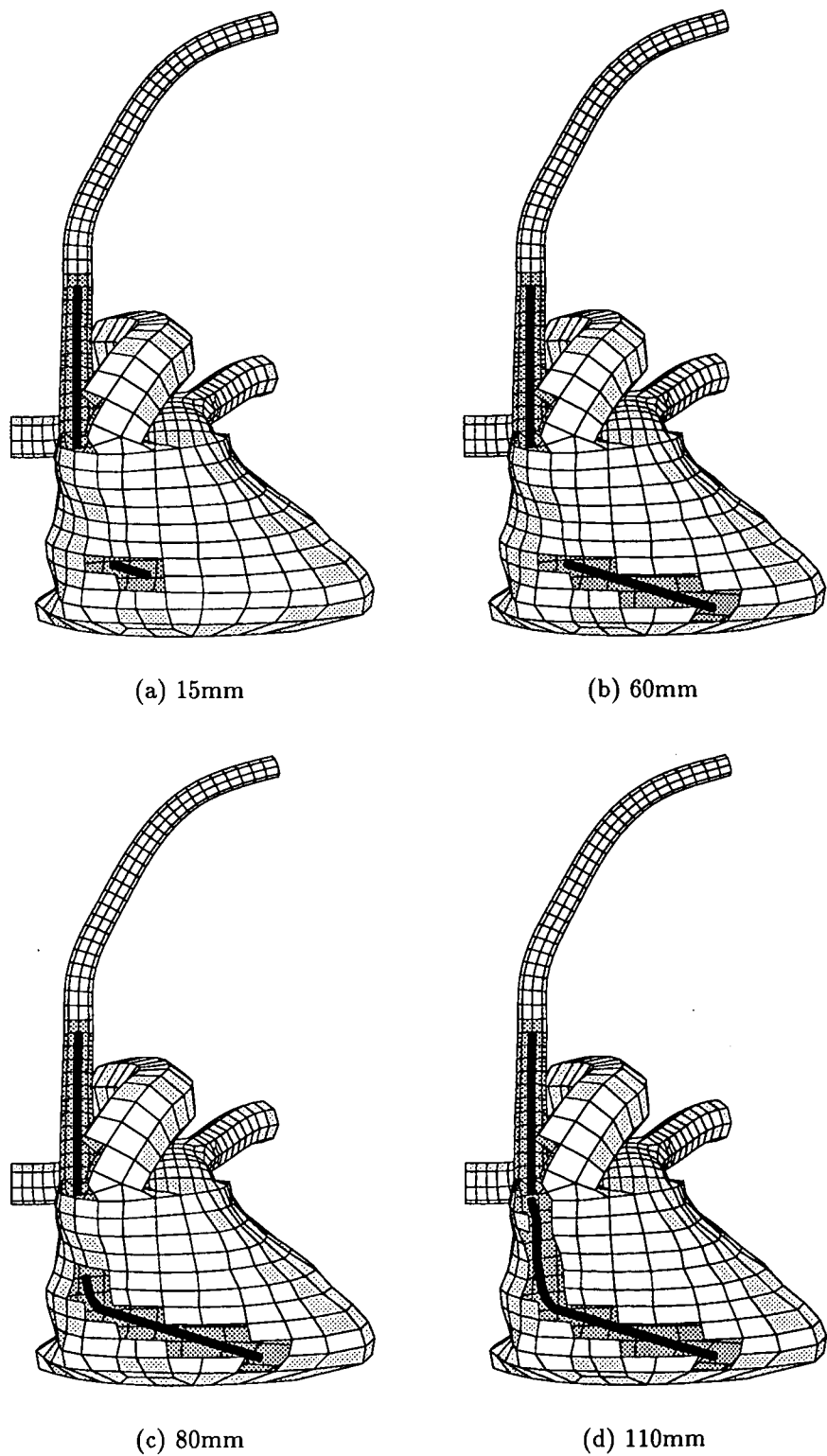


Figure 8.6: *Different length right ventricular electrodes (configuration CL)*

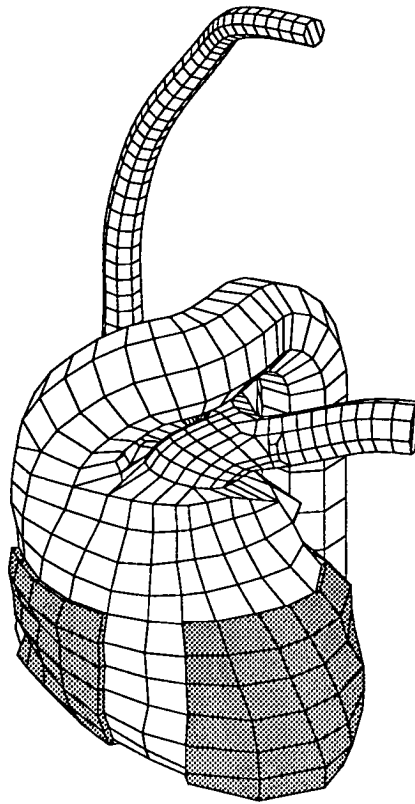


Figure 8.7: *Epicardial patch pair (configuration EPP)*

### **Epicardial Patch and Transvenous Combination (EP-T)**

Six configurations (EP-T) were constructed that used different size epicardial patch anodes with a right ventricular cathode. The aim was to reduce wasted energy by minimising the non-myocardial tissue between the anode and cathode.

Configurations EP-T 1-3 used a standard cathode and a single epicardial patch. The patches had surface areas of 67, 131 and  $220\text{cm}^2$ , and are illustrated in Figures 8.8, 8.9 and 8.11, respectively. The smallest patch only partly covered the left and right ventricles (Figure 8.8). The next covered nearly all of the ventricles though some of the right side of the heart remained uncovered (8.9). The largest patch covered the whole heart (Figure 8.10), except for the major vessels.

Configuration EP-T 4 was similar to EP-T 1 except the cathode in the right ventricle was replaced with Enguard 040-020 configured as a cathode in the

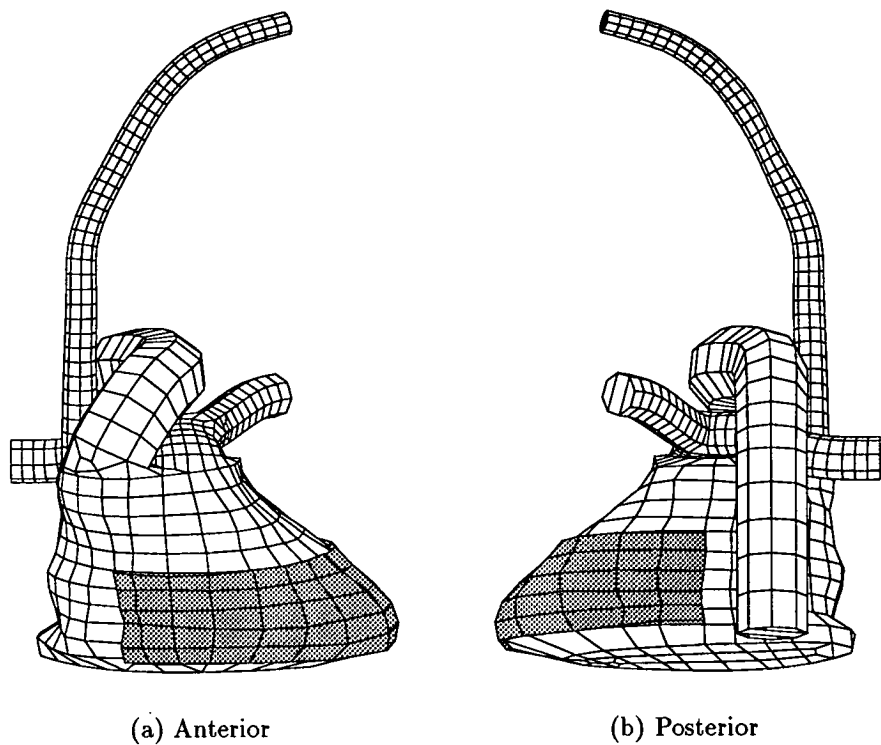


Figure 8.8:  $67\text{cm}^2$  epicardial patch (configuration EP-T 1)

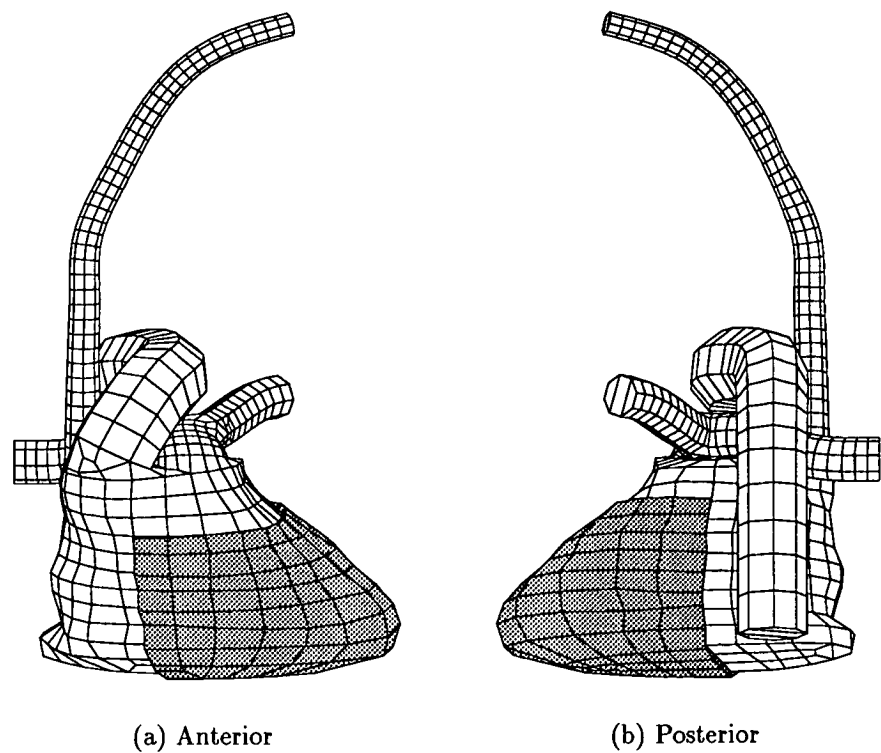


Figure 8.9:  $131\text{cm}^2$  epicardial patch (configuration EP-T 2)

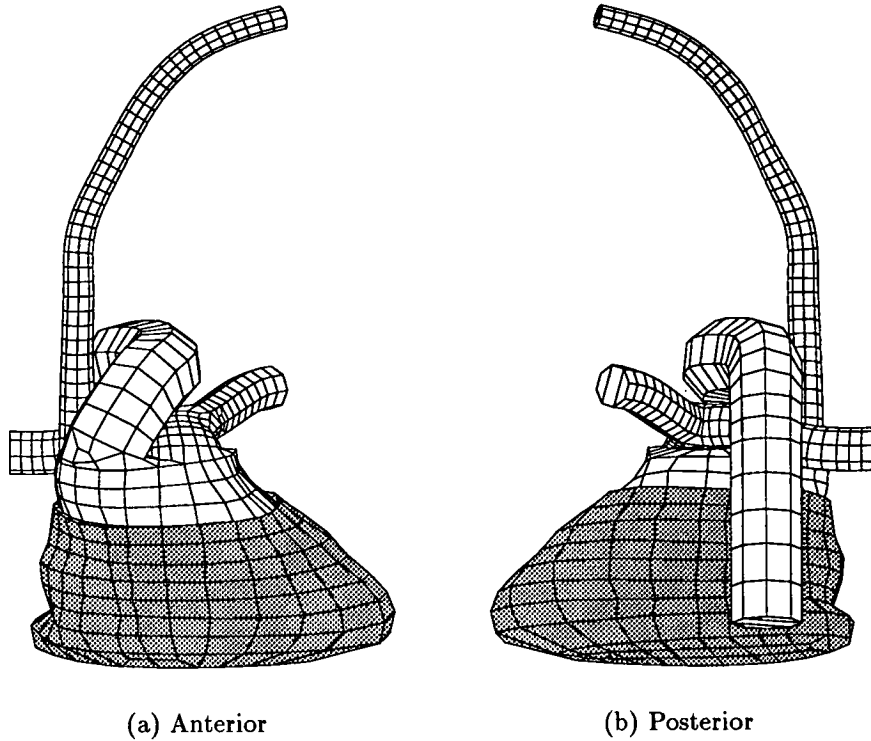


Figure 8.10:  $220\text{cm}^2$  epicardial patch (configuration EP-T 3)

superior vena cava. Configuration EP-T 5 used a  $25\text{cm}^2$  patch covering some of the left ventricle and an enlarged right ventricular electrode (Figure 8.11). The aim of using the enlarged electrode was to more effectively sandwich the myocardium between the anode and cathode. Although the enlarged ventricular electrode was modelled as solid, it was envisaged that the electrode would actually be constructed as a spring cage or spiral loop to permit normal blood flow in the ventricle. The surface of the enlarged electrode was formed by shrinking a copy of the endocardium of the right ventricle by approximately  $0.5\text{cm}$ .

### Subcutaneous Patch Location (SQ)

Four configurations (SQ) with subcutaneous patch anodes were modelled. Configuration SQ 1 consisted of an apical subcutaneous patch (Figure 8.12(a)) combined with an Enguard anode and a standard Enguard cathode. SQ 2 had

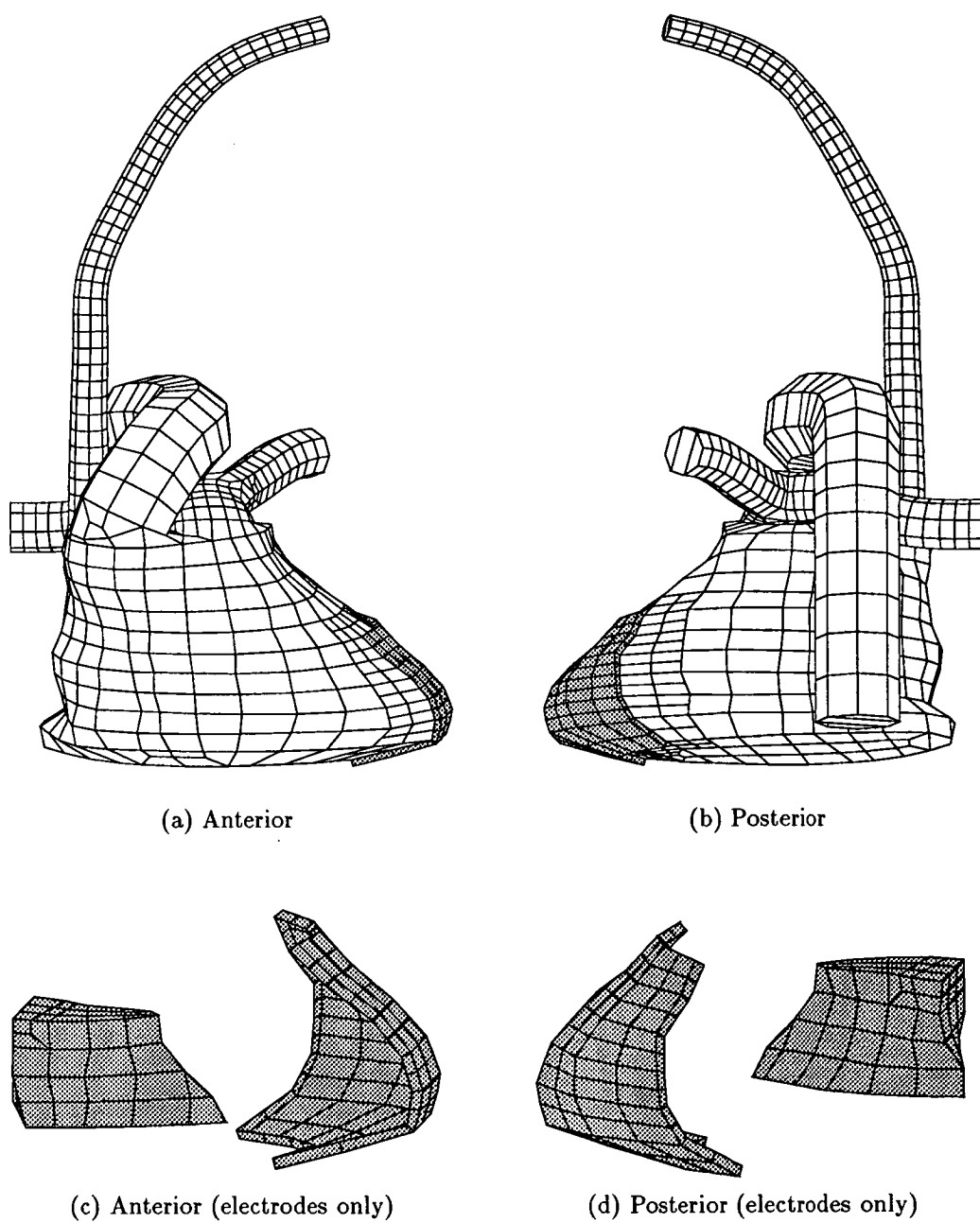


Figure 8.11:  $25\text{cm}^2$  epicardial patch and large ( $32\text{cm}^2$ ) right ventricular electrode (configuration EP-T 5)

a sub-apical subcutaneous patch (Figure 8.12(b)) with a standard Enguard anode and cathode. SQ 3 used a pectoral subcutaneous patch (Figure 8.12(c)) with a standard Enguard cathode (and was similar to an active-can arrangement). SQ 4 used a anterior subcutaneous patch located over the inferior end of the sternum (Figure 8.13(a)) with a standard Enguard cathode and a small ( $5\text{cm}^2$ ) epicardial patch on the posterior left ventricle.

### Effect of an Infarct (INF)

The effect of an infarct on defibrillator performance was also investigated. The infarct was positioned over the anterior surface of the left ventricle. Configuration INF 1 consisted of a transvenous cathode and anode (040-020). Configuration INF 2 consisted of the same endocardial pair and a subcutaneous patch. These configurations were modelled in both a healthy and an infarcted heart. A specific case of an infarct was assumed where a whole region of the infarct was deprived of blood, the muscle had all wasted, resulting in dilated cardiac myopathy. Therefore the infarct was modelled by reducing the thickness of the myocardium and allowing this region to bulge into the lung cavity (Figures 8.14 and 8.15). The infarcted region was considered electrically passive and therefore unable to sustain ventricular fibrillation. Consequently, it was unnecessary to apply defibrillation criteria to this region. It should be noted that these assumptions would not necessarily be valid for all infarcts, as often there may be spared myocardial muscle which may still be in electrical contact with the remaining myocardial muscle.

## 8.4 Performance Calculations

The performance of each configuration was ascertained by calculating the anode-cathode resistance ( $R$ ), the voltage and energy required for defibrillation and the corresponding maximum potential gradient in the ventricular

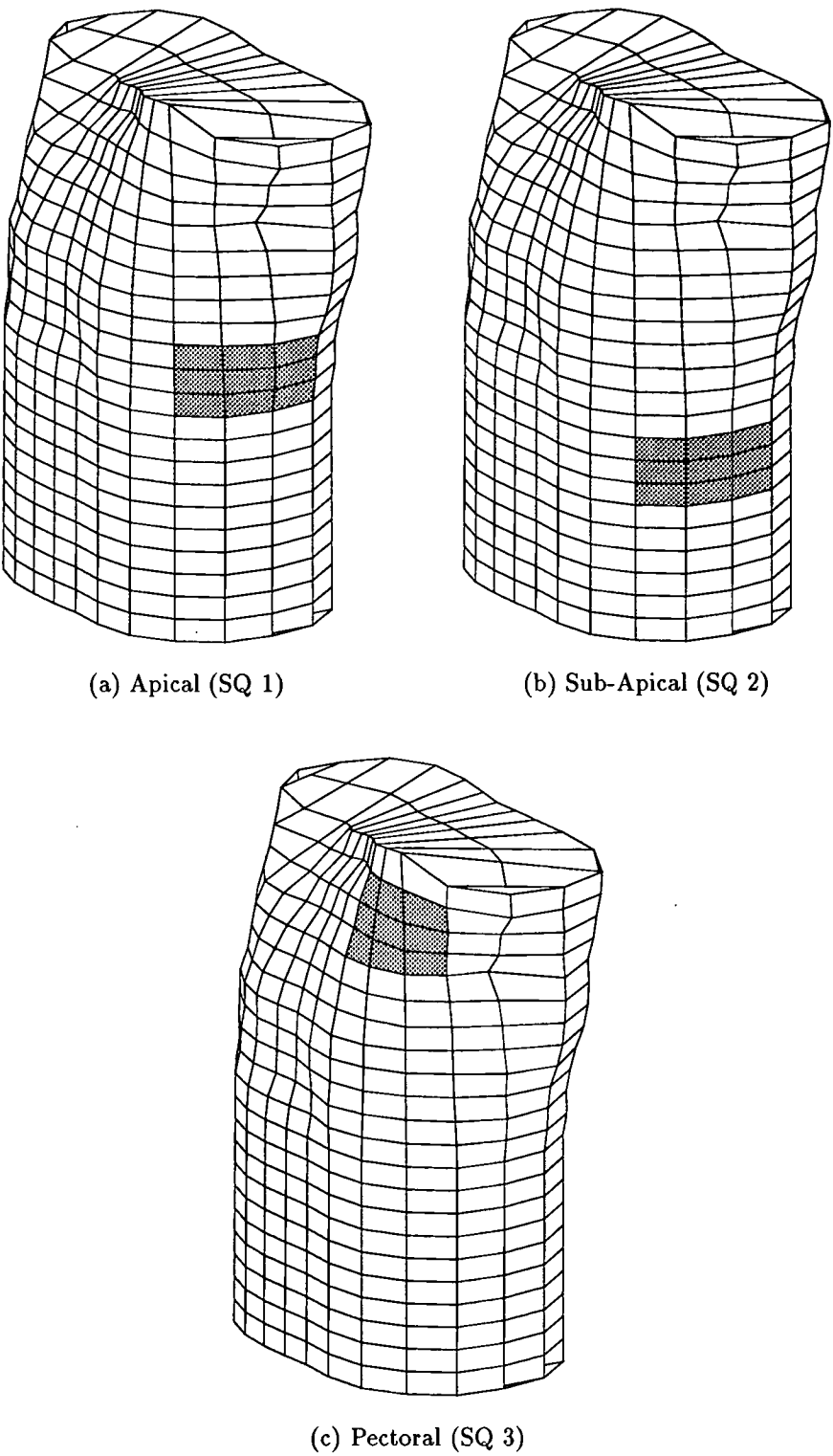
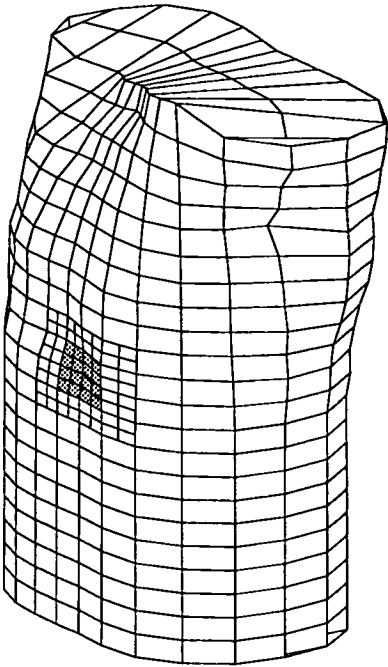
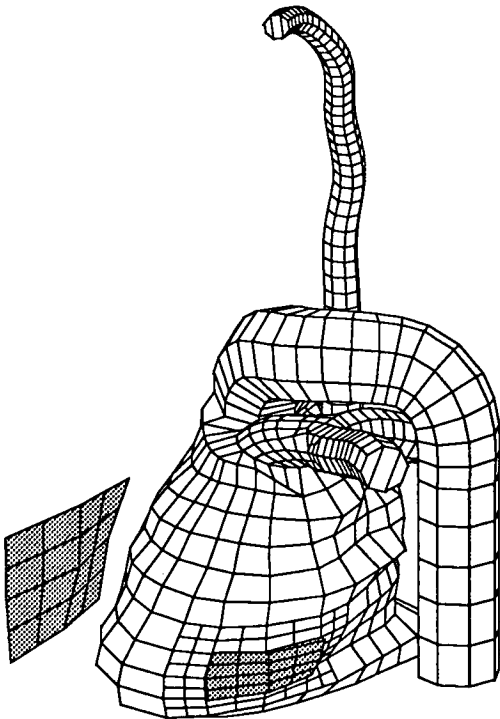


Figure 8.12: *Apical, sub-apical and pectoral subcutaneous patch locations (configuration SQ)*



(a) Subcutaneous patch relative to the torso



(b) View from left posterior side showing patches relative to the heart

Figure 8.13: *Left posterior epicardial and anterior subcutaneous patch combination (configuration SQ 4)*

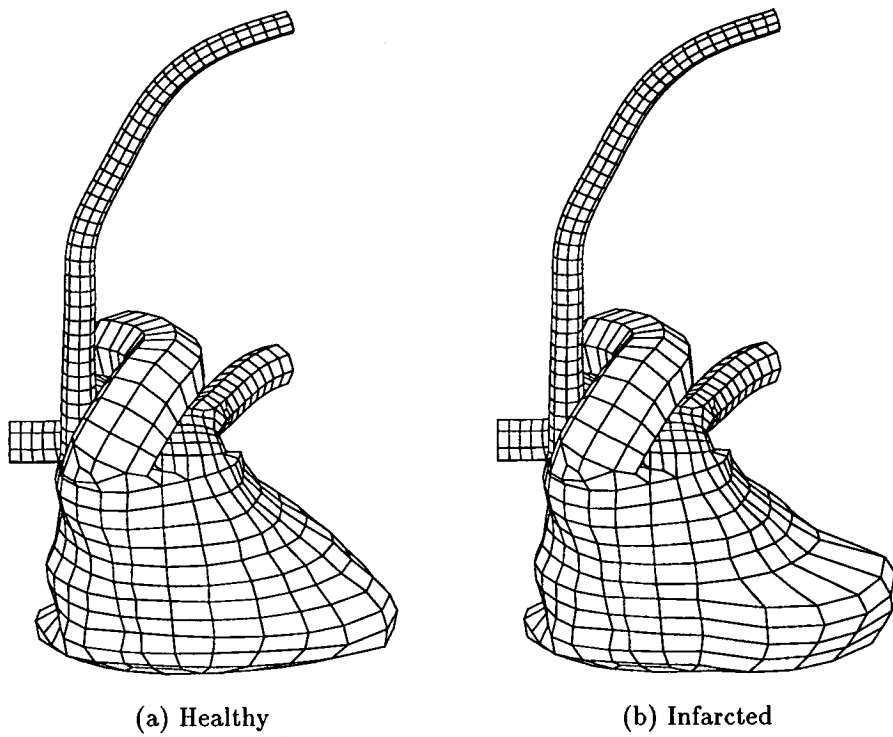


Figure 8.14: *Healthy and infarcted hearts: the infarcted heart was represented as having an infarct in the left-anterior wall of the left ventricle resulting in myopathy and bulging of the affected region into the lung cavity (configuration INF)*

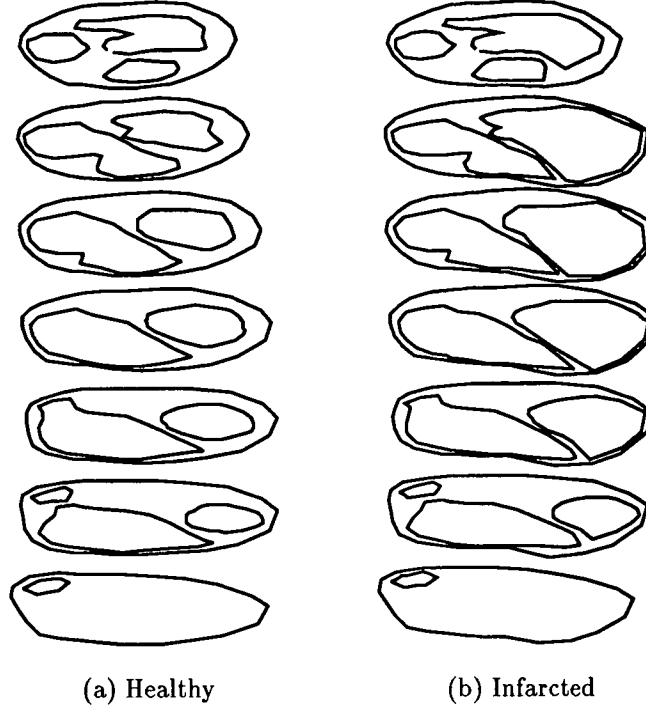


Figure 8.15: *Slices through healthy and infarcted hearts (configuration INF)*

myocardium. Voltage was the peak anode-cathode voltage ( $V_{pk}$ ) and energy was the energy dissipated ( $E$ ). The energy was calculated by assuming the applied defibrillation waveform was a monophasic truncated exponential. The waveform was assumed to be a generated from a  $7ms$  discharge from a  $150 \mu F$  capacitor ( $C$ ). The load resistance was the anode-cathode resistance calculated in the model. The anode-cathode voltage  $V_{ac}$  was therefore

$$V_{ac} = V_{pk} e^{-t/RC}, \quad (8.1)$$

where  $t$  was the time from application of the peak voltage. The energy dissipated was therefore:

$$E = \int_0^t \frac{V^2}{R} dt = \frac{V_{pk}^2 C}{2} (1 - e^{-2t/(RC)}). \quad (8.2)$$

The peak voltage was determined from the model output. It was assumed

that a minimum potential gradient of  $5V/cm$  was required in all parts of the ventricular myocardium for successful defibrillation (see Section 2.2 for discussion of this criteria).

## 8.5 Results

The results presented in this section were obtained using the boundary element human torso model with the configurations described in Section 8.3.

Results for variation in transvenous anode position and cathode length are presented in graphical form in Figures 8.16 and 8.17. Figure 8.16 plots variation in the defibrillation parameters resistance, energy and voltage against the location of the inferior end of the anode. Regions corresponding to the inferior vena cava (IVC), right atrium (RA), superior vena cava (SVC) and subclavian vein are marked on the figure, as is the location of the standard anode position. Figure 8.17 plots variation in the same defibrillation parameters against cathode length.

Some of the results from the figures and all the results from other configurations are presented in Table 8.1. The table contains details of each electrode configuration with corresponding values of resistance between the electrodes, electrode voltage, energy dissipated in the torso and the maximum voltage gradient in the ventricular myocardium. These values were calculated for defibrillation using a  $150\mu F$  capacitor and a monophasic  $7ms$  pulse with a minimum voltage gradient in the ventricular myocardium of  $5V/cm$ .

Potentials and gradients plotted on the heart surface are presented for some configurations. The plots are for an anode-cathode voltage of  $\pm 200V$ . For the potential plots, the contour interval is  $10V$ , solid contour lines are negative, broken lines are positive and the thick solid line is at a potential of zero. For the potential gradient plots, the contour interval is  $5V/cm$ , the thick solid line is at a potential gradient of  $5V/cm$ , broken contour lines are higher gradients.

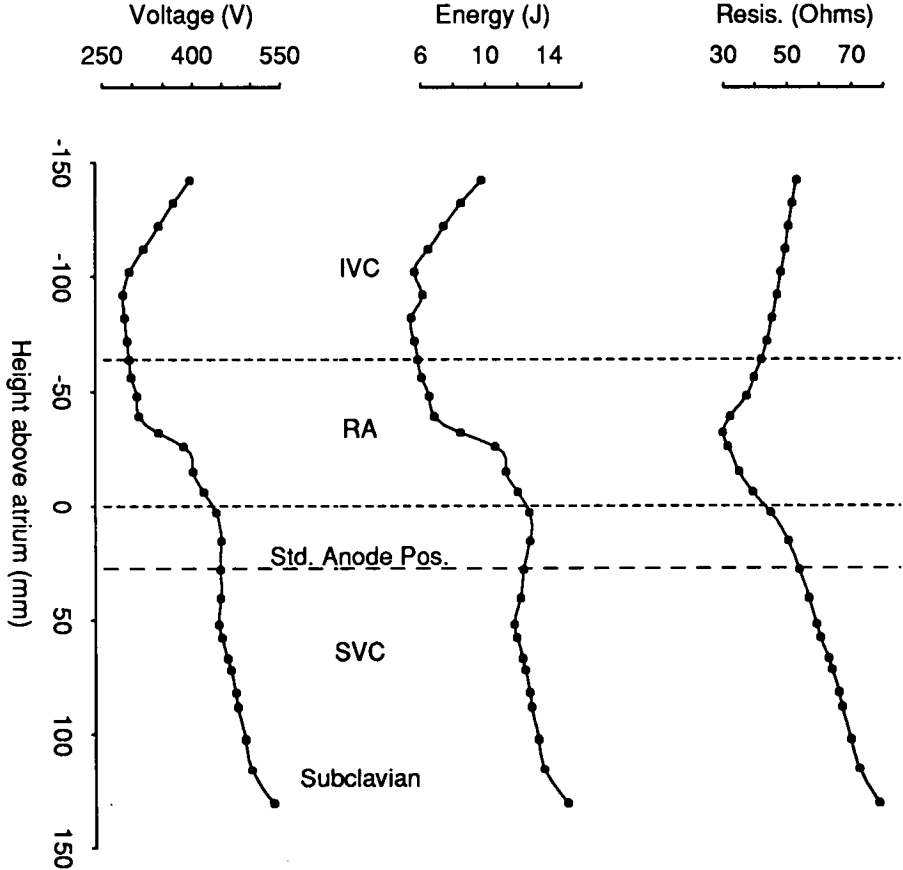


Figure 8.16: Configuration TA-VS results showing how the location of the transvenous anode affects defibrillation performance with a standard cathode in the right ventricle. Height was measured to the inferior end of the electrode braid.

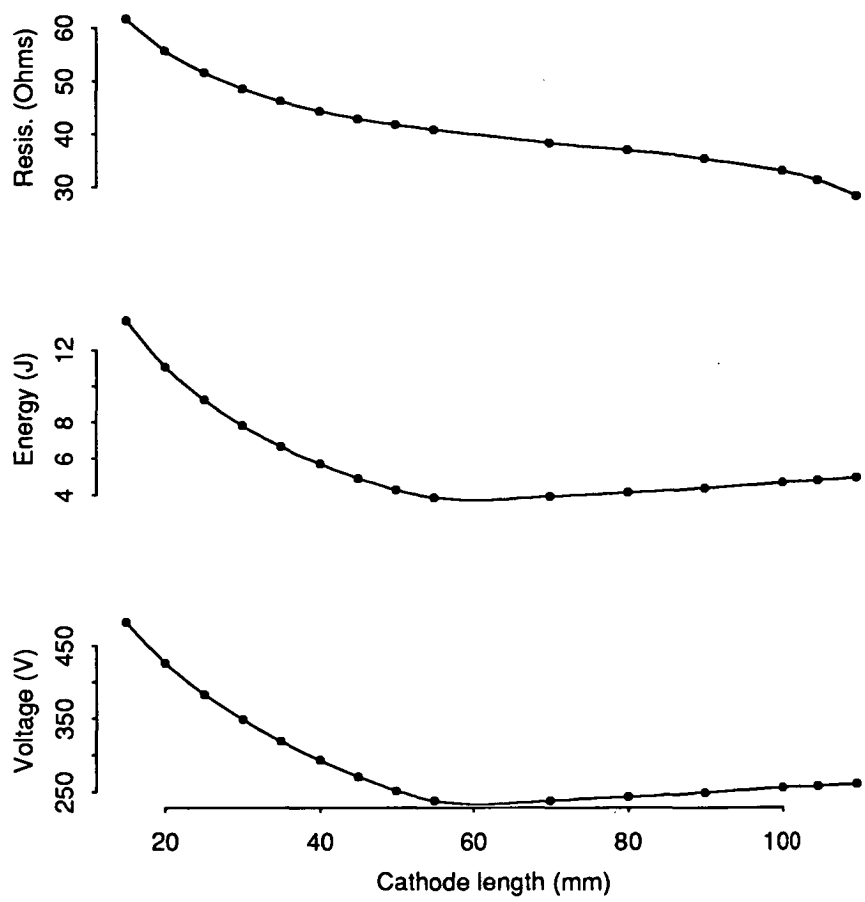


Figure 8.17: *Configuration CL results showing how the length of the cathode in the right ventricle effects defibrillation performance with a standard anode in the superior vena cava*

Config.	Ventricular	Venous	Subcutaneous (cm <sup>2</sup> )	Epicardial (cm <sup>2</sup> )	Res. (Ω)	Volt. (V)	Energy (J)	Max. Grad. (V/cm)
Transvenous anode within the venous system (complete results in Figure 8.16):								
TA-VS 1	Enguard	040-020	(Standard Configuration)		53.7	447	12.4	101.6
TA-VS 2	Enguard	040-022			66.8	476	12.8	86.2
TA-VS 3	Enguard	040-024			78.4	538	15.1	96.5
TA-VS 4	Enguard	IVC	(Optimal Configuration)		45.4	287	5.4	78.0
Transvenous anode with apical subcutaneous patch:								
TA-SQ 1	Enguard <sup>-</sup>	040-020 <sup>+</sup>	78 <sup>+</sup> (Standard plus Patch)		37.8	265	4.8	69.4
TA-SQ 2	Enguard <sup>-</sup>	040-022 <sup>+</sup>	78 <sup>+</sup>		42.7	272	4.9	66.9
TA-SQ 3	Enguard <sup>-</sup>	040-024 <sup>+</sup>	78 <sup>+</sup>		45.8	298	5.8	67.4
TA-SQ 4	Enguard <sup>-</sup>	040-020 <sup>-</sup>	78 <sup>+</sup>		52.7	437	11.9	97.5
Transvenous anode in the pulmonary artery:								
TA-PA 1	Enguard	PA			51.6	405	10.3	44.5
TA-PA 2	Enguard <sup>-</sup>	PA <sup>+</sup>	78 <sup>+</sup>		37.1	233	3.8	67.0
TA-PA 3	Enguard <sup>-</sup>	PA <sup>-</sup>	78 <sup>+</sup>		52.5	344	7.4	71.1
TA-PA 4	IVC	PA			63.3	564	18.4	108.6
Partly enlarged cathode:								
EC	Enlarged	040-020			52.7	427	11.4	94.4
Cathode length: CL—refer to Figure 8.16								
Epicardial patch pair:								
EPP			48.7 & 35.0		45.7	313	6.4	149.2
Kinst <sup>a</sup>			32 & 32		49	318	6.5	
Epicardial patch and transvenous combination:								
EP-T 1	Enguard		67		20.3	186	2.6	139.5
EP-T 2	Enguard		131		15.6	163	2.0	104.1
EP-T 3	Enguard		220		13.2	143	1.5	42.6
EP-T 4		040-020	67		50.3	323	6.6	84.1
EP-T 5	32cm <sup>2</sup>		25		46.9	451	13.2	494.4
Subcutaneous patch location:								
SQ 1	Enguard <sup>+</sup>	040-020 <sup>-</sup>	78 <sup>+</sup> (Sub-apical)		35.2	265	5.0	73.2
SQ 2	Enguard		32 (Apical)		72.8	418	9.5	79.4
SQ 3	Enguard		73 (Pectoral)		66.2	416	9.8	78.5
SQ 4	Enguard		26	5 (Anterior)	59.7	306	5.6	376.1
Effect of infarct:								
INF 1	Enguard	040-020			53.0	424	11.5	96.3
INF 2	Enguard <sup>-</sup>	040-020 <sup>+</sup>	78 <sup>+</sup>		35.9	277	5.3	83.5

<sup>a</sup>data from Kinst *et al.*[2] (energy derived assuming 150 $\mu$ F capacitor and 7ms pulse).

Table 8.1: Results of investigations for different electrode configurations in the human torso boundary element model. Results are for the resistance between the electrodes, electrode voltage, energy dissipated in the torso and the maximum voltage gradient in the ventricular myocardium. Results were calculated for defibrillation using a 150 $\mu$ F capacitor and a monophasic 7ms pulse with a minimum voltage gradient in the ventricular myocardium of 5V/cm.

The region bounded by the thick solid line is at a potential gradient lower than that required for successful defibrillation.

The epicardial potential and gradient distributions for configuration TA-VS 1 are presented in Figures 8.18 and 8.19, respectively, for TA-VS 3 in Figures 8.20 and 8.21, for TA-VS 4 in Figures 8.22 and 8.23, for TA-PA 1 in Figures 8.26 and 8.27, for TA-SQ 1 in Figures 8.24 and 8.25, for EPP in Figures 8.28 and 8.29 and for EP-T 1 in Figures 8.30 and 8.31,

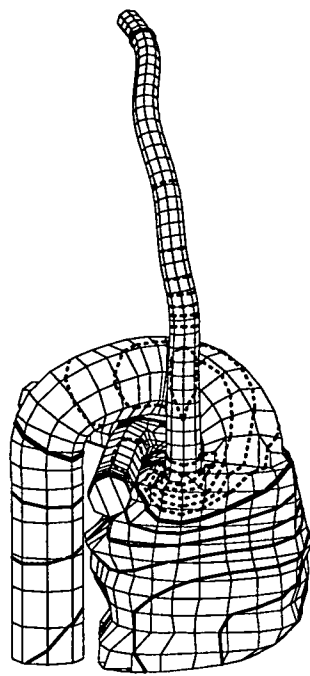
Plates 4-6 also show results. Plate 4 is for the standard configuration (TA-VS 1) and shows the potential and the potential gradient on a section through the ventricles. Plate 5 is for the same configuration and is a plot of potential gradient over the heart surface. Plate 6 is for the standard configuration plus apical subcutaneous patch (TA-SQ 1) and shows the potential gradient on a section through the torso and through the ventricles.

## 8.6 Discussion

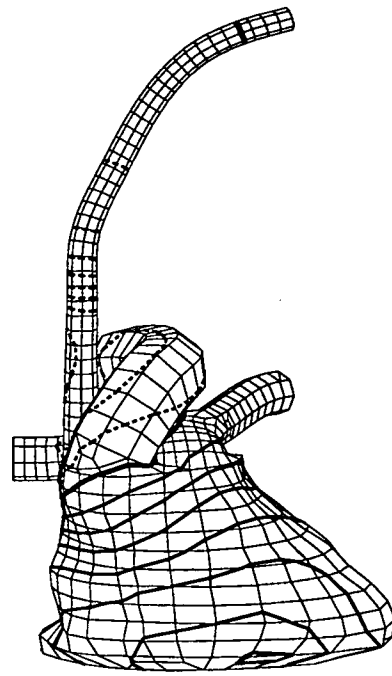
In discussion of the results, a standard electrode configuration will be used as a bench-mark for the purpose of making comparisons between configurations. The standard configuration configuration used was TA-VS 1, which consisted of the standard Enguard cathode in the right ventricle and the standard Enguard anode in the superior vena cava. Also, it is reiterated that, ideally, the maximum voltage gradient should be less than approximately  $80V/cm$  to help avoid interference to the electrical response of the myocardium (see Section 2.2).

### Transvenous Anode Within the Venous System (TA-VS)

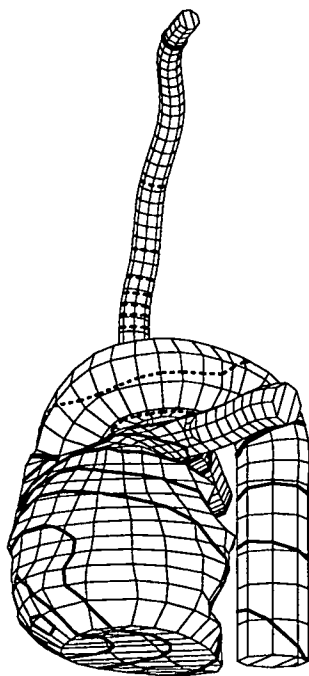
The TA-VS configuration used a cathode in the right ventricle with an anode in the venous system. The first TA-VS configuration to consider is the standard configuration. The minimum potential gradient for this configuration was on



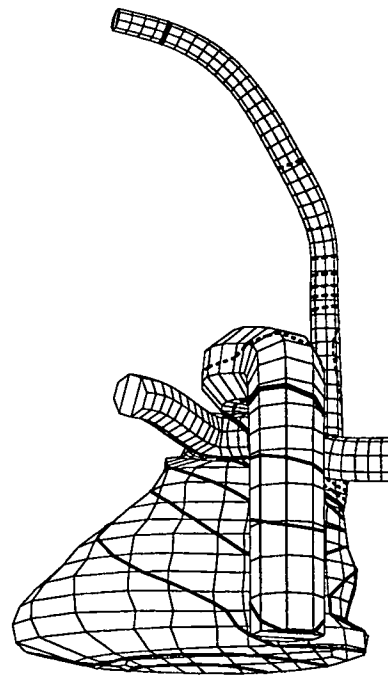
(a) Right lateral



(b) Anterior



(c) Left lateral



(d) Posterior

Figure 8.18: *Potential distribution, cathode & anode 040-020 (TA-VS 1)*

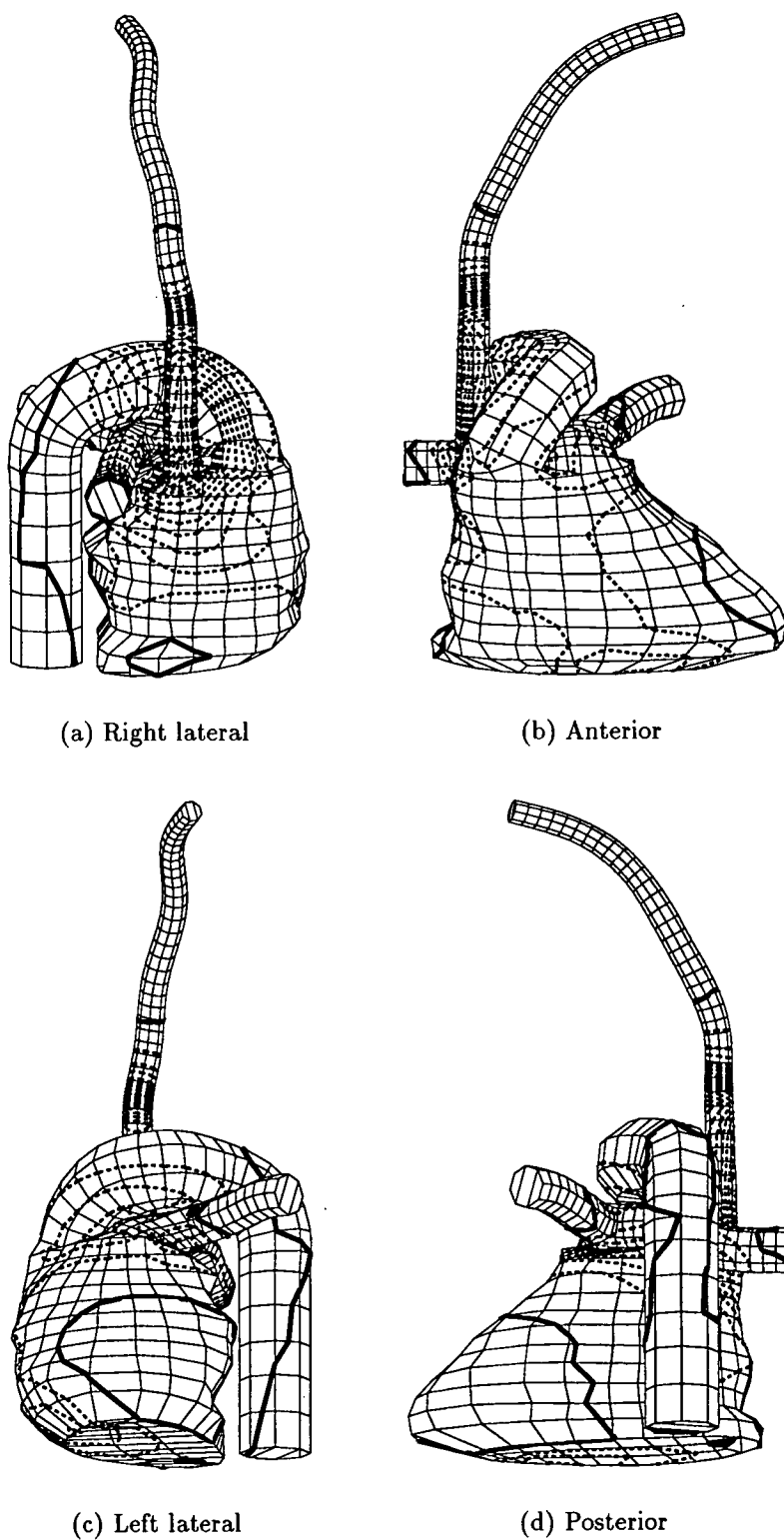
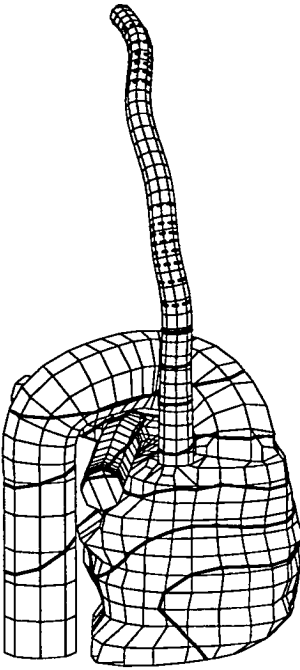
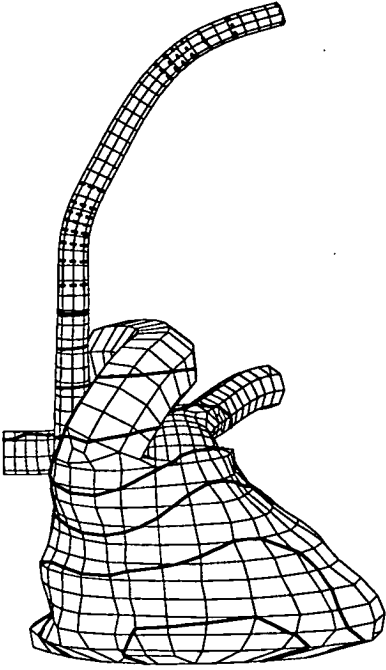


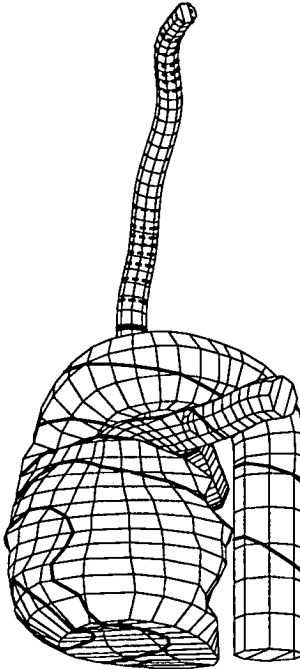
Figure 8.19: *Potential gradient distribution, cathode & anode 040-020 (TA-VS 1)*



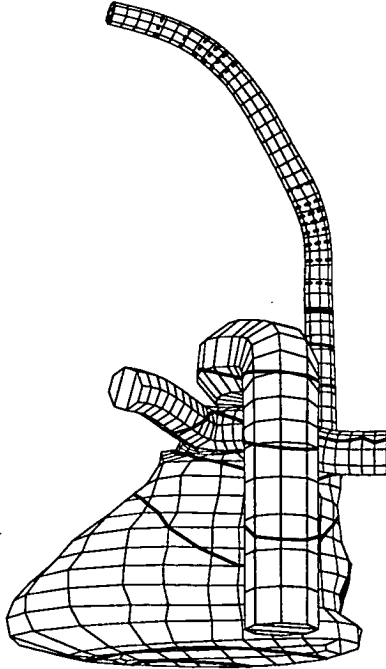
(a) Right lateral



(b) Anterior

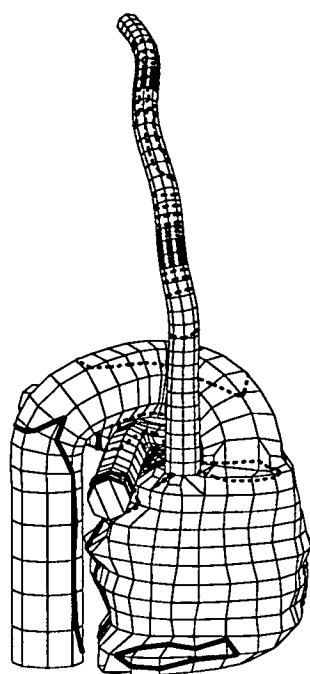


(c) Left lateral

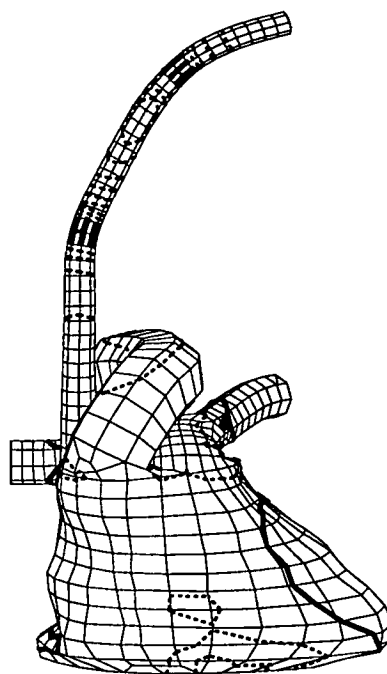


(d) Posterior

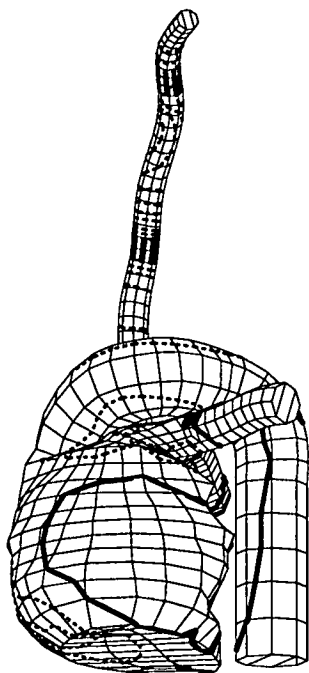
Figure 8.20: *Potential distribution, cathode & anode 040-024 (TA-VS 3)*



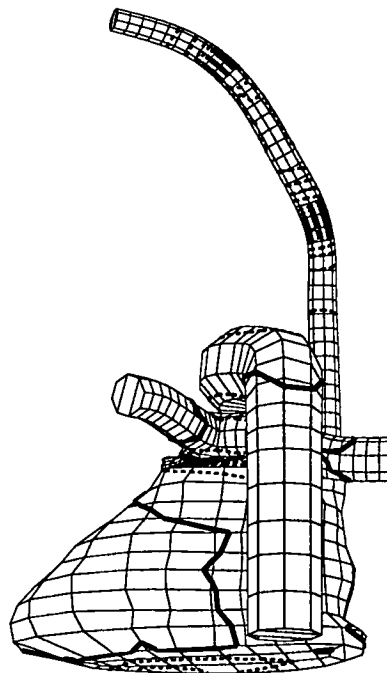
(a) Right lateral



(b) Anterior



(c) Left lateral



(d) Posterior

Figure 8.21: *Potential gradient distribution, cathode & anode 040-024 (TA-VS 3)*

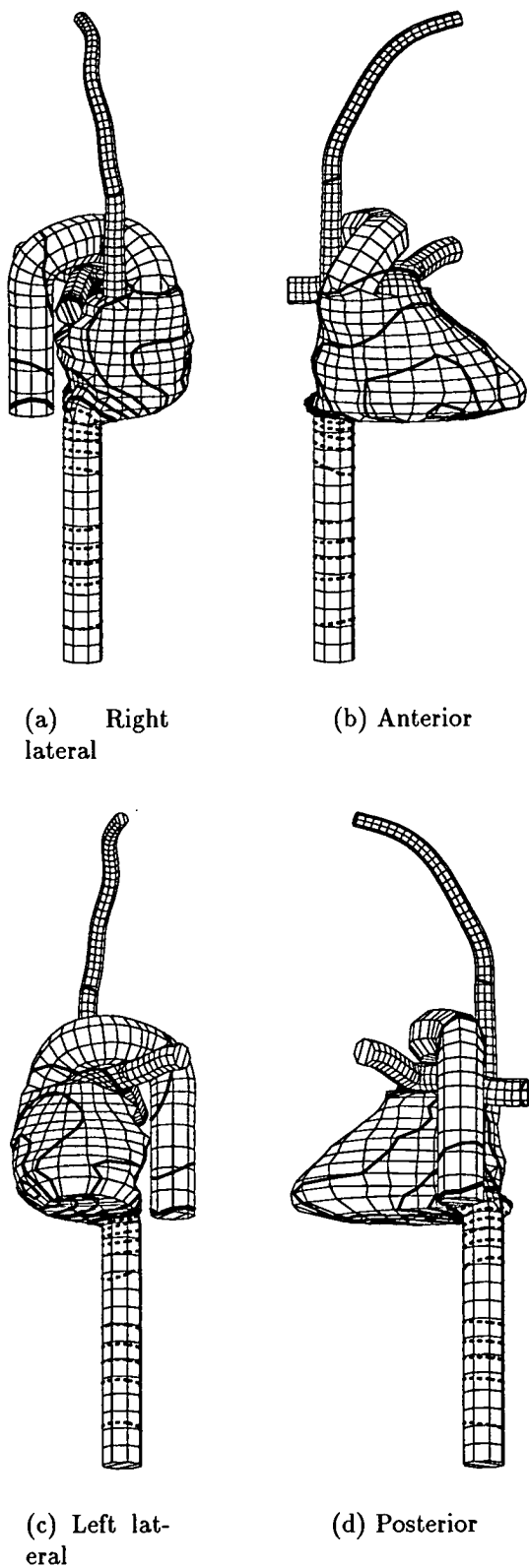


Figure 8.22: *Potential distribution, cathode & optimal anode in inferior vena cava (TA-VS 4)*

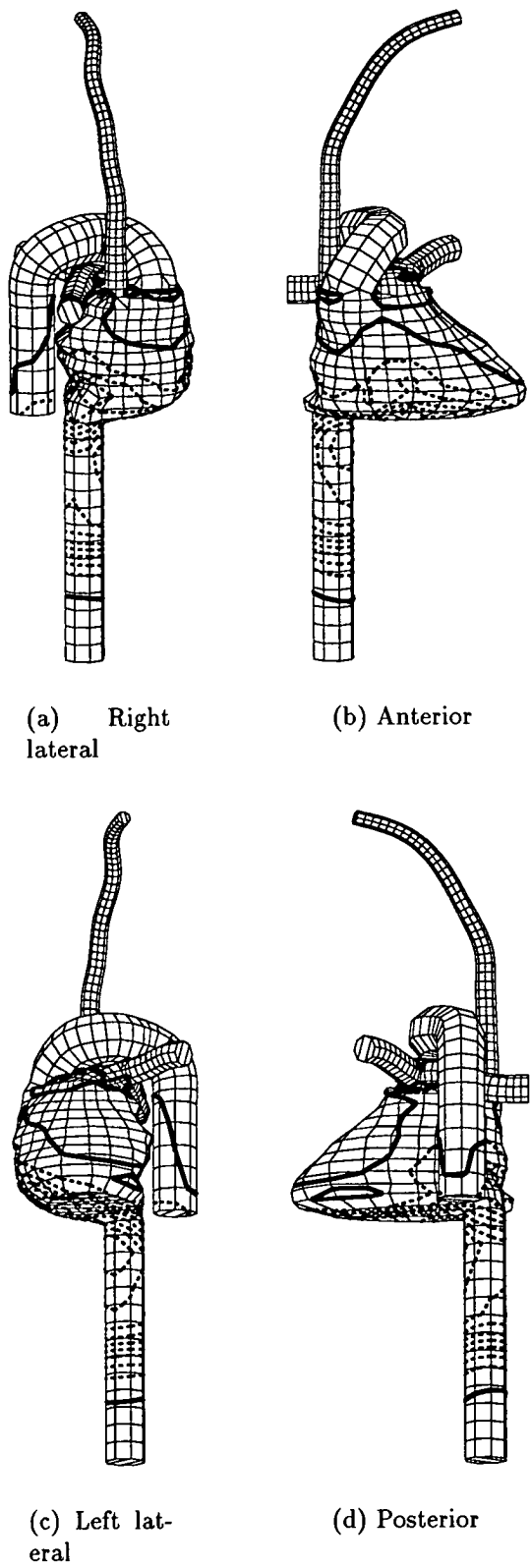


Figure 8.23: *Potential gradient distribution, cathode & optimal anode in inferior vena cava (TA-VS 4)*

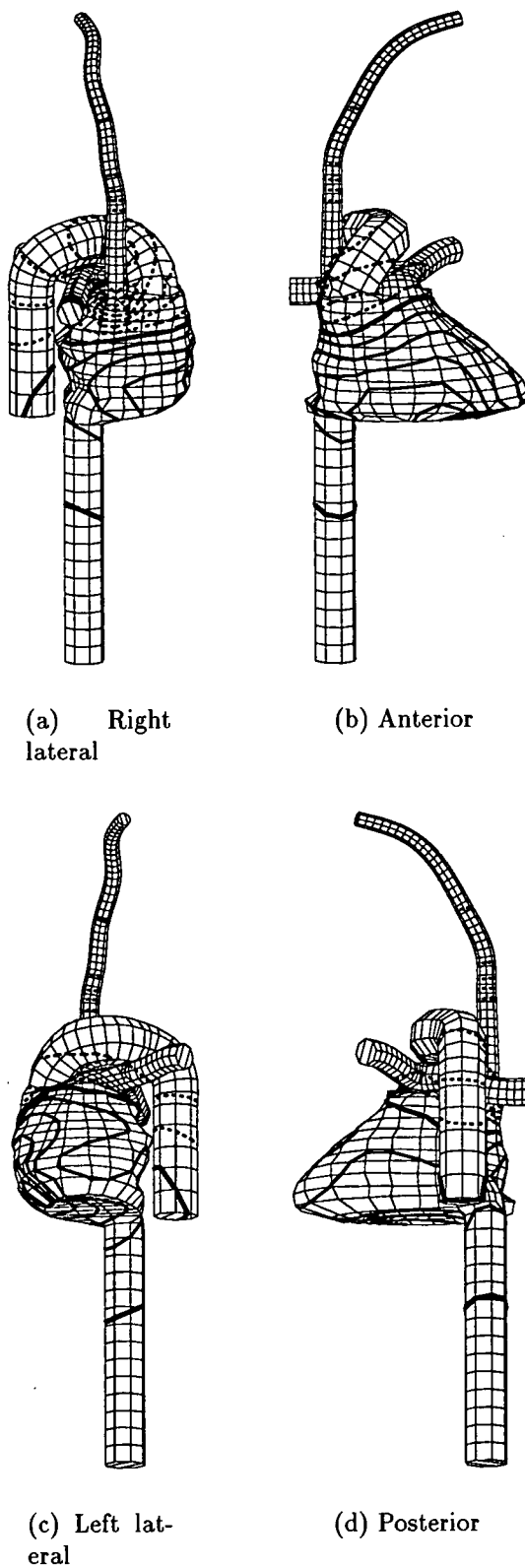


Figure 8.24: *Potential distribution, cathode, anode 040-020 and apical subcutaneous patch (TA-SQ 1)*

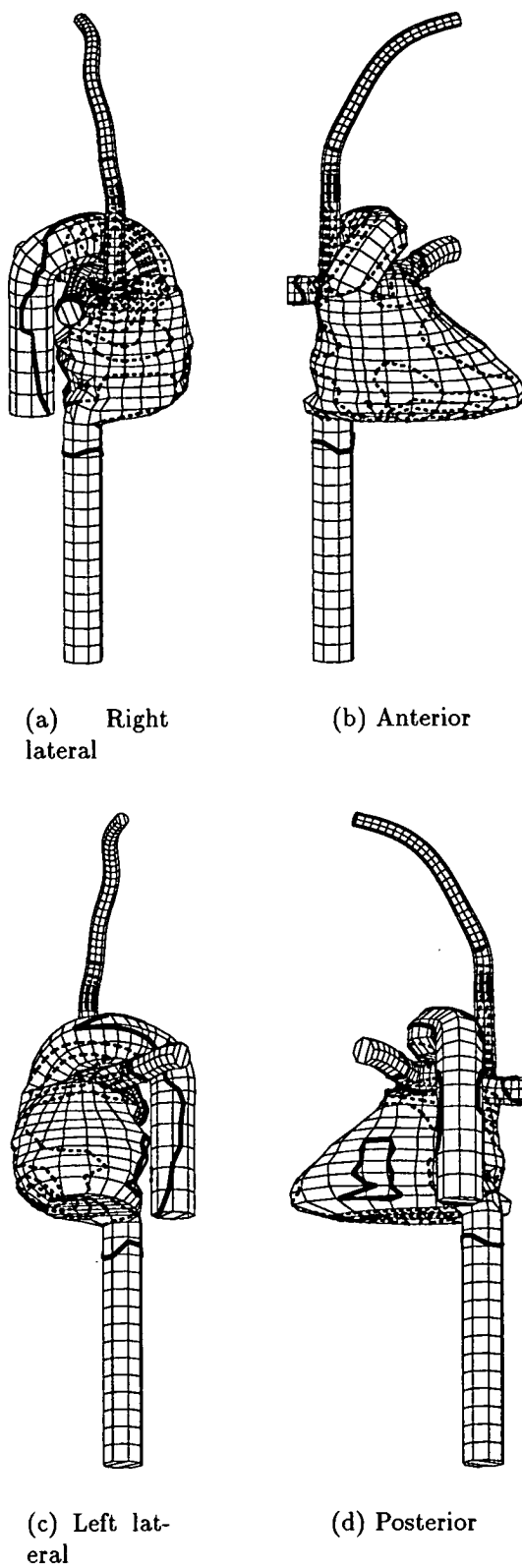
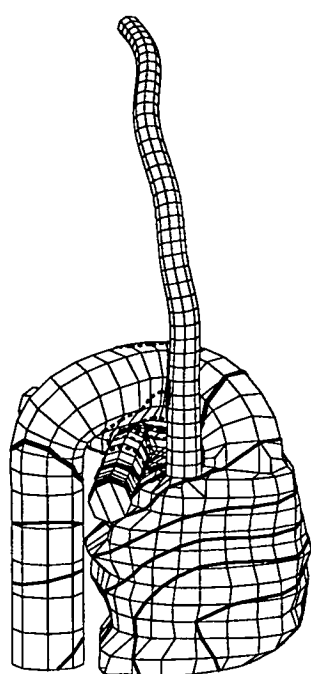
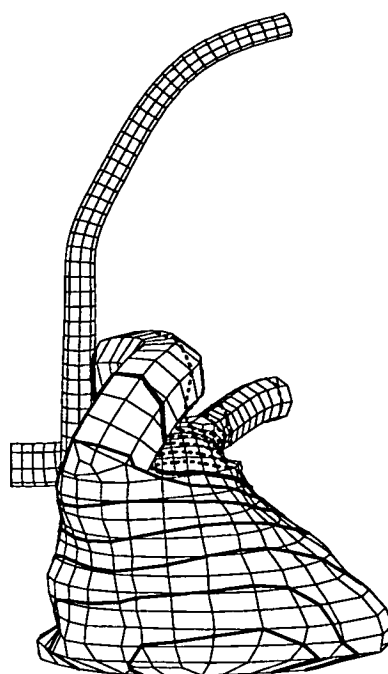


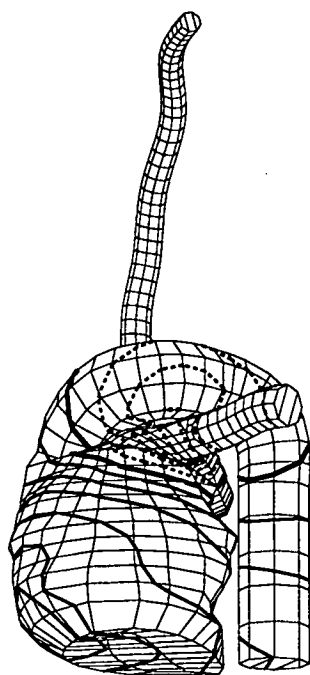
Figure 8.25: *Potential gradient distribution, cathode, anode 040-020 and apical subcutaneous patch (TA-SQ 1)*



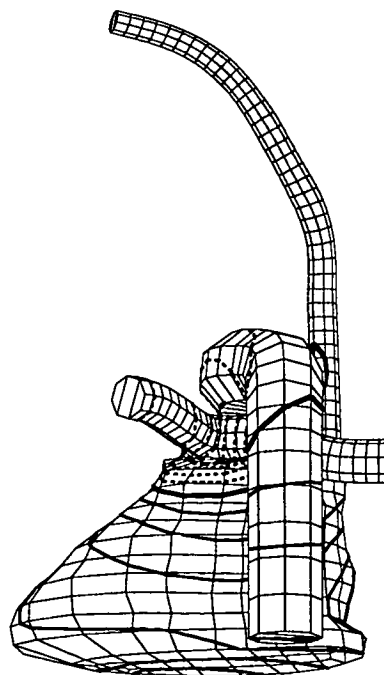
(a) Right lateral



(b) Anterior



(c) Left lateral



(d) Posterior

Figure 8.26: *Potential distribution, transvenous cathode and pulmonary artery anode (TA-PA 1)*

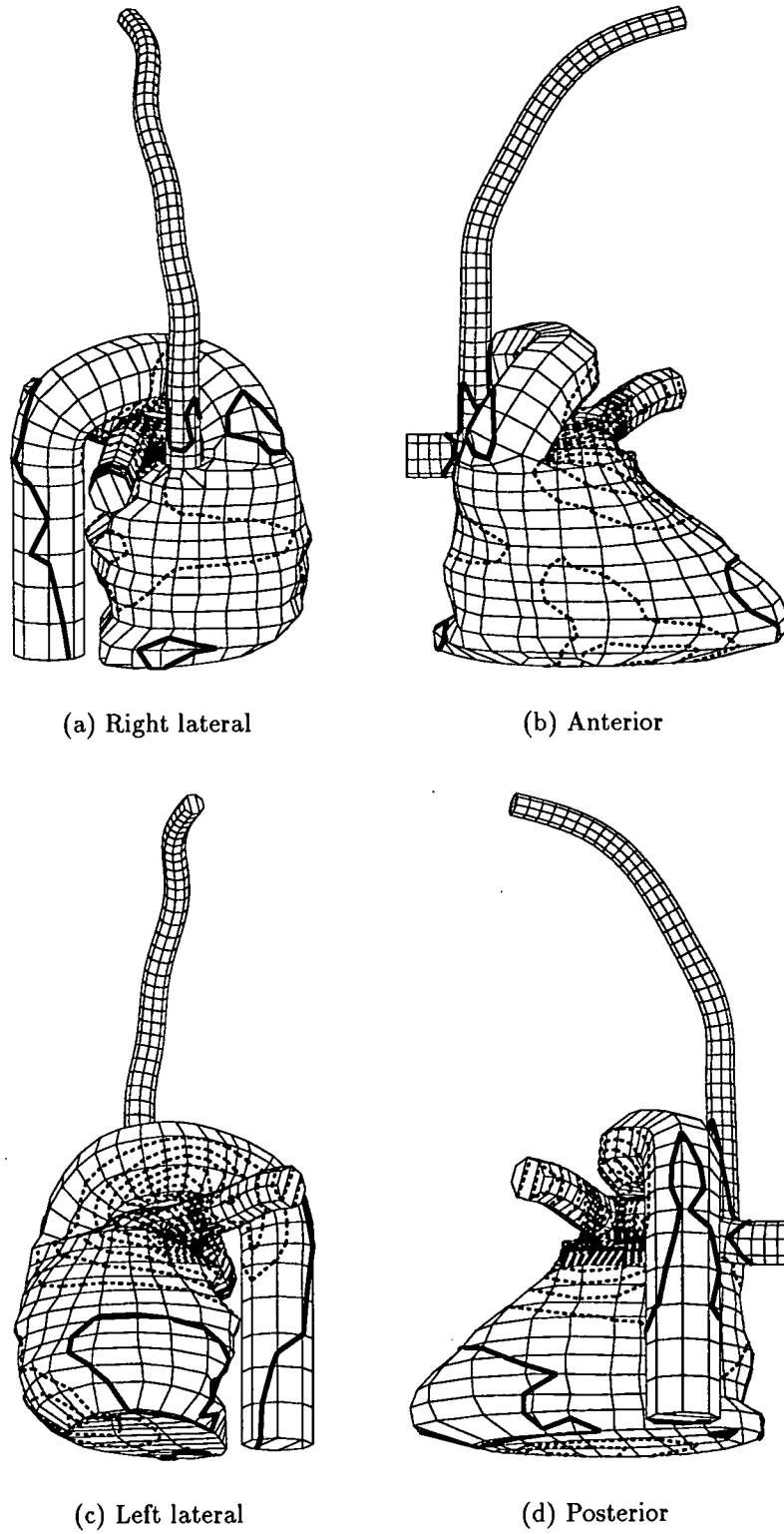
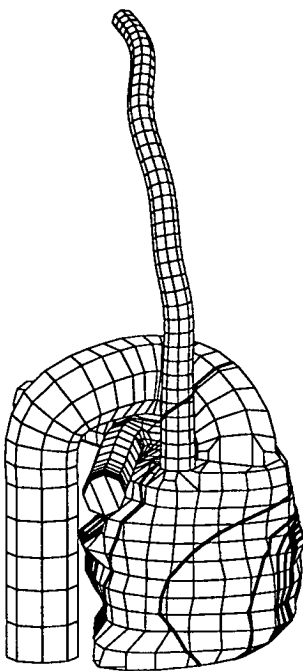
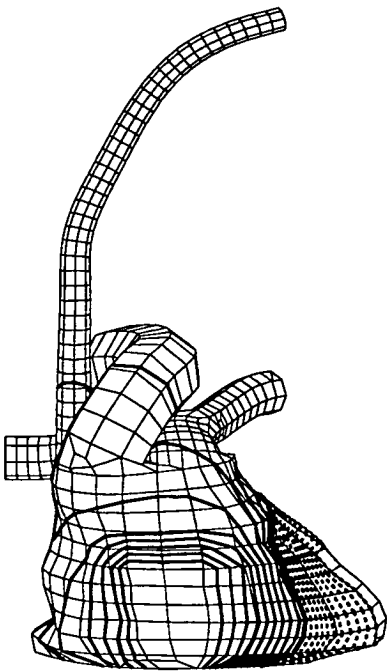


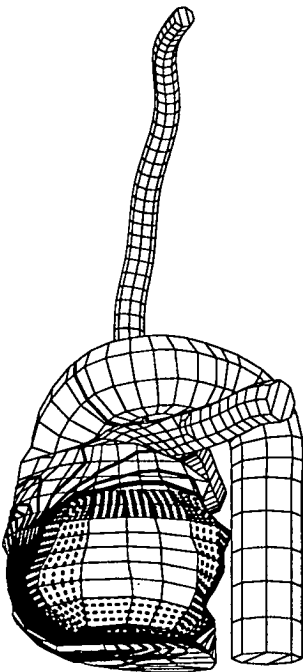
Figure 8.27: *Potential gradient distribution, transvenous cathode and pulmonary artery anode (TA-PA 1)*



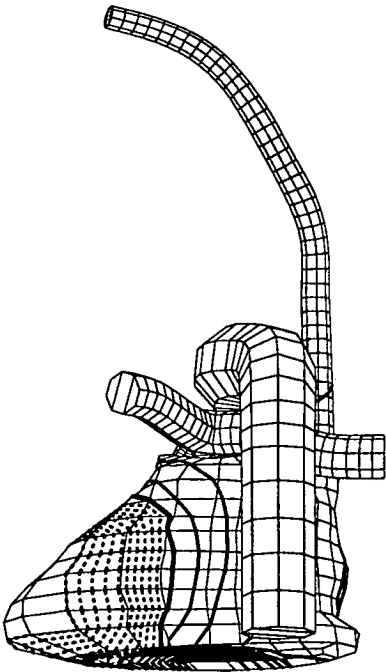
(a) Right lateral



(b) Anterior



(c) Left lateral



(d) Posterior

Figure 8.28: *Potential distribution, epicardial patch pair (EPP)*

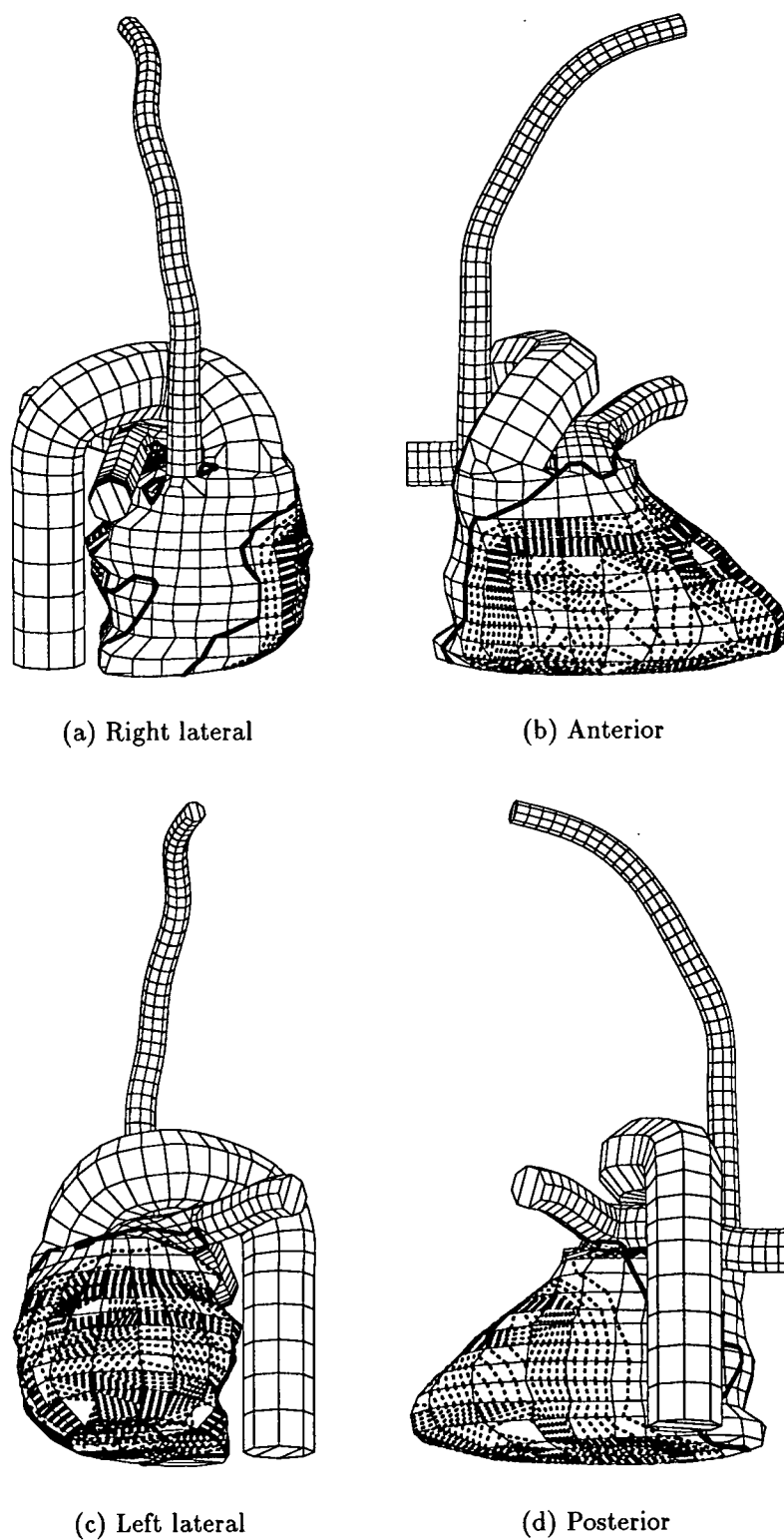


Figure 8.29: *Potential gradient distribution, epicardial patch pair (EPP)*

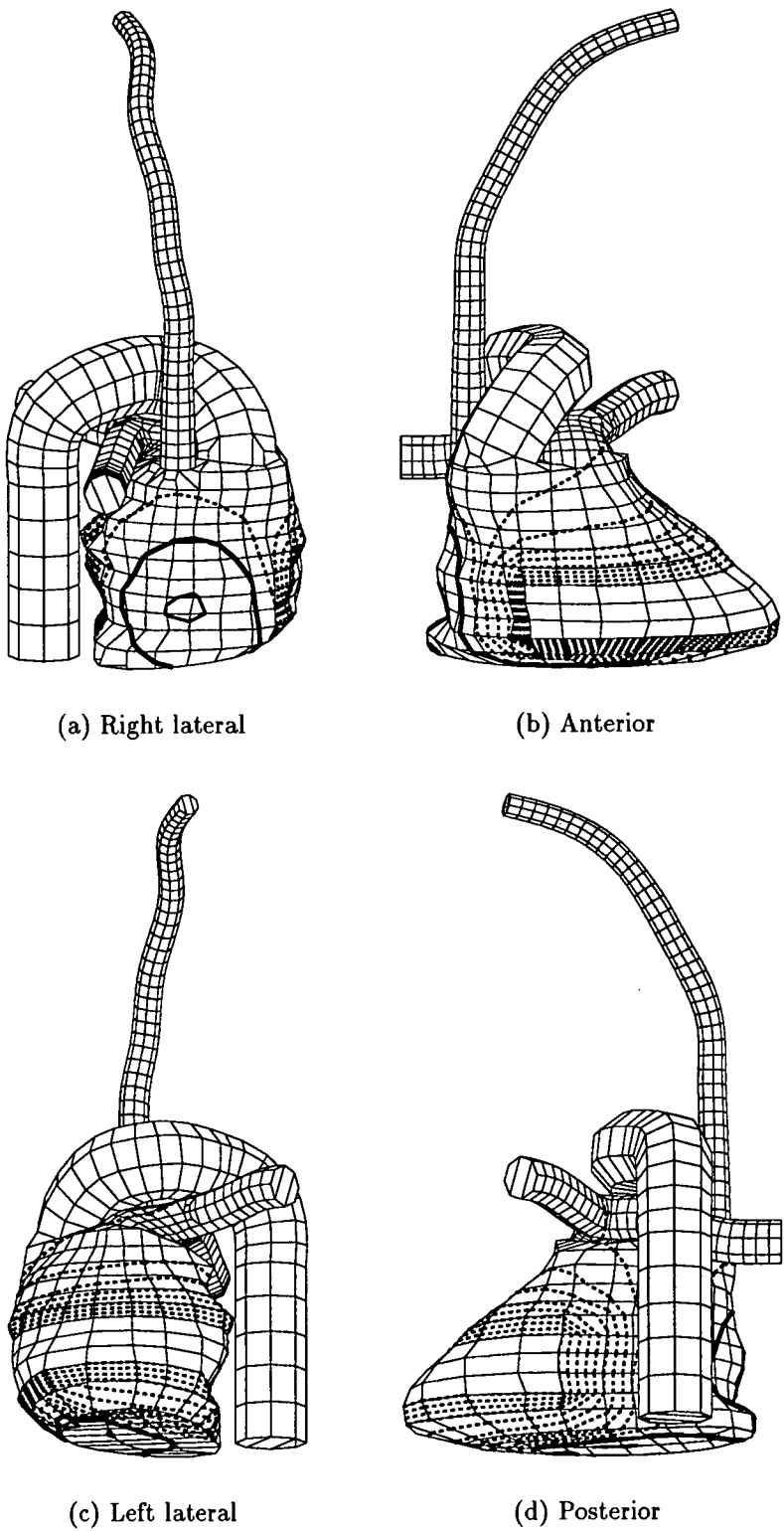


Figure 8.30: *Potential distribution, transvenous cathode and epicardial patch anode (EP-T 1)*

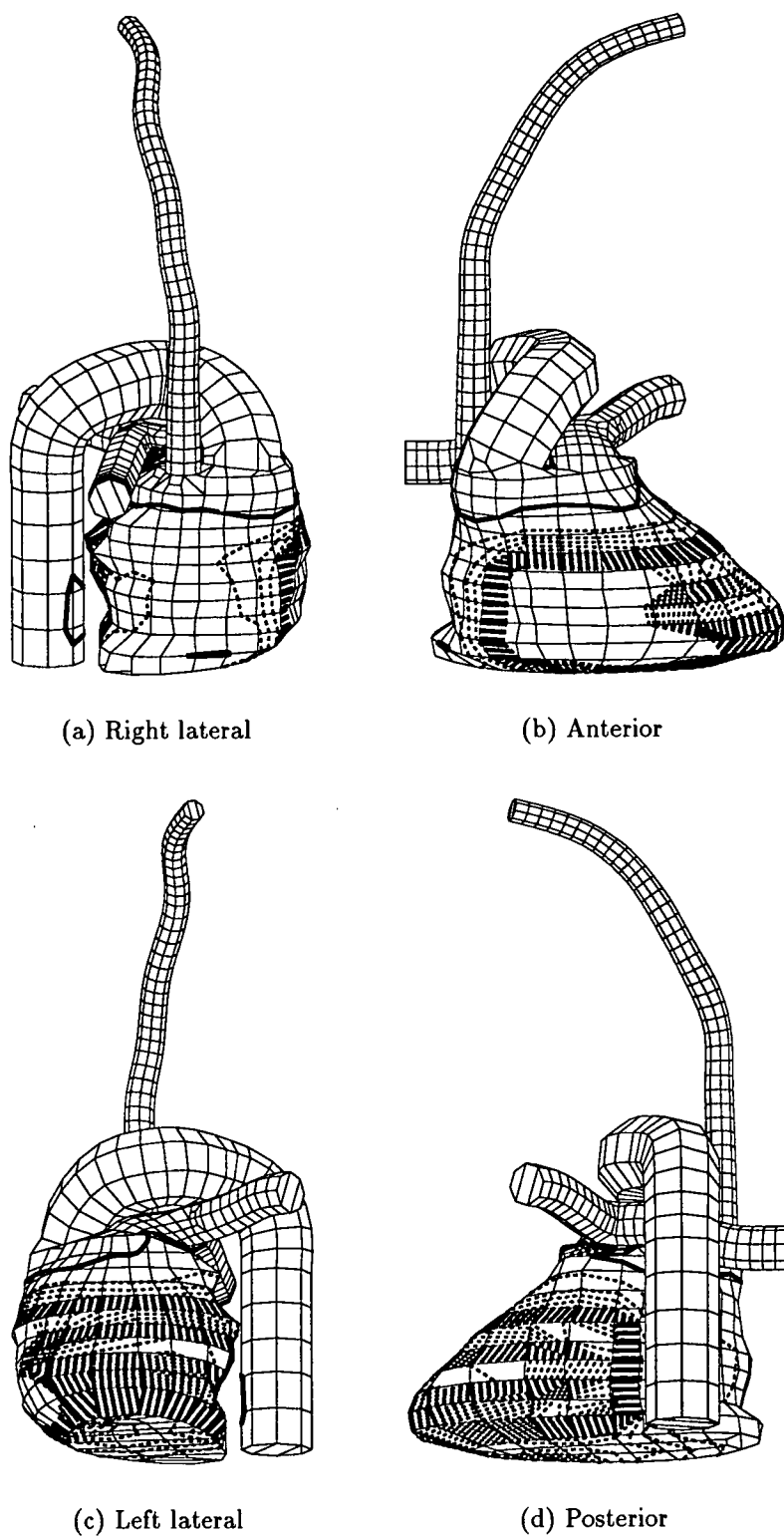


Figure 8.31: *Potential gradient distribution, transvenous cathode and epicardial patch anode (EP-T 1)*

the left lateral wall of the left ventricle within the low-gradient region bounded by the thick black line in Figure 8.19.

The performance of other TA-VS configurations can be compared to the standard configuration. In general, voltage and energy increased for configurations with the anode higher in the superior vena cava or in the subclavian vein. Configuration TA-VS 3, for example, had the anode entering the subclavian vein. Comparing results for this configuration (Figures 8.20 and 8.21) with those for the standard configuration (Figures 8.18 and 8.19), the isopotential lines are further apart and the low-gradient region was much bigger and, although not ascertainable from the figure, had a smaller minimum value.

Near the standard anode position, though, the trend for increasing voltage and energy was interrupted by a local minimum. This coincided with the anode being adjacent to the aorta, which provided a low-resistance pathway for current flow to the left side of the heart.

For the anode positioned below the standard position, the voltage and energy reduced, and this trend continued until the anode had passed through the right atrium and well into the inferior vena cava. It was not until the anode was well inferior of the heart that the voltage and energy again increased.

From observation of Figure 8.16, the best transvenous anode position was with the anode in the inferior vena cava. For this configuration, the region of low potential gradient was on the upper region of the heart opposite the electrodes (Figure 8.23). Raising the electrode voltage (from 200V) a relatively small amount was sufficient to move this region off the heart completely. In this position, the voltage and energy were reduced by 35% and 55%, respectively, compared to the results using the standard anode position. Significantly, this improvement would be achieved simply by using a longer lead to allow positioning of the the anode in the inferior vena cava. Also, the maximum voltage gradient was acceptable and was 23% lower than for the standard configuration.

**Transvenous Anode with Subcutaneous Patch (TA-SQ)**

The addition of a subcutaneous patch improved the performance of transvenous configurations with an anode in the superior vena cava. Reductions in voltage, energy and maximum gradient of up to 41%, 61% and 34%, respectively, were achieved compared to the standard configuration. A significant lowering of voltage and energy was achieved because the patch increased the strength of the field in the left ventricular wall (Figures 8.24 and 8.25), which was formerly the lowest gradient region in the ventricular myocardium. These configurations were relatively insensitive to the position of the anode. The decrease in resistance associated with the addition of the subcutaneous patch was due to the improved positioning and increased area of the anodal electrodes. The decrease in maximum gradient was due primarily to the decrease in electrode voltage. The use of reversed polarity on the transvenous anode (TA-SQ 4) resulted in much worse performance, though still marginally better than the standard configuration. The added complexity of the third electrode was a disadvantage compared to the standard configuration.

**Transvenous Anode in the Pulmonary Artery (TA-PA)**

Location of the anode in the pulmonary artery (TA-PA 1) decreased the required voltage and energy by 9% and 17%, respectively, compared to the standard configuration. This improvement resulted from the anode in the pulmonary artery being better located with respect to the left ventricle than for the standard configuration. This increased the voltage gradient throughout the left ventricle resulting in a smaller sub-threshold region (Figures 8.26 and 8.27). A significant advantage of this configuration was the low value of maximum gradient, which was 56% less than for the standard configuration.

With a subcutaneous patch added to the configuration (TA-PA 2), an improvement in voltage and energy of 12% and 21%, respectively, was achieved

compared to the standard configuration with the same patch (TA-SQ 1). This significant improvement was again due to the improved field strength in the left ventricle. The maximum gradient was similar to that obtained using the standard configuration.

### **Partly Enlarged Cathode (EC)**

The partly enlarged cathode (EC) decreased defibrillation voltage, energy and maximum gradient by 4.5%, 8% and 7%, respectively, compared to the standard configuration. Although the increase in effectiveness was relatively small, it was achieved with only minor modification to the shape of one electrode.

### **Cathode Length (CL)**

The results from varying the length of the cathode, from Figure 8.17, indicate that there is an optimum length of approximately 60mm where both the voltage and energy are at a minimum. With a longer cathode, more current is shunted between the electrodes, reducing their efficiency. With a shorter cathode, the voltage gradient is high near the cathode, again reducing the efficiency. For short cathodes, the field is improved if the cathode is moved as far as possible towards the apex of the right ventricle, rather than remaining near the middle of the ventricle. However, this results in high potential gradients in the myocardium near the electrode.

### **Epicardial Patch Pair (EPP)**

With a pair of epicardial patches, the potential and potential gradient fields (Figures 8.28 and 8.29) were very different to the transvenous configurations. Compared to the standard configuration, voltage and energy were reduced by 30% and 48%, respectively. The significant reductions may be attributed in part to lower resistance and an improved distribution of the electric field. However, the maximum gradient increased by 47%. Results for this config-

uration were in excellent agreement with those obtained from the model of Kinst *et al.*[2] (refer to Table 8.1). Agreement between the models was within 2% for both voltage and energy. This configuration is disadvantaged by the requirement for major surgery for patch implantation.

### **Epicardial Patch and Transvenous Combination (EP-T)**

The combination of an epicardial patch with a transvenous electrode (EP-T) was particularly effective. For the first three configurations, a strong field was achieved even with the smallest patch (Figures 8.30 and 8.31). Reductions in voltage and energy of up to 59% and 79%, respectively, were achieved compared to the standard transvenous configuration. The maximum gradient increased by 37% to an unacceptably high value for the smallest patch but decreased by 85% for the largest.

The use of the standard anode with the small patch (EP-T 4) gave acceptable results. This contrasted to the poor results, especially the high maximum gradient, from use of a large right ventricular electrode with the small epicardial patch (EP-T 5).

The best results for this configuration were for a cathode in the right ventricle and a large epicardial patch anode (EP-T 3). This concentrated the field in the heart. An advantage of this configuration was the use of only one epicardial patch. The exact positioning of the patch was not critical, unlike with a pair of patches where care must be taken to ensure correct spacing between the edges of the patches. Use of only one patch may assist implantation of the system without thoracotomy.

Care is taken to avoid covering the main coronary arteries when implanting epicardial patches, due to complications that can arise if the arteries are covered by the patches. This issue was not addressed when considering the epicardial configurations. However, patches shown as solid and continuous may instead be constructed in a piecewise fashion, thereby avoiding covering

the arteries.

### **Subcutaneous Patch Location (SQ)**

The use of a sub-apical (SQ 1), rather than an apical (TA-SQ 1), subcutaneous patch resulted in unchanged voltage, a marginal increase in energy and maximum gradient and a small reduction in resistance. This indicated that the exact position of the apical patch has little effect on performance.

In contrast, use of a smaller patch with only a cathode (SQ 2) resulted in the voltage and energy increasing by 58% and 98%, respectively, compared to the standard transvenous plus patch configuration (TA-SQ 1), illustrating the importance of the transvenous anode. Compared to the standard transvenous-only configuration (TA-VS 1), voltage and energy reduced by 6.5% and 26%, respectively, indicating a small improvement in performance for electrodes placed either side of the left ventricle rather than in the right ventricle and the superior vena cava.

Use of a pectoral patch with only a cathode (SQ 3), gave similar results to SQ 2. Increased resistance, and consequently increased voltage and energy, may have been expected compared to the standard configuration because of the increased separation of cathode and anode. However, this effect was counteracted by the large area of the pectoral patch relative to the standard transvenous anode.

Use of an anterior subcutaneous and a small epicardial patch with a standard cathode (configuration SQ 4) resulted in generally improved performance over the two-electrode apical and pectoral configurations (SQ 1 and 2), but worse performance than the standard three-electrode configuration (TA-SQ 1). The epicardial patch was too small to generate a sufficiently uniform field in the left ventricle, though the subcutaneous patch over the sternum generated a strong field in the right ventricle. A major disadvantage was the maximum gradient in the myocardium was unacceptably high.

**Effect of an Infarct (INF)**

With the standard electrode configuration, the effect of an infarct (INF 1) was to reduce the voltage and energy for defibrillation by 5% and 7%, respectively. The main reason for the reduction was that the infarct was in the lowest gradient region of the ventricles and the gradient in this region could be sub-threshold. Therefore, a lower electrode voltage could be used. For this configuration, the shape of the electric field was little changed by the bulge of the infarcted region.

With an apical subcutaneous patch (INF 2), the opposite result was found. There was now an increase in voltage and energy of 5% and 10%, respectively, compared to the standard transvenous plus patch configuration. The main reason for this was the bulging wall of the left ventricle displaced some of the lung tissue from between the heart and the patch. This resulted in a shunting of current through this region and a less favourable electric field in the posterior lateral wall of the left ventricle.

The reason for the good performance of configurations such as EP-T was that the myocardium was sandwiched between electrodes that were closely spaced, had a large surface-area and wasted little voltage and energy outside the heart. The potential effectiveness of this type of configuration can be shown by the simple one dimensional example illustrated in figure 8.32. Part (a) shows the myocardium sandwiched between two electrodes and part (b) shows the same configuration with additional thoracic tissue between the electrodes. Expressions for the voltage and energy for successful defibrillation for these configurations are as follows:

$$V_E = q_t d_m \left( \frac{R_m + R_o}{R_m} \right) \quad (8.3)$$

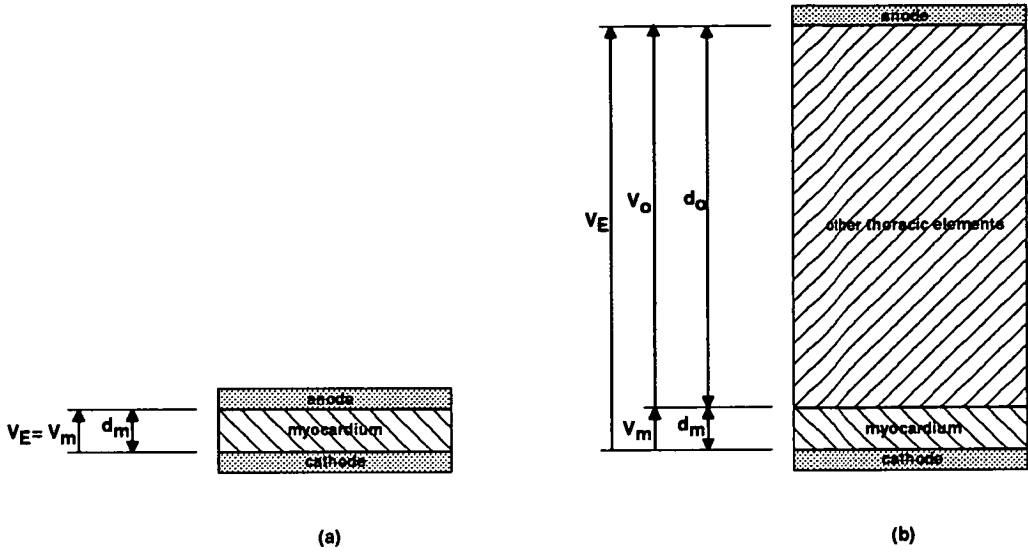


Figure 8.32: (a) efficient 'myocardial sandwich' configuration where the voltage and energy is dissipated entirely within the myocardium (b) less efficient standard configuration with additional voltage and energy dissipation within other parts of the thorax

and

$$E = \frac{V_i^2 C}{2} \left( 1 - \exp \frac{-2t}{(R_m + R_o) C} \right), \quad (8.4)$$

where  $V_E$  is the anode-cathode voltage,  $E$  is the energy dissipated for a monophasic truncated decaying exponential waveform with an peak voltage  $V_i$ , duration  $t$  and time-constant dependent on the anode-cathode resistance  $R$  and the capacitance  $C$ . Subscripts  $m$  and  $o$  designate myocardium and other thoracic elements, respectively,  $q_t$  is the defibrillation voltage gradient threshold, and  $d$  is the region thickness. Of course, minimum voltage and energy are obtained when there is only myocardium between the electrodes (i.e.  $R_o = 0$ ). This is a theoretical minimum that can not be reduced and is dependent on the thickness and conductivity of the myocardium. In practical electrode configurations, there would usually at least be some of the left ventricular blood as well as myocardium between the electrodes.

## 8.7 Conclusion

The ability to control the variables in the model allowed investigations to be done where direct comparisons of electrode configurations were made. The results of these investigations clearly differentiated the performance of each configuration and allowed conclusions to be drawn regarding the relative merits of each. Such a controlled comparison between many electrode configurations would have been very difficult, if not virtually impossible to do experimentally and illustrates some of the benefits of modelling.

# Chapter 9

## Conclusion

The aim of this thesis was to model the electric field from implantable defibrillators. It was intended that the capabilities and performance of the methods used would be such that it would be possible to model realistic electrode configurations and realistic torso structures. It was desirable that the solution speed would be sufficient to enable optimisation of electrode position in a torso within a practical time period.

A brief biomedical background was presented which discussed the heart structure, the nature of fibrillation and defibrillation and defibrillators. The most important conclusions from this chapter include the following. First, that the ventricular myocardium is electrically isolated from the atrial myocardium, which means that defibrillation of the ventricles alone is sufficient to ensure defibrillation success. Second, that a minimum shock strength through all or a critical mass of the ventricles is an effective criteria to apply to assess the success or failure of defibrillation. Third, that there is a maximum shock strength above which fibrillation may be reinduced.

Relevant modelling literature was discussed. Most of the models in the literature were finite element models and were subject to both the advantages and disadvantages of this method. The main advantage was the ability to include detailed anisotropy. The main disadvantage was the complex mesh

required for each configuration and the amount of computation required for electrode optimisation.

The numerical methods used were presented. The mathematical basis of the model was Laplace's equation and this was solved using the boundary element method. Constant quadrilateral elements were used. The method involved calculation of boundary potentials and normal gradients and then post-processing to find internal potentials and gradients. The potential gradient on boundaries was approximated by linearly interpolating element nodal potentials. A finite element model was also developed using the commercial package FIDAP. Linear brick elements with 8 nodes were used in this model.

The implementation of the boundary element method involved constructing the torso geometry, specifying boundary conditions and electrodes, building the governing matrix equations, solving the equations and performing post-processing calculations. Torso construction involved manual digitisation of CT or MRI scans followed by mesh generation using semi-automatic and manual methods. This procedure resulted in adequate representation of the torso structures but would be impractical for generation of a large number of torsos. Once the torso was constructed, it was a relatively simple matter to specify the boundary conditions and electrodes. Following this, the governing matrix equations were built then solved. This was a time-consuming task and typically took approximately 69 hours on a Silicon Graphics Iris Indigo. Efficient out-of-core techniques were developed to enable solution of the matrices, which typically contained more than 500 mega-bytes of non-zero values. A technique was also developed that allowed electrode configurations to be optimised without the need to repeat all the calculations. Solutions to modified configurations only took approximately 2 hours to solve. This was a major advantage of the method used.

The numerical methods were validated against analytical and finite element models. The results of the validations indicated the numerical methods were

accurate and the implementation had been performed correctly. Next, model results were validated against measured results on sheep and humans. The field magnitudes in the sheep compared well with that predicted by the model and the electrode resistance and voltage required for defibrillation predicted by the model compared well with those measured in humans.

A number of investigations were performed using the boundary element model with various electrode configurations. Results were visualised over surfaces in the model and on slices through regions. Results were presented as values of defibrillation voltage, energy, inter-electrode resistance and maximum potential gradient. Some configurations required significantly lower voltage and energy for defibrillation than configurations in current use. It was found that because the variables in the model could be controlled, direct comparisons of electrode configurations could be made. The results of these investigations clearly differentiated the performance of each configuration and allowed conclusions to be drawn regarding the relative merits of each. Such a controlled comparison between many electrode configurations would have been difficult, if not virtually impossible to do experimentally and illustrated the benefits of modelling. In particular, a new transvenous configuration with one electrode in the right ventricle and one in the inferior vena cava was found to be a significant improvement over current configurations and may be clinically useful. Other configurations, some less practical than this, were found to significantly reduce defibrillation thresholds. Configurations with a transvenous electrode in the right ventricle and a large epicardial patch performed particularly well. The factors affecting reduction of voltage and energy were discussed, including the limit to reductions. The conclusion was obtained that configurations that sandwiched the myocardium between two electrodes produced the lowest voltage and energy. This was confirmed by results from modelling this type of configuration.

The advantages of using the boundary element method rather than a purely

domain based method included discretisation using surface rather than volume elements, ease of modification of the discretised torso, attainment of accurate values of potentials and gradients for many configurations without requiring extensive re-meshing or mesh refinement, even in regions with relatively large potential gradients, and the avoidance of iterative methods and the associated convergence issues. One of the biggest advantages was that when electrode configurations were modified and the field re-solved, only a relatively small amount of re-computation was required. The main disadvantage of using the boundary element method was the difficulty of incorporating anisotropy.

In conclusion, the boundary element model was successful in modelling the electric field in the torso and in predicting implantable defibrillator performance. The model has potential to be used in research and development and in clinical settings.

### **Future Work**

There are a number of developments that can be considered for future work. One is the inclusion of anisotropic conductivity in the boundary element model. In regard to implantable defibrillators, the anisotropy of only two torso regions is significant. Those regions are the myocardium and the skeletal muscle layer. Adding anisotropy would represent these areas more accurately. The advantages of the boundary element method would be maintained in the other regions.

Two possible methods of including anisotropy are as follows. The anisotropic regions could be split into relatively small boundary element regions. Anisotropy in each region would be forced to be constant in direction relative to the torso axes, because of inherent restrictions in the boundary element method. Therefore, many small regions would be needed to adequately represent continuously varying anisotropy. The numerical methods would need to be modified to allow for these additional regions. Alternatively, the boundary element model

could be modified so that the anisotropic regions were represented by finite elements. The numerical methods would be modified to combine the boundary and finite element methods in the isotropic and anisotropic regions. Methods of combining the boundary and finite element methods are well established (see, for example, [144, 85]).

Anisotropy was actually added to the ventricular myocardium in the finite element human torso model. Unfortunately, though, numerical results were not obtained from this model due to unforeseen difficulties with the implementation of anisotropy in the FIDAP solver. Therefore this work was not presented in this thesis. However, the methods of including anisotropy may be used in future work and are as follows. The myocardium was considered to be formed from fibres of tissue constructed in spiral formations and forming sheets running parallel to the endo- and epicardium. The resistivity of the myocardium was assumed to be 2, 5, and  $12.5\Omega m$  in the fibre, sheet and cross-sheet directions, respectively, from published values. As an approximation, isotropy was assumed within the sheets (an average of  $3.5\Omega m$ ) and anisotropy across the sheets ( $12.5\Omega m$ ) [146]. The direction of anisotropy for each finite element was then obtained from the orientation of the nearest segment of the epi- or endocardium.

Apart from inclusion of anisotropy, there are other areas for future work. One is the use of high-order boundary elements rather than constant elements. High-order elements allow potential and potential gradient to be modelled as continuous functions over the boundaries. This would improve the model in regard to calculation of boundary gradients. Also, boundaries could be modelled as smooth, and fewer elements could be used which may improve the speed of solution.

There are other strategies that could also be used for improving the speed of solution. One is to use additional, strategically placed subregions to reduce

the size of some of the original regions. Another is to manipulate the governing matrix equations further before forming the final matrix equation to give the option of calculating potentials and gradients only in the myocardium rather than throughout the whole torso. A further strategy would be to represent low-conductivity regions such as bone by voids.

Another area for future work is the development of methods to automate torso construction. Automated construction would make the modelling of individual patients more practical. One way to build a torso model for a patient would be to resize and reshape the boundaries of regions from the current torso model to match the boundary positions taken on CT or MRI scans, or to match key landmarks from x-ray pictures. Alternatively, image processing techniques could be implemented to extract regions from MRI and CT scans and this information used to construct the torso. Knowledge of the structure of the human body could be used in the process.

The utility of the model in optimising the electrode configurations in patients would be improved by addition of some form of automatic optimisation. Algorithms used by others ([101, 103], for example) for automatically optimising electrode position may be suitable for this purpose.

There is also scope for further validation with improved sheep experiments. These experiments may involve using multiple sheep, high resolution scans to accurately model torso geometry and locate electrodes and *in vivo* measurement of tissue conductivity.

Finally, the model could be used in a number of studies, of which two examples are given. One is a parameter sensitivity study to find how the model results respond to variations in tissue conductivity and level of anatomical detail. This would provide information on the sensitivity and robustness of the model to changes in these factors. The other is a study modelling individual patients who are to receive an implantable defibrillator. Values of defibrillation voltage, energy and resistance could be predicted from the model and compared

to values found clinically at the time of implantation from normal testing of the defibrillator. Data could be arranged as matched pairs and used for various purposes such as model validation, or clinically to predict thresholds or to find patients with abnormal results.

# Appendix A

## Detail of the Boundary

### Element Model

Consider the discretised torso in which the torso tissue, spine, sternum, ribs, left and right lungs, heart and arterial and venous blood ( $T$ ,  $S_p$ ,  $S_t$ ,  $R$ ,  $L_l$ ,  $L_r$ ,  $H$ ,  $B_a$  and  $B_v$ , respectively) are represented as isotropic, homogeneous regions. The torso surface consists of the free surface ( $T_t$ ) and subcutaneous patch electrodes ( $E_s$ ). The epicardial surface consists of the free surface ( $H_h$ ) and epicardial patch electrodes. The insulated outer surface ( $E_o$ ) of an epicardial patch is a region constructed over the inner surface ( $E_i$ ), which is part of the epicardium. Transvenous electrodes ( $E_t$ ) are located within the blood. Multiple transvenous and epicardial electrodes are indicated by the subscripts  $1, \dots, n$ .

Equation 4.17 is applied in each region in turn resulting in a set of equations that are combined to form matrix equations A.1 to A.4. The matrix notation employed is  $M_{sub}^{sup}$ . The subscript specifies the region and the superscript specifies the boundary under consideration.

Torso tissue: the boundaries of this region are the torso surface, heart, spine,

sternum, ribs, lungs. The matrix equation for this region is

$$\begin{aligned}
 & \left[ \begin{array}{cccccccccccc} H_T^{T_i} & H_T^{E_i} & H_T^{S_p} & H_T^{S_i} & H_T^R & H_T^{L_i} & H_T^{L_r} & H_T^{H_h} & H_T^{E_{o_1}} & \dots & H_T^{E_{o_n}} \end{array} \right] \left\{ \begin{array}{c} U_T^{T_i} \\ U_T^{E_i} \\ U_T^{S_p} \\ U_T^{S_i} \\ U_T^R \\ U_T^{L_i} \\ U_T^{L_r} \\ U_T^{H_h} \\ U_T^{E_{o_1}} \\ \vdots \\ U_T^{E_{o_n}} \end{array} \right\} \\
 & = \left[ \begin{array}{cccccccccccc} G_T^{T_i} & G_T^{E_i} & G_T^{S_p} & G_T^{S_i} & G_T^R & G_T^{L_i} & G_T^{L_r} & G_T^{H_h} & G_T^{E_{o_1}} & \dots & G_T^{E_{o_n}} \end{array} \right] \left\{ \begin{array}{c} Q_T^{T_i} \\ Q_T^{E_i} \\ Q_T^{S_p} \\ Q_T^{S_i} \\ Q_T^R \\ Q_T^{L_i} \\ Q_T^{L_r} \\ Q_T^{H_h} \\ Q_T^{E_{o_1}} \\ \vdots \\ Q_T^{E_{o_n}} \end{array} \right\} \quad (A.1)
 \end{aligned}$$

Spine: the only boundary of this region is the spine. The matrix equation for this region is:

$$\left[ \begin{array}{c} H_{S_p}^{S_p} \end{array} \right] \left\{ \begin{array}{c} U_{S_p}^{S_p} \end{array} \right\} = \left[ \begin{array}{c} G_{S_p}^{S_p} \end{array} \right] \left\{ \begin{array}{c} Q_{S_p}^{S_p} \end{array} \right\} \quad (A.2)$$

Similar equations to Equation A.2 hold for the sternum, ribs, lungs, and arterial blood regions since they also only involve the boundary of one region.

Heart: the boundaries of this region are the heart, the inner surface of epicardial electrodes and arterial and venous blood. The resulting matrix equation

is:

$$\begin{aligned}
 & \left[ \begin{array}{ccccc} H_H^{H_h} & H_H^{E_{i_1}} & \dots & H_H^{E_{i_n}} & H_H^{B_a} & H_H^{B_v} \end{array} \right] \left\{ \begin{array}{c} U_H^{H_h} \\ U_H^{E_{i_1}} \\ \vdots \\ U_H^{E_{i_n}} \\ U_H^{B_a} \\ U_H^{B_v} \end{array} \right\} = \\
 & \left[ \begin{array}{ccccc} G_H^{H_h} & G_H^{E_{i_1}} & \dots & G_H^{E_{i_n}} & G_H^{B_a} & G_H^{B_v} \end{array} \right] \left\{ \begin{array}{c} Q_H^{H_h} \\ Q_H^{E_{i_1}} \\ \vdots \\ Q_H^{E_{i_n}} \\ Q_H^{B_a} \\ Q_H^{B_v} \end{array} \right\} \quad (A.3)
 \end{aligned}$$

Venous blood: the boundaries of this region are the venous blood cavities and transvenous electrodes. The resulting matrix equation is:

$$\left[ \begin{array}{ccccc} H_{B_v}^{B_v} & H_{B_v}^{E_{t_1}} & \dots & H_{B_v}^{E_{t_n}} \end{array} \right] \left\{ \begin{array}{c} U_{B_v}^{B_v} \\ U_{B_v}^{E_{t_1}} \\ \vdots \\ U_{B_v}^{E_{t_n}} \end{array} \right\} = \left[ \begin{array}{ccccc} G_{B_v}^{B_v} & G_{B_v}^{E_{t_1}} & \dots & G_{B_v}^{E_{t_n}} \end{array} \right] \left\{ \begin{array}{c} Q_{B_v}^{B_v} \\ Q_{B_v}^{E_{t_1}} \\ \vdots \\ Q_{B_v}^{E_{t_n}} \end{array} \right\} \quad (A.4)$$

The following additional equations describe the compatibility conditions on the boundaries.

Torso-spine interface:

$$\left. \begin{aligned} U^{TS_p} &= U_T^{TS_p} = U_{S_p}^{TS_p} \\ Q^{TS_p} &= Q_{S_p}^{TS_p} = -\frac{k_T}{k_{S_p}} Q_T^{TS_p} = -k_{TS_p} Q_T^{TS_p} \end{aligned} \right\} \quad (A.5)$$

where  $k_i$  is the conductivity in region  $i$  and the notation  $k_{ij}$  denotes  $k_i/k_j$ . The interfaces between the torso and the sternum, ribs and lungs, respectively, were similar to Equation A.5.

Heart and arterial-blood interface:

$$\left. \begin{aligned} U^{HB_a} &= U_H^{HB_a} = U_{B_a}^{HB_a} \\ Q^{HB_a} &= Q_{B_a}^{HB_a} = -k_{HB_a} Q_H^{HB_a} \end{aligned} \right\} \quad (A.6)$$

The interface between the heart and venous blood was similar to Equation A.6.

The interface compatibility equations can be substituted into equations A.1, ..., A.4 to relate each equation through the potential and potential gradient on the region boundaries. The equations are combined as follows:

$$\begin{bmatrix}
 H_T^{Tt} & H_T^{Es} & H_T^{Sp} & H_T^{St} & H_T^R & H_T^{Ll} & H_T^{Lr} & H_T^{Hh} & H_T^{Eo1} & \dots & H_T^{Eon} & 0 & \dots & 0 & 0 & 0 & 0 & \dots & 0 \\
 0 & 0 & H_{Sp}^{Sp} & 0 & 0 & 0 & 0 & 0 & 0 & \dots & 0 & 0 & \dots & 0 & 0 & 0 & 0 & \dots & 0 \\
 0 & 0 & 0 & H_{St}^{St} & 0 & 0 & 0 & 0 & 0 & \dots & 0 & 0 & \dots & 0 & 0 & 0 & 0 & \dots & 0 \\
 0 & 0 & 0 & 0 & H_R^R & 0 & 0 & 0 & 0 & \dots & 0 & 0 & \dots & 0 & 0 & 0 & 0 & \dots & 0 \\
 0 & 0 & 0 & 0 & 0 & H_{Ll}^{Ll} & 0 & 0 & 0 & \dots & 0 & 0 & \dots & 0 & 0 & 0 & 0 & \dots & 0 \\
 0 & 0 & 0 & 0 & 0 & 0 & H_{Lr}^{Lr} & 0 & 0 & \dots & 0 & 0 & \dots & 0 & 0 & 0 & 0 & \dots & 0 \\
 0 & 0 & 0 & 0 & 0 & 0 & 0 & H_H^{Hh} & 0 & \dots & 0 & H_H^{Ei1} & \dots & H_H^{Eon} & H_H^{Ba} & H_H^{Bv} & 0 & \dots & 0 \\
 0 & 0 & 0 & 0 & 0 & 0 & 0 & 0 & 0 & \dots & 0 & 0 & \dots & 0 & H_{Ba}^{Ba} & 0 & 0 & \dots & 0 \\
 0 & 0 & 0 & 0 & 0 & 0 & 0 & 0 & 0 & \dots & 0 & 0 & \dots & 0 & 0 & H_{Bv}^{Bv} & H_{Bv}^{Et1} & \dots & H_{Bv}^{Etn}
 \end{bmatrix}
 \begin{Bmatrix}
 U^{Tt} \\
 U^{Es} \\
 U^{Sp} \\
 U^{St} \\
 U^R \\
 U^{Ll} \\
 U^{Lr} \\
 U^{Hh} \\
 U^{Eo1} \\
 \vdots \\
 U^{Eon} \\
 U^{Ei1} \\
 \vdots \\
 U^{Ein} \\
 U^{Ba} \\
 U^{Bv} \\
 U^{Et1} \\
 \vdots \\
 U^{Etn}
 \end{Bmatrix}
 =$$

[illegible]

(A.7)

In this case,  $U_T^{E_s}$ ,  $U_H^{E_i}$  and  $U_{B_v}^{E_t}$  are known and  $Q_T^{T_t} = Q_T^{E_o} = 0$ . Rearranging equation A.7 so the unknowns are on the left-hand side and the knowns are on the right results in equation A.8, which is in the form of equation 4.20. The left hand side matrix of equation A.8 is a square matrix and is known from the discretised torso geometry. The right hand side vector is known from the torso and electrode geometry and the applied boundary conditions. The vector of unknowns is found by solving the equation.

[illegible]

$$\begin{pmatrix}
 U^{T_t} \\
 Q^{T_s} \\
 U^{Sp} \\
 U^{S_t} \\
 U^R \\
 U^{L_l} \\
 U^{L_r} \\
 U^{H_h} \\
 U^{E_{o1}} \\
 \vdots \\
 U^{E_{on}} \\
 Q^{Sp} \\
 Q^{S_t} \\
 Q^R \\
 Q^{L_l} \\
 Q^{L_r} \\
 Q^{H_h} \\
 Q^{E_{i1}} \\
 \vdots \\
 Q^{E_{in}} \\
 Q^{Ba} \\
 Q^{B_v} \\
 U^{Ba} \\
 U^{B_v} \\
 Q^{E_{t1}} \\
 \vdots \\
 Q^{E_{tn}}
 \end{pmatrix} = \begin{pmatrix}
 0 \\
 -H_T^{E_s} U^{E_s} \\
 0 \\
 0 \\
 0 \\
 0 \\
 0 \\
 0 \\
 0 \\
 \vdots \\
 0 \\
 0 \\
 0 \\
 0 \\
 0 \\
 0 \\
 -H_H^{E_{i1}} U^{E_{i1}} \\
 \vdots \\
 -H_H^{E_{in}} U^{E_{in}} \\
 0 \\
 0 \\
 0 \\
 0 \\
 0 \\
 -H_H^{E_{t1}} U^{E_{t1}} \\
 \vdots \\
 H_H^{E_{tn}} U^{E_{tn}}
 \end{pmatrix}$$

(A.8)

# Appendix B

## Element Integrals

Integration over quadrilateral elements was done using two dimensional Gaussian quadrature. The integrals were those in equations (4.12) and (4.13):

$$\hat{H}_{ij} = \int_{\Gamma_j} q^* d\Gamma, \quad (\text{B.1})$$

and

$$G_{ij} = \int_{\Gamma_j} u^* d\Gamma. \quad (\text{B.2})$$

First, basis functions  $\phi_i$  for were defined in terms of dimensionless coordinates  $\eta_1, \eta_2$  which vary from -1 to 1:

$$\phi_1 = \frac{1}{4}(1 - \eta_1)(1 - \eta_2), \quad (\text{B.3})$$

$$\phi_2 = \frac{1}{4}(1 + \eta_1)(1 - \eta_2), \quad (\text{B.4})$$

$$\phi_3 = \frac{1}{4}(1 + \eta_1)(1 + \eta_2), \quad (\text{B.5})$$

and

$$\phi_4 = \frac{1}{4}(1 - \eta_1)(1 + \eta_2). \quad (\text{B.6})$$

The integrals were then transformed from the  $x, y, z$  coordinate system to the  $\eta_1, \eta_2$  system. Transforming the differential area  $d\Gamma$ :

$$d\Gamma = \left| \frac{\partial \mathbf{r}}{\partial \eta_1} \times \frac{\partial \mathbf{r}}{\partial \eta_2} \right| d\eta_1 d\eta_2 = |\mathbf{G}| d\eta_1 d\eta_2 \quad (\text{B.7})$$

where

$$\frac{\partial \mathbf{r}}{\partial \eta_1} = \left( \frac{\partial x}{\partial \eta_1}, \frac{\partial y}{\partial \eta_1}, \frac{\partial z}{\partial \eta_1} \right) \quad (\text{B.8})$$

and

$$\frac{\partial \mathbf{r}}{\partial \eta_2} = \left( \frac{\partial x}{\partial \eta_2}, \frac{\partial y}{\partial \eta_2}, \frac{\partial z}{\partial \eta_2} \right) \quad (\text{B.9})$$

Note that  $|\mathbf{G}|$  is the magnitude of the normal vector:

$$\mathbf{n} = \frac{\partial \mathbf{r}}{\partial \eta_1} \times \frac{\partial \mathbf{r}}{\partial \eta_2} = (g_1, g_2, g_3) \quad (\text{B.10})$$

where

$$\begin{aligned} g_1 &= \frac{\partial y}{\partial \eta_1} \frac{\partial z}{\partial \eta_2} - \frac{\partial y}{\partial \eta_2} \frac{\partial z}{\partial \eta_1} \\ g_2 &= \frac{\partial z}{\partial \eta_1} \frac{\partial x}{\partial \eta_2} - \frac{\partial z}{\partial \eta_2} \frac{\partial x}{\partial \eta_1} \\ g_3 &= \frac{\partial x}{\partial \eta_1} \frac{\partial y}{\partial \eta_2} - \frac{\partial x}{\partial \eta_2} \frac{\partial y}{\partial \eta_1} \end{aligned} \quad (\text{B.11})$$

and therefore

$$|\mathbf{G}| = (g_1^2 + g_2^2 + g_3^2)^{1/2}. \quad (\text{B.12})$$

The integrals of equations (B.1) and (B.2) can now be rewritten

$$\int_{\Gamma_j} q^* d\Gamma = \int_{-1}^{+1} \int_{-1}^{+1} q^* |\mathbf{G}| d\eta_1 d\eta_2 \quad (\text{B.13})$$

and

$$\int_{\Gamma_j} u^* d\Gamma = \int_{-1}^{+1} \int_{-1}^{+1} u^* |\mathbf{G}| d\eta_1 d\eta_2 \quad (\text{B.14})$$

The geometry for each element was written in terms of the basis functions:

$$x = \phi_1 x_1 + \phi_2 x_2 + \phi_3 x_3 + \phi_4 x_4 \quad (\text{B.15})$$

$$y = \phi_1 y_1 + \phi_2 y_2 + \phi_3 y_3 + \phi_4 y_4 \quad (\text{B.16})$$

$$z = \phi_1 z_1 + \phi_2 z_2 + \phi_3 z_3 + \phi_4 z_4 \quad (\text{B.17})$$

and  $g_1, g_2$  and  $g_3$  found analytically using equation (B.11) while  $|\mathbf{G}|$  was found using equation (B.12).

The integrals in equations (B.13) and (B.14) can now be evaluated. This is done numerically using two dimensional Gaussian quadrature:

$$\int_{\Gamma_j} q^* d\Gamma = \frac{1}{4\pi} \sum_{m=1}^p \sum_{l=1}^p w_m w_l \frac{\hat{\mathbf{r}} \cdot \hat{\mathbf{n}}}{r^2} |\mathbf{G}| \quad (\text{B.18})$$

and

$$\int_{\Gamma_j} u^* d\Gamma = \frac{1}{4\pi} \sum_{m=1}^p \sum_{l=1}^p w_m w_l \frac{1}{r} |\mathbf{G}| \quad (\text{B.19})$$

where  $\hat{\mathbf{r}}$  is the unit radius vector and  $\hat{\mathbf{n}}$  is the unit surface normal, and  $w_m$  and  $w_l$  are the Gaussian weights for the  $p$  integration points. Usually, between 6 and 12 integration points results in accurate solutions. In the case of the singularity, the integration point  $i$  was on the element over which integration was being done. In this case, the integral in equation (B.13) is zero [144] while an accurate calculation for the integral in equation (B.14) is obtained by using more integration points than for the non-singular integrations, 24 integration points usually being satisfactory.

# Appendix C

## Statistical Definitions

The correlation coefficient was defined as

$$CC = \frac{\Sigma(x_i - \bar{x}) \cdot (y_i - \bar{y})}{\sqrt{\Sigma(x_i - \bar{x})^2} \sqrt{\Sigma(y_i - \bar{y})^2}}, \quad (C.1)$$

and the relative error as

$$RE = \sqrt{\frac{\Sigma(x_i - y_i)^2}{\Sigma x_i^2}}. \quad (C.2)$$

Appendix D

Enguard Electrodes

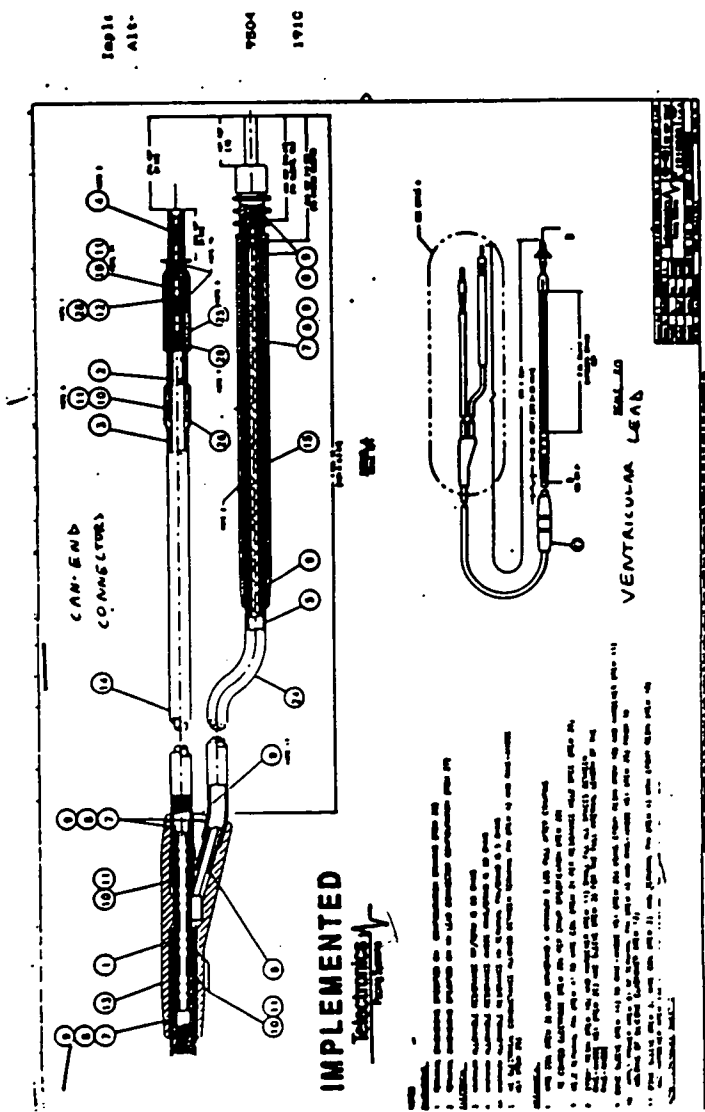


Figure D.1: Enguard ventricular electrode

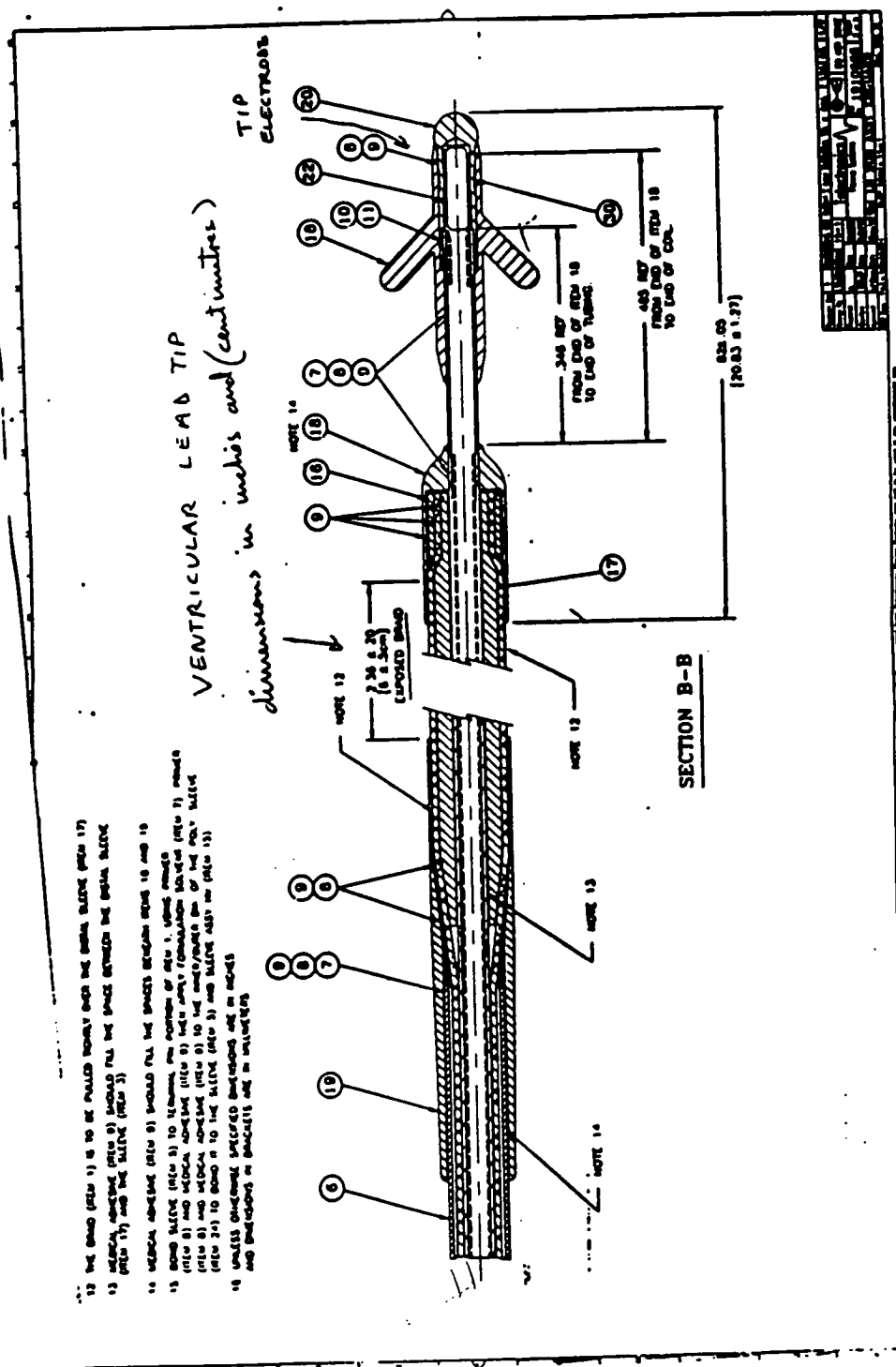


Figure D.2: Enguard centricular electrode-tip detail

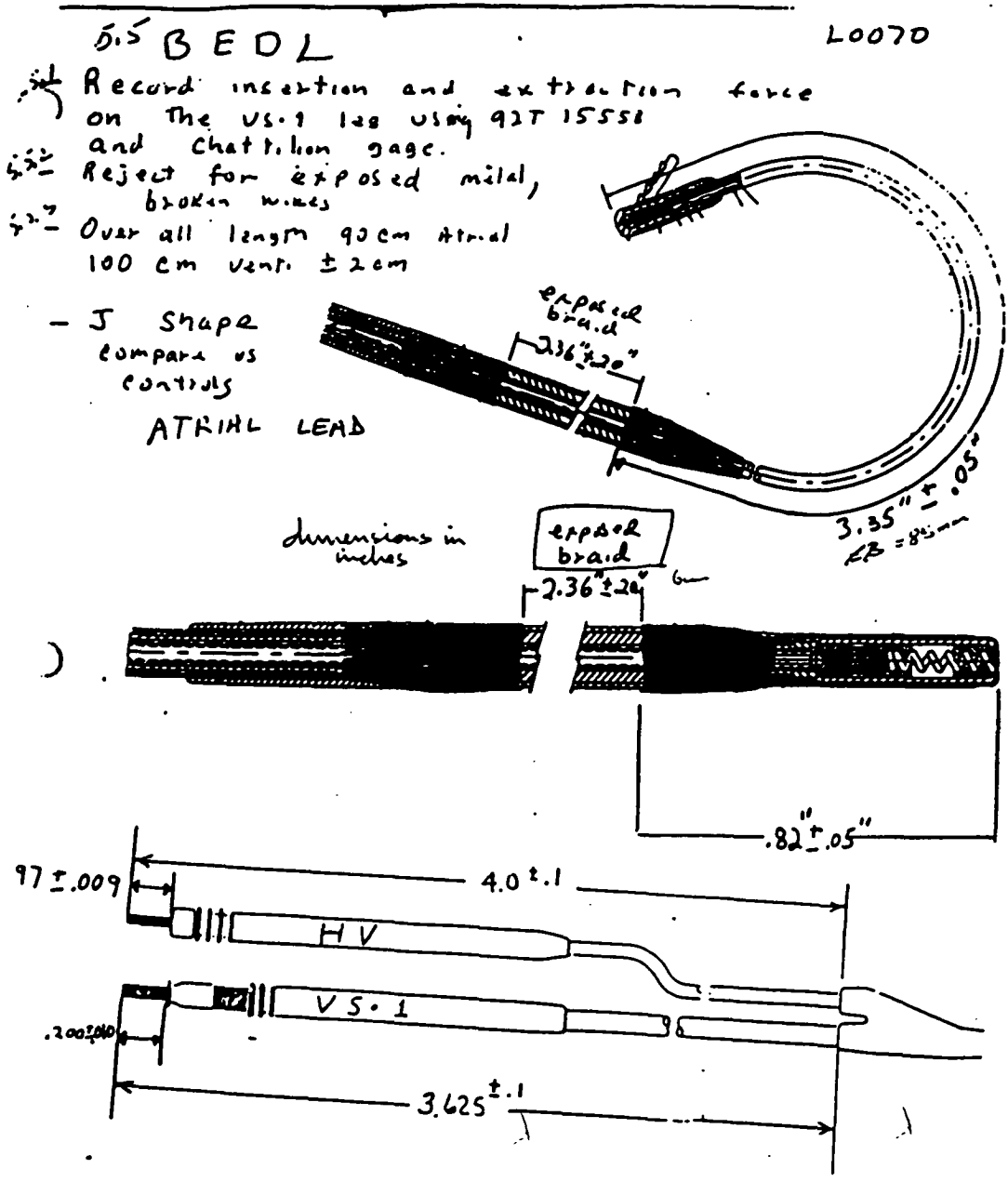
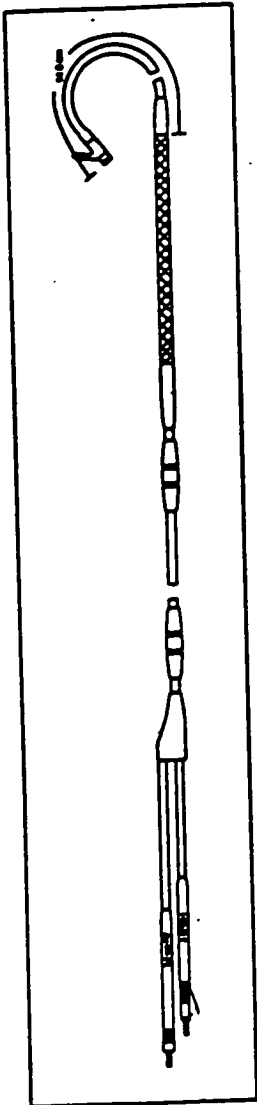


Figure D.3: Enguard Standard Atrial Lead 040-020

MODEL 040-022 GENERAL SPECIFICATIONS

DESCRIPTION	BIFURCATED TERMINAL CONNECTOR	LEAD LENGTH (mm)	LEAD BODY DIAMETER (mm)	CONDUCTIONS (Material Cat)	CONDUCTOR RESISTANCE AT 25°C (ohm)	ELECTRODE SEPARATION (mm)	ELECTRODE MATERIAL	ELECTRODE SURFACE AREA (mm²)	SUGGESTED INTRODUCER SIZE
ENGUARD PFX	Pneumoseal Insulator V6-1 High voltage insulator 3.3 mm (1/8")	80	2.0	Inner: Quadraflex MP-200 Outer: Quadraflex MP-200 Alloy Hypoguard	Inner 16 (mm) Outer 8 (mm)	14.5	Quadraflex Polymer 18 Standard Titanium	Distal 9.0 Seal 800	12F



PRIOR TO IMPLANTATION

It is important to maintain the cleanliness of the electrode prior to implant. Contamination can occur if the electrodes come in contact with virtually any surface or material. It is therefore recommended that the lead remain in the sterile tray until it is time to be implanted.

IMPLANTING THE LEAD

**Note:** Although the following implantation instructions are based on experience gathered to date, the physician may wish to vary the procedure in accordance with clinical judgment.

**Caution:** Avoid blood from entering into the V6-1 pin or contacting the stylet. This occurrence may make stylet insertion and extraction difficult. A spare stylet is provided.

- Insert the stylet through the hole in the V6-1 lead terminal connector. Gently advance the stylet to the distal end of the lead.

**Caution:**

When inserting the stylet, use extreme care to avoid penetrating the lead wall or bending the lead with the tip of the stylet. To help prevent conductor fracture, support the entire lead by

- advancing the stylet all the way to the tip. Do not bend the lead to an acute angle anywhere along its length.

- Under fluoroscopy, advance the lead slowly and carefully. If advancement is resisted, withdraw the lead a short distance, ensure that the stylet is fully inserted into the lead, and advance the lead again.

- Advance the lead into the atrium.
  - After the lead's tip enters the right atrium, withdraw the stylet up to 10 cm, until the distal end of the lead returns to a curved shape.

- Maneuver the lead until the distal electrode reaches the intended location (the junction in the right atrial appendage). If the stylet is re-advanced during positioning, the lead resistance may be lost as the stylet straightens the lead's tip.

- Use fluoroscopy to verify the position of the distal electrode. When viewed laterally, the lead should be pointing anteriorly. In the anteroposterior view, the lead is typically in or near the median plane.

- Use fluoroscopy to verify the position of the HV electrode in the SVC.

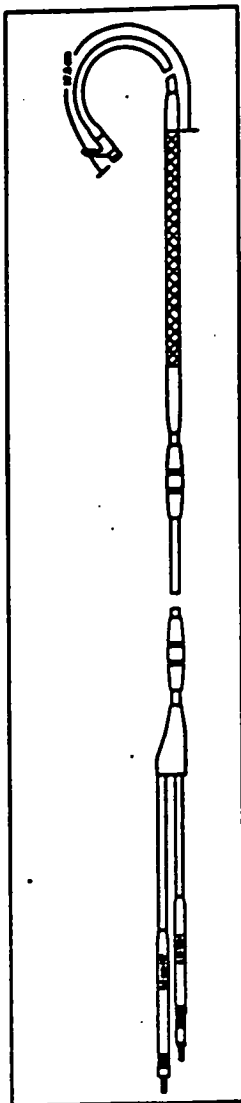
**Caution:**

To prevent HV electrode fracture, the electrode must not be positioned under the junction of the distal and first rib.

Figure D.4: Enguard Atrial Lead 040-022

MODEL 040-024 GENERAL SPECIFICATIONS

DESCRIPTION	IMPLICATED TERMINAL CONNECTOR	LEAD LENGTH (mm)	LEAD BODY DIAMETER (mm)	CONDUCTORS (Material Cat)	CONDUCTOR RESISTANCE AT 37°C (ohms)	ELECTRODE SEPARATION (mm)	ELECTRODE MATERIAL	ELECTRODE SURFACE AREA (mm <sup>2</sup> )	SUGGESTED INTRODUCER SIZE
ENGUARD PFX	Pushbutton type VBI high voltage impedance 3.7 mm (P/N)	90	2.0	Inner: Quadralite Outer: Quartz Surf: 24K Alloy Housing	Inner 60 (mm) Outer 8 (mm)	17.5	Thick Platinum Platinum 10 Borel Titanium	Distal 8.0 Distal 600	18F

**PRIOR TO IMPLANTATION**

It is important to maintain the cleanliness of the electrode prior to implant. Contamination can occur if the electrode curve is altered with virtually any surface is exposed. It is therefore recommended that the lead remain in the trial tray until it is time to be implanted.

**IMPLANTING THE LEAD****Alert:**

Although the following implantation instructions are based on experience gained to date, the physician may wish to vary the procedure in accordance with clinical judgment.

**Caution:**

Avoid blood from entering into the pleth or connecting the stylet. This occurrence may make stylet insertion and location difficult. A spare stylet is provided.

- Insert the stylet through the hole in the VBI lead terminal connector. Gently advance the stylet to the distal end of the lead.

**Caution:**

When handling the stylet, use extreme care to avoid penetrating the lead wall or bending the lead with the tip of the stylet. To help prevent conductor fracture, support the entire lead by

- advancing the stylet all the way to the tip. Do not bend the lead to an acute angle anywhere along its length.

- Under fluoroscopy, advance the lead slowly and carefully. If advancement is resisted, withdraw the lead a short distance, ensure that the stylet is fully inserted into the lead, and advance the lead again.

- Advance the lead into the atrium.

- After the lead's tip enters the right atrium, withdraw the stylet (up to 10 cm), until the distal end of the lead returns to a curved shape.

- Manipulate the lead until the distal electrode reaches the intended location (be lateral to the right atrial appendage). If the stylet is re-advanced during positioning, some resistance may be felt as the stylet straightens the lead's tip.

- Use fluoroscopy to verify the position of the distal tip electrode. When viewed laterally, the lead should be pointing anteriorly. In the anteroposterior view, the lead is typically in or near the median plane.

- Use fluoroscopy to verify the position of the HV electrode in the SVC.

**Caution:**

To prevent HV electrode fracture, the electrode must not be positioned under the junction of the chest and first rib.

Figure D.5: Enguard Atrial Lead 040-024

# Bibliography

- [1] L. Glass, P. Hunter, and A. McCulloch, editors. R.E. Ideker and A.S.L. Tang and D.W. Frazier and N. Shibata and P.S. Chen and J.M. Wharton. In *Theory of Heart*. Springer-Verlag, New York, 1991.
- [2] T.F. Kinst, S.R. Eisenberg, N.G. Perlmutter, and J.L. Lehr. Internal electrical defibrillation: A three-dimensional finite element model of current density distribution. In *Proc IEEE Eng in Med and Biol*, volume 13, 1993.
- [3] M.R. Rosen. *Electrical therapy for cardiac arrhythmias*, chapter 1. W.B. Saunders Company, Philadelphia, 1990.
- [4] M.A. Allesie, F.I.M. Bonke, and F.J.C. Schopman. Circus movement in rabbit atrial muscle as a mechanism of tachycardia. iii. the “leading circle” concept: A new model of circus movement in cardiac tissue without the involvement of an anatomical obstacle. *Circulation Research*, 41:9, 1977.
- [5] D.P. Zipes and J. Jalife, editors. J.M. Davidenko. In *Cardiac Electrophysiology*. W.B. Saunders Company, Philadelphia, 2 edition, 1995.
- [6] D.P. Zipes and J. Jalife, editors. L. Glass. In *Cardiac Electrophysiology*. W.B. Saunders Company, Philadelphia, 2 edition, 1995.
- [7] A.L. Goldberger, V. Bhargava, B.J. West, and A.J. Mandell. Some observations of the question: Is ventricular fibrillation chaos? *Physica D*, 19:282–289, 1986.
- [8] R.E. Ideker, G.J. Klein, L. Harrison, W.M. Smith, and et al. The transition to ventricular fibrillation induced by reperfusion after acute ischemia in the dog: A period of organized epicardial activation. *Circulation*, 63:1371–1379, 1981.
- [9] S.J. Evans, S.S. Khan, A. Garfinkel, R.M. Kass, and et al. Is ventricular fibrillation random or chaotic? [abstract]. *Circulation*, 80(suppl 2):538, 1989.
- [10] D.R. Hooker, W.B. Kouwenhoven, and O.R. Langworthy. The effect of alternating currents on the heart. *American Journal of Physiology*, 103:444–454, 1933.

- [11] C.J. Wiggers. The physiologic basis for cardiac resuscitation from ventricular fibrillation—method for serial defibrillation. *American Heart Journal*, 20:413, 1940.
- [12] M.M. Mower, M. Mirowski, J.F. Spear, and E.N. Moore. Patterns of ventricular activity during catheter defibrillation. *Circulation*, 49:858–861, 1974.
- [13] D.P. Zipes, J. Fisher, R.M. King, A. Nicoll, and W.W. Jolly. Termination of ventricular fibrillation in dogs by depolarizing a critical mass of myocardium. *American Journal of Cardiology*, 36:37–44, 1975.
- [14] X. Zhou, J.P. Daubert, P.D. Wolf, W.M. Smith, and R.E. Ideker. Epicardial mapping of ventricular defibrillation with monophasic and biphasic shocks in dogs. *Circulation Research*, 72:145–160, 1993.
- [15] J.M. Wharton, P.D. Wolf, P.S. Chen, and et. al. Is an absolute minimum potential gradient required for ventricular defibrillation? [abstract]. *Circulation*, 74(II):342, 1986.
- [16] K.M. Kavanagh, E.V. Simpson, P.D. Wolf, G.A. Johnson, W.M. Smith, and R.E. Ideker. Minimum gradient required for biphasic defibrillation. [abstract]. *PACE*, 16:916, 1993.
- [17] Nestor G. Sepulveda, Jr. John P. Wikswa, and Debra S. Echt. Finite element analysis of cardiac defibrillation current distributions. *IEEE Tran Biom Eng*, 37(4):354–365, April 1990.
- [18] L. Glass, P. Hunter, and A. McCulloch, editors. A.T. Winfree. In *Theory of Heart*. Springer-Verlag, New York, 1991.
- [19] S. Yabe, W.M. Smith, J.P. Daubert, P.D. Wolf, and R.E. Ideker. The strength of monophasic and biphasic shocks that cause conduction block. *J American College of Cardiology*, 13:67A, 1989.
- [20] J.L. Jones, E. Lepeschkin, R. Jones, and S. Rush. Responce of cultured myocardial cells to countershock-type electric field stimulation. *American Journal of Physiology*, 235:H214–H222, 1978.
- [21] C.F. Babbs, W.A. Tacker, J.F. VanVleet, J.D. Bourland, and L.A. Geddes. Therapeutic indices for transchest defibrillator shocks: Effective, damaging, and lethal electrical doses. *American Heart Journal*, 99(6):735–38, 1980.
- [22] O.H. Tovar, K.B. Milne, and J.L. Jones. Interaction of tilt and stimulus intensity on prolongation of refractory period with monophasic and biphasic defibrillating waveforms. In *Proceedings, 15th IEEE Eng in Med and Biol Conf*, volume 13, pages 846–847, 1993.
- [23] S.M. Blanchard and R.E. Ideker. Mechanisms of electrical defibrillation: impact of new experimental defibrillator waveforms. *American Heart Journal*, 127:970–977, April, 1994.

- [24] R.J. Sweeney, R.M. Gill, and P.R. Reid. Refractory period extension for monophasic versus biphasic shocks. *JACC Abstracts*, page 422A, February, 1994.
- [25] L.N. Horowitz, J.F. Spear, and E.N. Moore. Relation of the endocardial and epicardial ventricular fibrillation thresholds of the right and left ventricles. *American Journal of Cardiology*, 48:698-701, 1981.
- [26] M.J. Burgess, D. Williams, and P. Ershler. Influence of test site on ventricular fibrillation. *American Heart Journal*, 94:55-61, 1977.
- [27] R.E. Hillsley, J.M. Wharton, A.W. Cates, P.D. Wolf, and R.E. Ideker. Why do some patients have high defibrillation thresholds at defibrillator implantation—answers from basic research. *PACE*, 17:222-239, 1994.
- [28] S.A. Strickberger, J.D. Hummel, L.E. Horwood, J. Jentzer, E. Daoud, M. Niebauer, O. Bakr, K.C. Man, B.D. Williamson, and F. Morady. The effect of polarity on defibrillation threshold using a non-thoracotomy lead system. *JACC Abstracts*, page 12A, February, 1994.
- [29] J.L. Prevost and F. Batelli. Sur quel ques effets des decharges electriques sur le coer mammifries. *Comptes Rendus des Seances de L'Academie des Sciences*, 129:1267, 1899.
- [30] O.R. Langworthy and W.B. Kouwenhoven. An experimental study of the abnormalities produced in the organism. *J Indust Hygiene*, 12:31, 1930.
- [31] W.B. Kouwenhoven. A through type current transformer and amplifier for measuring alternating current of a few milliamperes. *Rev Sci Instrum*, 2:541, 1931.
- [32] W.B. Kouwenhoven, D.R. Hooker, and O.R. Langworthy. The current flowing through the heart under conditions of electric shock. *American Journal of Physiology*, 100:344, 1932.
- [33] N.L. Gurvich and G.S. Yuniev. Restoration of regular rythm in the mammalian fibrillating heart. *American Review of Soviet Medicine*, 3:236, 1946.
- [34] C.S. Beck, W.H. Pritchard, and H.S. Feil. Ventricular fibrillation of long duration abolished by electric shock. *JAMA*, 135(15):985, 1947.
- [35] P.M. Zoll, A.J. Linenthal, W. Gibson, M.H. Paul, and L.R. Norman. Termination of ventricular fibrillation in man by externally applied electric countershock. *N Engl J Med*, 254:727, 1956.
- [36] B. Lown, J. Neuman, R. Amarasingham, and B.V. Berkovits. Comparison of alternating current with direct current electroshock across the closed chest. *American Journal of Cardiology*, 10:233, 1962.

- [37] W.R. Milnor, G.G. Knickerbocker, and W.B. Kouwenhoven. Cardiac response to transthoracic capacitor discharges in the dog's heart. *Circulation Research*, 6:60, 1958.
- [38] P.Y. Bouvrain, R. Saumont, and Y. Berthier. Etude clinique de la fibrillation ventriculaire, resultat des chocs electriques transthoraciques. *Ext Arch Mal Coeur*, 2:213, 1967.
- [39] J.C. Schuder, H. Stoeckle, P.M. Keskar, J.H. Gold, M.T. Chier, and *et al.* Transthoracic ventricular defibrillation in the dog with unidirectional rectangular double pulses. *Cardiovasc Res*, 4:497, 1970.
- [40] L.A. Geddes and W.A. Tacker. Engineering and physiological considerations of direct capacitor-discharge defibrillation. *Med Biol Eng*, 9:185, 1971.
- [41] P. Troup. Early development of defibrillation devices. *IEEE Eng in Med and Biol*, 9(2):19-24, 1990.
- [42] R.D. Mitrani, L.S. Klien, D.P. Rardon, D.P. Zipes, and W.M. Miles. *Cardiac Electrophysiology*, pages 1393-1402. W.B. Saunders Company, Philadelphia, 2 edition, 1995.
- [43] M. Mirowski, M.M. Mower, W.S. Staewen, and *et al.* Standby automatic defibrillator. an approach to prevention of sudden coronary death. *Arch Int Med*, 126:158-161, 1970.
- [44] J.C. Schuder, H. Stoeckle, J.H. Gold, J.A. West, and P.Y. Keskar. Experimental ventricular defibrillation with an automatic and completely implanted system. *Trans Am. Soc. Artifc Organs*, 16:207-212, 1970.
- [45] B. Lown and P. Axelrod. Implanted standby defibrillators. *Circulation*, 46:637-639, 1972. Editorial.
- [46] M. Mirowski, M.M. Mower, A. Langer, M.S. Heilman, and J. Schreiber. A chronically implanted system for automatic defibrillation in active conscious dogs. *Circulation*, 58(1):90-94, 1978.
- [47] M. Mirowski, P.R. Reid, M. Mower, and *et al.* Termination of malignant ventricular arrhythmias with an implanted automatic defibrillator in human beings. *N Engl J Med*, 303:322-324, 1980.
- [48] R. Yee, G.J. Klein, J.W. Leitch, and *et al.* A permanent transvenous lead system for an implantable pacemaker cardioverter-defibrillator: Non-thoracotomy approach to implantation. *Circulation*, 85:196-204, 1992.
- [49] G.H. Bardy, B. Hofer, G. Johnson, and *et al.* Implantable transvenous cardioverter-defibrillators. *Circulation*, 87:1152-1168, 1993.
- [50] J.C. Schuder, G.A. Rahmoeller, and H. Stoeckle. Transthoracic ventricular defibrillation with triangular and trapezoidal waveforms. *Circulation Research*, 14:689, 1966.

- [51] J.H. Gold, J.C. Schuder, H. Stoeckle, and T.A. Granberg. Thransthoracic ventricular fibrillation in the 100kg calf with unidirectional rectangular pulses. *Circulation*, 56(5):745, 1977.
- [52] S.E. Leeds, E.S. Macay, and K. Mooslin. Ventricular fibrillation of long duration abolished by electric shock. *American Journal of Physiology*, 165:179, 1950.
- [53] V. Alferness and R.E. Ideker. The influence of shock waveforms on defibrillation efficacy. *IEEE Eng in Med and Biol*, 9(2):25–27, 1990.
- [54] R.S. Mackay and S.E. Leeds. Physiological effects of condenser discharges. *J Applied Physiology*, 6:67, 1953.
- [55] K.W. Edmark. Simultaneous voltage and current waveforms generated during internal and external direct current defibrillation. *Surg Forum*, page 262, 1963.
- [56] R.E. Kerber. *Cardiac Electrophysiology*, pages 1360–1365. W.B. Saunders Company, Philadelphia, 2 edition, 1995.
- [57] M. Hinds, G.M. Ayers, J.D. Bourland, and *et al.* Comparison of the efficacy of defibrillation with the damped sine and constant-tilt current waveforms in the intact animal. *Med Instrum*, 21:92, 1987.
- [58] S. Saksena, R. Mehra, and *et al.* Prospective comparison of biphasic and monophasic shocks for implantable cardioverter-defibrillators using endocardial leads. *American Journal of Cardiology*, 70:304–310, 1992.
- [59] D.G. Wyse, K.M. Kavanag, A.M. Gillis, and *et al.* Comparison of biphasic and monophasic shocks for defibrillation using a nonthoracotomy system. *American Journal of Cardiology*, 71:197–202, 1993.
- [60] R.A. Winkle, R.H. Mead, M.A. Ruder, and *et al.* Improved low energy defibrillation efficacy in man with the use of a biphasic truncated exponential waveform. *American Heart Journal*, 117:122–127, 1989.
- [61] P.D. Chapman, J.W. Vetter, J.J. Souza, and *et al.* Comparative efficacy of monophasic and biphasic truncated exponential shocks for nonthoracotomy internal defibrillation in dogs. *J American College of Cardiology*, 12:739–745, 1988.
- [62] G.H. Bardy, T.D. Ivey, M.D. Allen, and *et al.* A prospective randomized evaluation of biphasic versus monophasic waveform pulses on defibrillation efficacy in humans. *J American College of Cardiology*, 14:728–733, 1989.
- [63] G.H. Bardy, C. Trouman, G. Johnson, and *et al.* Electrode system influence on biphasic waveform defibrillation efficacy in humans. *Circulation*, 84:665–671, 1991.

- [64] G.H. Bardy, R.B. Stewart, T.D. Ivey, and *et al.* Intraoperative comparison of sequential-pulse and single-pulse defibrillation in candidates for automatic implantable defibrillators. *American Journal of Cardiology*, 60:618–624, 60.
- [65] D.L. Jones, G.J. Klein, G.M. Guiraudon, and *et al.* Sequential pulse defibrillation in humans: Orthogonal sequential pulse defibrillation with epicardial electrodes. *J American College of Cardiology*, 11:590–596, 1988.
- [66] H.C. Burger and J.B. Milaan. Heart-vector and leads. part II. *Br Heart J*, 9:154–60, 1947.
- [67] C.V. Nelson, M. Chatterjee, E.T. Angelos, and H.H. Hecht. Model studies on the effect of the intracardiac blood on the electrocardiogram. *American Heart Journal*, 62:83–92, 1961.
- [68] S. Rush. An inhomogeneous anisotropic model of the human torso for electrocardiographic studies. *Medical and Biological Engineering*, 9:201–211, 1971.
- [69] S. Rush and C.V. Nelson. *The theoretical basis of electrocardiology*, pages 257–93. Clarendon Press, Oxford, 1976.
- [70] Y. Rudy and R. Plonsey. The eccentric spheres model as the basis for a study of the role of geometry and inhomogeneities in electrocardiography. *IEEE Trans Biomed Eng*, 26:392–399, 1979.
- [71] R. Plonsey. *Bioelectric Phenomena*. McGraw Hill, New York, 1969.
- [72] H.L. Gelernter and J.C. Swihart. A mathematical-physical model of the genesis of the electrocardiogram. *Biophys J*, 4:285–301, 1964.
- [73] H.L. Gelernter, J.C. Swihart, and M.A.K. Angell. The use of a mathematical model in the study of the properties on the full-surface electrocardiogram. I. scher generators in a human torso. ii. “enlarged heart” potentials. *Ann N.Y. Acad Sci*, 128:1069–84, 1966.
- [74] A.C.L. Barnard, I.M. Duck, M.S. Lynn, and W.P. Timlake. The application of electromagnetic theory to electrocardiology. II. numerical solution of the integral equations. *Biophys J*, 7:463–91, 1967.
- [75] R.H. Selvester, J.C. Solomon, and T.L. Gillespie. Digital computer model of a total body electrocardiographic surface map. an adult male-torso simulation with lungs. *Circulation*, 38:684–90, 1968.
- [76] B.N. Cuffin and D.B. Geselowitz. Studies of the electrocardiogram using realistic cardiac and torso models. *IEEE Trans Biomed Eng*, 24:242–52, 1977.

- [77] B.M. Horacek. *The effect on electrocardiographic lead vectors of conductivity inhomogeneities in the human torso*. PhD thesis, Dalhousie University, Halifax, Nova Scotia, 1971.
- [78] R.M. Gulrajani and G.E. Mailloux. A simulation study of the effects of torso inhomogeneities on electrocardiography potential using realistic heart and torso models. *Circulation Research*, 52:45–56, 1983.
- [79] S. Rush, A.J. Abildskov, and R. McFee. Resistivity of body tissues at low frequencies. *Circulation Research*, 12:40–49, 1963.
- [80] P.C. Stanley, T.C. Pilkington, and M.N. Morrow. The effects of thoracic inhomogeneities on the relationship between epicardial and torso potentials. *IEEE Trans Biomed Eng*, 33:273–284, 1986.
- [81] P.C. Stanley, T.C. Pilkington, and R.E. Ideker. Accuracy of torso extension method for anisotropic analysis. In *Proceedings 8th IEEE Eng Med Biol Conf*, volume 8, pages 299–301, 1986.
- [82] S.J. Walker and D. Kilpatrick. An automated system for modelling the electrical properties of the human torso. In *Proc Computers in Cardiology*, pages 409–412, 1985.
- [83] S.J. Walker and D. Kilpatrick. Forward and inverse electrocardiographic calculations using resistor network models of the human torso. *Circulation Research*, 61:504–513, 1987.
- [84] D. Kilpatrick, A.J. Bell, and S. J. Walker. Derived epicardial potentials differentiate ischemic ST depression from ST depression secondary to ST elevation in acute inferior myocardial infarction in humans. *J. American College of Cardiology*, 14(3):695–702, 1989.
- [85] P.C. Stanley and T.C. Pilkington. The combination method: a numerical technique for electrocardiographic calculations. *IEEE Trans Biom Eng*, 36(4):456–61, 1989.
- [86] P.C. Stanley, T.C. Pilkington, and M.N. Morrow. An assessment of variable thickness and fibre orientation of the skeletal muscle layer on electrocardiographic calculations. *IEEE Trans Biom Eng*, 38(11):1068–76, 1991.
- [87] P.R. Johnston and D. Kilpatrick. *Computational Biomedicine*, pages 191–198. Computational Mechanics Publications, Southampton, 1992.
- [88] D. Kilpatrick and P.R. Johnston. Origin of the electrocardiogram. *IEEE Eng in Med and Biol*, 4(4):479–86, 1994.
- [89] A.F. Pullan, C.P. Bradley, and P.J. Hunter. The development of a high order coupled finite element/boundary element torso model. In *Proc IEEE Eng in Med and Biol*, volume 13, 1993.

- [90] F.J. Claydon, T.C. Pilkington, A. S. L. Tang, M. N Morrow, and R.E. Ideker. A volume conductor model of the thorax for the study of defibrillation fields. *IEEE Trans Biom Eng*, 35(11):981–992, 1988.
- [91] W.J. Karlon, S.R. Eisenberg, and J. L. Lehr. Effects of paddle placement and size on defibrillation current distribution: A three-dimensional finite element model. *IEEE Trans Biomed Eng*, 40:246–255, 1993.
- [92] M.A. Camacho, S.R. Eisenberg, N.G. Perlmutter, and J.L. Lehr. Paddle position and size effects in human transthoracic defibrillation: a three-dimensional finite element model. In *Proceedings 15th IEEE Eng in Med and Biol Conf*, pages 824–825, 1993.
- [93] M.A. Camacho, S.R. Eisenberg, T.F. Kinst, N.G. Perlmutter, and J.L. Lehr. The effects of epicardial patch electrodes on transthoracic defibrillation: a three-dimensional finite element study. In *Proceedings 15th IEEE Eng in Med and Biol Conf*, pages 834–835, 1993.
- [94] R.S. Ledley and *et al.* *Cross-sectional anatomy: an atlas for CT*. Williams and Wilkins, 1977.
- [95] A.L. deJongh, F.J. Claydon, and D.M. Mirvis. Examining the fraction of intrathoracic current that enters the heart during transthoracic defibrillation of the human torso. In *Proceedings 15th IEEE Eng in Med and Biol Conf*, pages 828–829, 1993.
- [96] R. Patterson and L. Wang. Thoracic current pathways for different size and position external defibrillation electrodes based on a 3D model. In *Proc IEEE Eng in Med and Biol*, volume 13, 1993.
- [97] A. Cansell, P.H. Lechat, G. Fontaine, Y. Grosogeat, and K. Meyer-Waarden. Transvenous and subcutaneous electrode system for an implantable defibrillator, improved on large pigs. *PACE*, 11:2008–2014, 1988.
- [98] E.B. Seneta and L. Holley. Customising implantable defibrillator electrodes: an efficient finite element model for desktop personal computers. In *Proc Computers in Cardiology*, 1993.
- [99] S. Gao, A. Nadeem, O.C. Deale, P.T. Cahill, B.B. Lerman, and K.T. Ng. Uniform grid solution of 3D bio-electrostatic problems on a massively parallel computer. In *Proceedings 15th IEEE Eng in Med and Biol Conf*, pages 764–765, 1993.
- [100] D.B. Jorgenson, D.R. Haynor, G.H. Bardy, and Y. Kim. Computational studies of transthoracic and transvenous defibrillation in a detailed 3-D human thorax model. *IEEE Trans Biom Eng*, 42(2):172–84, 1995.
- [101] E.B. Seneta and L. Holley. Optimizing defibrillation electrodes: automating the search for better configurations. In *Proc Computers in Cardiology*, 1994.

- [102] L. Ingber and B. Rosen. Genetic algorithms and very fast simulated reannealing: a comparison. *Mathematical and computer modelling*, 16:11, 1992.
- [103] S.A. Hutchinson and K.T. Ng. An optimization algorithm for electrode configurations in transcardiac defibrillation. In *Proceedings 15th IEEE Eng in Med and Biol Conf*, pages 836–837, 1993.
- [104] J.E. Dennis and R.B. Schnabel. *Numerical methods for unconstrained optimization and nonlinear equations*. Prentice-Hall, Englewood Cliffs, NJ, 1983.
- [105] X. Min, L. Wang, M Hill, J. Lee, and R. Mehra. A detailed human thorax FEM model for the cardiac defibrillation study. In *Proceedings 15th IEEE Eng in Med and Biol Conf*, pages 838–839, 1993.
- [106] R.S. MacLeod, C.R. Johnson, and P.R. Ershler. Construction of an inhomogeneous model of the human torso for use in computational electrocardiology. In *Proceedings 13th IEEE Eng Med Biol Soc*, volume 13, pages 688–9, 1991.
- [107] J. Schmidt, J. Eason, and T. Pilkington. Adaptive grid generation. In *Proceedings 14th IEEE Eng Med Biol Soc*, volume 14, pages 593–4, 1992.
- [108] O.S. Odesanya, W.N. Waggenspack, and D.E. Thompson. Construction of biological surface models from cross-sections. *IEEE Trans Biom Eng*, 40(4):329–34, 1993.
- [109] A. Nadeem, K.T. Ng, and J.B. Jordan. Image processing and grid generation for finite element analysis of defibrillation. In *Proceedings 15th IEEE Eng in Med and Biol Conf*, pages 832–833, 1993.
- [110] P. Macfarlane and T.D.V. Lawrie, editors. R. Plonsey. In *Comprehensive Cardiology*, volume 1. Pergamon Press, New York, 1989.
- [111] H.P. Schwan and C.F. Kay. The conductivity of living tissues. *Ann N.Y. Acad Sci*, 65:1007–1013, 1957.
- [112] W. Peters, S. Solingen, Y. Kobayshi, R. Scharf, W.J. Mandel, and E.S. Gang. Transmyocardial impedance during single and multiple internal ventricular defibrillation shocks. *Americal Journal of Physiology*, 267:H684–H693, 1994.
- [113] L.A. Geddes and L.E. Baker. The specific resistance of biological material—a compendium of data for the biomedical engineer and physiologist. *Med Biol Eng*, 5:271–293, 1967.
- [114] D.C. Barber and B. H. Brown. Applied potential tomography. *J Phys E: Sci Instrum*, 17:723–732, 1984.

- [115] W.K. Pluta. *The method of spatial localisation of tissue electrical conductivity changes for use for intensive care*. PhD thesis, Technical University of Warsaw, 1987.
- [116] C.D. Swerdlow, R.M. Kass, C. Hwang, E. Gang, P.S. Chen, and T. Peter. Effects of voltage and respiration on impedance in nonthoracotomy defibrillation pathways. *American Journal of Cardiology*, 73(9):688–692, 1994.
- [117] J.M. Wharton, P.D. Wolf, W.M. Smith, P.S. Chen, D.W. Frazier, S. Yabe, N. Danieleley, and R.E. Ideker. Cardiac potential and potential gradient fields generated by single, combined and sequential shocks during ventricular defibrillation. *Circulation*, 85:1510–1523, 1992.
- [118] S. Brigitte and S. Gisela. Materials for intracardial ICD-electrodes. In *Proceedings 15th IEEE Eng in Med and Biol Conf*, pages 879–880, 1993.
- [119] P.H Schimpf, D.B. Jorgenson, G. Johnson, D.R. Haynor, G.H. Bardy, and Y. Kim. In vitro characterization of transvenous defibrillation electrodes. *American Heart Journal*, 128(3):635, 1994.
- [120] D. Panescu, J.G. Webster, and R.A. Stratbucker. A nonlinear finite element model of the Electrode-Electrolyte-Skin system. *IEEE Trans Biom Eng*, 41(7):681–7, 1994.
- [121] R.C. Barr and M.S. Spach. Inverse calculation of QRS-T epicardial potentials from body surface potential distributions for normal and ectopic beats in the intact dog. *Circulation Research*, 42(5):661–75, 1978.
- [122] B.J. Messenger-Raport and Y. Rudy. Noninvasive recovery of epicardial potentials in a realistic heart-torso geometry. *Circulation Research*, 66(4):1023–39, 1990.
- [123] D.L. Derfus, T.C. Pilkington, E.W. Simpson, and R.E. Ideker. A comparison of measured and calculated intracavity potentials for electrical stimuli in the exposed dog heart. *IEEE Tran Biom Eng*, 39(11):1192–1206, 1992.
- [124] A.V. Shahidi, P. Savard, and R. Nadeau. Forward and inverse problems of electrocardiology: Modeling and recovery of epicardial potentials in humans. *IEEE Trans Biomed Eng*, 41(3):249–56, 1994.
- [125] D. Kilpatrick and S.J. Walker. A validation of derived epicardial potential distributions by prediction of the coronary artery involved in acute myocardial infarction in humans. *Circulation*, 76(6):1282–9, 1987.
- [126] A.S. Manolis. Transvenous endocardial cardioverter defibrillator systems—is the future here. *Archives of Internal Medicine*, 154:617–622, March, 1994.

- [127] G.C. Timmis. The development of implantable cardioversion defibrillation systems—the clinical chronicle of defibrillation leads. *American Heart Journal*, 127:1003–1009, April, 1994.
- [128] S. Saksena, R.B. Krol, and R.R. Kaushik. Innovations in pulse generators and lead systems—balancing complexity with clinical benefit and long term results. *American Heart Journal*, 127:1010–1021, April, 1994.
- [129] J.F. Swartz, P. Karasik, and R.D. Fletcher. Sub-scapular patch position enhances multiple pathway non-thoracotomy defibrillation in humans. *Circulation*, 4:I-441, 1992. Abstract.
- [130] M.R. Gold, D.W. Riggio, Z. Feliciano, S.R. Shorofsky, and A.H. Foster. Comparison of monophasic and biphasic waveforms for defibrillation in a nonthoracotomy lead system. *Circulation*, 88, No 4, Part2:I-215, 1993.
- [131] D. Schwartzman, R.L. Jadonath, M.W. Preminger, R. Kay, C.D. Gottlieb, and F.E. Marchlinski. The importance of subcutaneous patch position on the defibrillation threshold for non-thoracotomy defibrillation lead systems. *Circulation*, 88, No 4, Part2:I-216, 1993.
- [132] G.H. Bardy, P.J. Kudenchuk, G.L. Dolack, J.E. Poole, G. Johnson, R. Mehra, and M. H. Raitt. A prospective randomized comparison in humans of the unipolar pectoral defibrillation system with one incorporating an additional electrode in the coronary sinus. *Circulation*, 88, No 4, Part2:I-216, 1993.
- [133] G.H. Bardy, G.L. Dolack, J.E. Poole, P.J. Kudenchuk, G. Johnson, M. H. Raitt, R. Mehra, P. DeGroot, and B.O. Hofer. A prospective randomized comparison in humans of 50% vs 65% tilt biphasic pulse defibrillation using the unipolar pectoral transvenous defibrillation system. *Circulation*, 88, No 4, Part2:I-113, 1993.
- [134] S. Saksena, M. Lehmann, L.B. Mitchell, and V. Sakun. Device use and clinical results with a third-generation cardioverter-defibrillator using endocardial or epicardial leads. *Circulation*, 4:I-60, 1992. Abstract.
- [135] M. Block, D. Hammel, D. Bocker, F. Isbruch, D. Wietholt, and M. Borggrefe. Biphasic shock waveform and a single bipolar transvenous lead should be the nonthoracotomy defibrillation of first choice. *Circulation*, 4:I-442, 1992. Abstract.
- [136] G.H. Bardy, B. Hofer, G. Johnson, P.J. Kudenchuk, J.E. Poole, G.L. Dolack, M. Gleva, R. Mitchell, and D. Kelso. Experience with transvenous defibrillators in 68 consecutive patients. *Circulation*, 4:I-60, 1992. Abstract.
- [137] F.J. Venditti, G. Vassolas, and D. Martin. Chronic defibrillation thresholds in an implantable transvenous cardioverter defibrillator system. *Circulation*, 4:I-441, 1992. Abstract.

- [138] J.W. Leitch, R. Yee, and Multicenter PCD Investigators Group. Predictors of epicardial defibrillation efficacy. *Circulation*, 4:I-443, 1992. Abstract.
- [139] S. Saksena, R.B. Krol, T. John, D. Mehta, R. Raju, P. Degroot, and R. Mehra. Optimal thoracic electrode or device location for cardioverter-defibrillators with endocardial defibrillation leads. *Circulation*, 4:I-443, 1992. Abstract.
- [140] H.H. Hsia, R.B. Kleiman, B.T. Flores, and F.E. Marchlinski. Comparison of simultaneous versus sequential pathways for defibrillation energy delivery. *Circulation*, 4:I-790, 1992. Abstract.
- [141] G.H. Bardy, G. Johnson, J.E. Poole, G.L. Dolack, P.J. Kudenchuk, D. Kelso, R. Mitchell, and B. Hofar. A simplified, single lead unipolar transvenous cardioverter-defibrillator. *Circulation*, 4:I-792, 1992. Abstract.
- [142] M. Zardini, R. Yee, R. Mehra, G. Klein, R.K. Thakur, C.A. Morillo, and H.W. Stites. Improved defibrillation efficacy with a simple non-thoracotomy lead configuration. *JACC Abstracts*, page 66A, February, 1993.
- [143] G.A. Buser, M.J. Krasna, A.H. Foster, and M.R. Gold. A comparison of lead configurations for thoracoscopic defibrillator systems. *Circulation*, 4:I-441, 1992. Abstract.
- [144] C. A. Brebbia and J. Dominguez. *Boundary Elements An Introductory Course*. Computational Mechanics Publications, Southampton, second edition, 1992.
- [145] C. Johnson. *Numerical solution of partial differential equations by the finite element method*. Cambridge University Press, Cambridge, 1987.
- [146] P.M. Nielsen, I.J. Grice, B.H. Smaill, and P.J. Hunter. Mathematical model of geometry and fibrous structure of the heart. *Am J Physiol*, 260, No 4, Part2:H1365-78, 1991.